目　次

Jiufengershan landslide induced by 1999 Chi-chi earthquake. The Next Generation of Research on Earthquake-induced Landslides: An International Conference in Commemoration of 10th Anniversary of the Chi-Chi Earthquake, pp402-406, 2009.

主論文

Importance of Carbonaceous Materials in Fault Zones on Their Mechanical Properties: Field and Experimental Studies

A dissertation

by

Kiyokazu OOHASHI

Department of Earth and Planetary Systems Science,

Graduate School of Science, Hiroshima University

Doctor of philosophy

January 2011

ABSTRACT

Carbonaceous materials are contained in fault zones in a variety of geological settings, but they received little attention even though they may affect mechanical properties of faults significantly. The aim of this thesis is to reveal natural occurrence of carbonaceous materials in faults through fieldwork and to evaluate their effects on fault mechanics by laboratory experiments. In particular, graphite, a form of carbonaceous materials, should receive attention because it is a well-known solid lubricant and has potential to act as a lubricating agent for fault zones. The main outcomes are as follows:

Abundant graphite was in fault zones of the Atotsugawa fault system through the present work. The mesoscopic and microscopic observations of the fault rocks revealed two different processes of graphite enrichment into the fault zones. One is pressure solution process; it enhances the mass transfer of water-soluble minerals such as quartz and carbonates from rocks, resulting in the enrichment of insoluble minerals such as carbon and metals in fault zones. The other process is the precipitation of graphite from high-temperature carbon-rich fluid; this type of graphite typically appears as injection veins within cataclasitic fault zones. The two processes have lead to ~15 wt% of graphite concentration in the Atotsugawa fault zones, while their hostrocks contain only 0~3 wt% of carbonaceous materials.

In order to determine mechanical properties of carbonaceous faults, frictional experiments were conducted on pure amorphous carbon and graphite gouges at a wide range of slip rates from 50 μm/s to 1.3 m/s and normal stresses of 0.5–50 MPa in atmospheres of air and nitrogen gas, using two rotary-shear friction apparatuses and a biaxial friction apparatus. The friction of graphite gouge was strikingly low (steady-state friction coefficient, μ_{ss} = ~0.1) over five orders of magnitude in slip rate. On the other hand, the frictional coefficient of amorphous carbon gouge was relatively high (μ_{ss} = ~0.54) at low slip rates. When, however, the slip rate is higher than 10 mm/s, the friction dropped toward ~0.1 which is the same level as that of graphite gouge at a slip rate of 1.3 m/s. The result suggests that the faults with amorphous carbon are not weak at low slip rates, but they can become dynamically weak to foster fault motion during an earthquake. XRD and TEM analyses revealed that graphitization can indeed occur during seismogenic fault motion perhaps due to large shear strain, short-lived flash heating and stress concentration at asperity contacts, even at low temperatures and

pressures under anoxic environments where the most earthquakes occur. Thus the enriched carbonaceous materials in fault zones can act as a lubricant during earthquakes.

The carbonaceous fault rocks in nature contain not only graphite but also other minerals such as quartz. In order to determine the minimum amount of graphite in reducing the frictional strength of faults dramatically, friction experiments were performed on mixed graphite and quartz gouges with different compositions, using a rotary-shear low to high-velocity friction apparatus. Experimental result clearly indicates that the friction coefficient of the mixture gouge decreases with graphite content following a power-law relation irrespective of slip rate; it starts to reduce at the graphite fraction of 5 vol% and reaches to the almost same level of pure graphite gouge at the fraction of more than 28 vol%. The slight weakening of 5-10 vol% of graphite mixture is associated with the development of partial connection of graphite matrix, forming a slip localized surface. On the other hand, the formation of through-going connection of diffused graphite-matrix zones along shear planes is most likely to have caused the dramatic weakening of gouge with graphite of more than 28 vol%. The non-linear power-law dependency of friction on graphite content leads to more efficient reduction of fault strength as compared with the previously reported linear dependency on the effects of clay minerals. Hence the result demonstrates the potential importance of graphite as a weakening agent of mature faults as graphite can reduce friction efficiently as compared with other weak clay minerals. Such mechanical properties of graphite may explain the lack of pronounced heat flow in major crustal faults and the long-term fault weakening.

The integrated field and experimental studies thus revealed (a) ubiquitous distribution of graphite along the western part of the Atotsugawa fault system, (b) the significant weakness of graphite at a wide range of slip rates and (c) enough graphite content in those fault zones for reducing friction. The results indicate the importance of graphite as a weakening agent of faults. Geophysical investigation of deep underground seismic-velocity and resistivity structures implies the existence of graphite at the deeper part of the Atotsugawa fault system. Geophysical data and the mechanical properties of graphite revealed in this study suggest that graphite in fault zones is associated with the creep-like fault motion and the distribution of microearthquakes observed along the Atotsugawa fault system.

ACKNOWLEDGEMENTS

I would like to express my sincere thanks to Prof. Toshihiko Shimamoto of China Earthquake Administration (an emeritus professor of Hiroshima University) and Dr. Takehiro Hirose of Kochi Core Center, JAMSTEC (a visiting associate professor of Hiroshima University) for introducing me the field of experimental rock deformation, many useful discussions, encouragements and critical reading of the manuscript. I wish to thank Professors H. Hidaka, Y. Takahashi, T. Sekine and K. Terada for guidance and encouragements during the doctoral course and for examination of my doctoral thesis. I would like to thank Dr. Jun-ichi Ando of Hiroshima University for critical discussion and his helpful technical assistance and advices in TEM analysis and Dr. Ken-ichi Hoshino and Dr. Ikuo Katayama for valuable discussions and encouragements. I would like to express my appreciation to Dr. Raehee Han of KIGAM for sincere and constructive discussions and help with the experiments. I would like to thank Mr. Muranaka of workshop for advanced techniques, Hiroshima University for making pressure vessel with his skillful technique. I wish to thank Dr. Hideki Mukoyoshi for help with the SEM observation and sample preparation. I wish to thank Dr. Kenta Kobayashi of Niigata University for providing the carbonaceous fault rock samples.

I am grateful to Prof. Richard H. Sibson of Otago University for many encouragements and helpful suggestions during the field excursion in the Atotsugawa fault system. Encouragement and helpful suggestion by Prof. Chris Spiers of Utrecht University are also appreciated. Constructive reviews for the JSG paper by Anne-Marie Boullier and Cristiano Collettini are greatly appreciated. I would like to thank Dr. Hiroyuki Noda and Dr. Ken-ichi Hirauchi for beneficial discussions and encouragements. I also thank to Dr. Tom Mitchell of Ruhr University, my colleague Mr. Tetsuhiro Togo and Mr. Keishi Okazaki for various discussions and help with the experiments.

This work was supported by a Grant-in-Aid for JSPS fellows (21-04493), Japan Society for Promotion of Science. Transmission electron microscope work was done at the Natural Science Center for Basic Research and Development (N-BARD), Hiroshima University.

I greatly thank my parents for their supports and encouragements.

CONTENTS

LIST OF FIGUREURES AND TABLES

1. INTRODUCTION

Carbonaceous material is one of the major components in the earth's crust. It characteristically concentrated along fault zones developed at various tectonic settings such as sedimentary basins, pelitic metamorphic belts and accretionary complexes (Oohashi and Kobayashi, 2008, Awaji, 2006, Zulauf et al., 1990, Manatschal, 1999 etc., Figure 1.1). These carbonaceous fault zones typically contain 1~20 wt% of graphite, whereas the hostrock of these faults contains only 0~3 wt% of graphite. Graphite is one of the carbonaceous materials and has the lowest friction among the minerals that naturally exists on earth (e.g., Savage, 1948). As a weak mineral in fault zone primary controls fault rheology, graphite is hence a key mineral for understanding the mechanics of faulting. However its mechanical role in faulting has still remained unclear. I thus planed integrated field and experimental studies to reveal the formation process of graphite-enriched fault zone and to evaluate its effects on fault mechanics.

The first aim of this thesis is to describe the natural occurrence of carbonaceous materials along the Atotsugawa fault system (Chapter 2). ; see for its location). This fault system consists of Atotsugawa fault to the south and of Ushikubi fault to the north that runs nearly parallel in ENE-SWS directions (Fig. 1.2). Atotsugawa fault is one of representative A-class active faults in Japan that caused the 1858 M7.0-7.1 Hietsu earthquake (The Research Group of Active Faults in Japan, 1991). Detailed geodetic, seismological and electromagnetic investigations have been performed on this fault system (e.g., Goto et al., 2005, Nakajima et al., 2010, Ohzono et al., 2011). Thus, the Atotsugawa fault system is an ideal field to link the crustal-scale fault behavior and the mechanical properties of fault rocks that are measured by laboratory friction experiments. I focused more on the Ushikubi fault than on the Atotsugawa fault because Ushikubi fault zones are frequently crop out (Oohashi and Kobayashi, 2008). I proposed two possible mechanisms for carbon-enrichment along the fault zones on the field survey and fault rock analysis on this fault system. I then discuss the development process of graphite-bearing faults.

The second aim is to experimentally reproduce the mineralogical and textural features of carbonaceous fault rocks observed in the Atotsugawa fault system, and to determine their mechanical properties through a series of laboratory friction experiments. Chapters 3 reports results from friction experiments on amorphous carbon

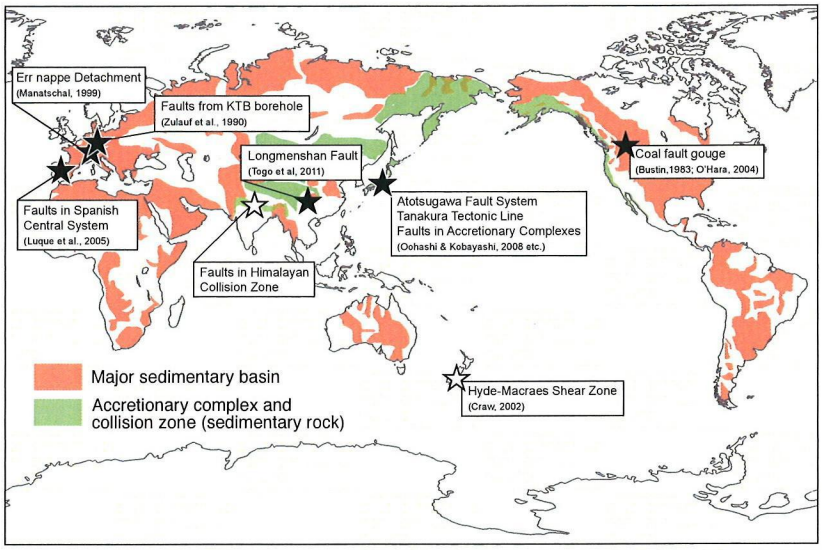

Fig. 1.1. A compilation of carbonaceous upper crustal faults (filled stars) and lower crustal shear zone (open star) reported in the world.

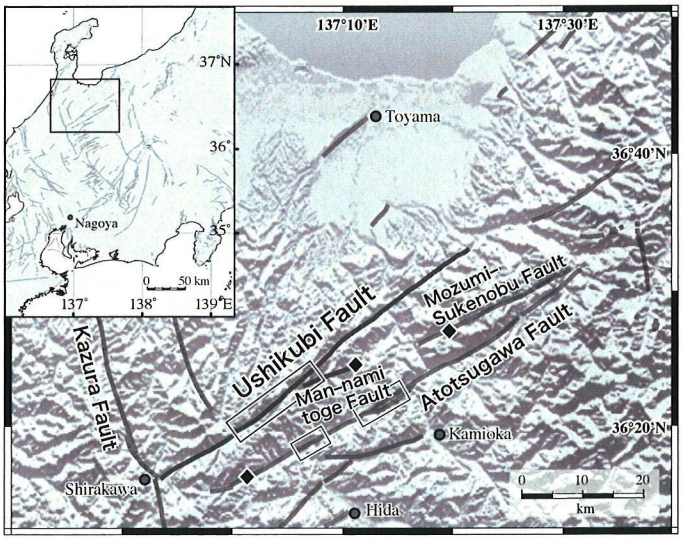

Fig. 1.2. Index map showing the location of the study areas (black boxs and diamond dots) on the topographic relief of northern central Japan. The map also shows the trace of active faults based on Research Group for Active Faults of Japan ed. (1980). The base topographic relief was created making use of 50 m-DEM of the Geographical Survey Institute of Japan.

and graphite in order to compare frictional behaviors of two representative carbonaceous materials at low to high slip rates (10^{-5} to 1 m/s) and to see if graphite can form from amorphous carbon during fault motion. Synthetic materials were used as gouges to avoid complexity from mixing other minerals. The experiment at the wide range of slip rates is essentially important since natural fault involves from slow slip rates during fault creep and nucleation phase of earthquakes to high slip rates on the order of m/s during seismic fault motion. A surprising result is that graphite forms from amorphous carbon during seismic slip rate at temperature and pressure conditions far below than those previously thought (Diessel, 1978; Buseck and Huang, 1985). This provides a new perspective in considering graphite genesis in natural fault zones. Results also reveal contrasting behaviors of graphite and amorphous carbon; the former exhibits very low friction at all slip rates, whereas the latter has shows fairly high friction at low to intermediate slip rates and dramatic weakening at high slip rates. Frictional behavior of amorphous carbon is similar to that of fault gouges (e.g., Mizoguchi et al, 2007).

Natural fault zones contain minerals other than carbonaceous materials, so that Chapter 4 reports experimental results on gouge composed of mixture of quartz and graphite with different proportions. Quartz is used as a representative granular mineral and such experiments are needed to determine how much graphite is needed to lubricate faults. In Chapters 5, the processes of such mineral transformation of carbonaceous materials and its influence on fault behavior are examined based on the friction experiments under controlled atmospheres conditions and detailed material analysis by *scanning* and transmission electron microscopes. Finally Chapter 6 discusses the physical and chemical effects of carbonaceous materials on behaviors of natural faults. In particular, I discuss the origin of fault creep characteristically observed along the Atotsugawa fault system by integrating the results of field and experimental studies.

2. Occurrence of graphitic fault rocks and its origins: A field study along the Atotsugawa fault system

2-1. Introduction

2-1-1. Occurrence of carbon bearing faults and its general features

Fault rocks enriched in carbonaceous materials (e.g. amorphous carbon and lowly to highly crystalline graphite) are reported from several fault zones (see Figure 1.1), the Ushikubi fault, central Japan (Oohashi, 2008MS; Oohashi and Kobayashi, 2008), and the Tanakura Tectonic Line, NE Japan (Awaji, 2006), the KTB borehole, Germany (Zulauf et al., 1990), the Err nappe detachment fault, Switzerland (Manatschal, 1999) and the Longmenshan fault (Togo et al., 2011; the source fault of 2008 Sichuan earthquake), China. The occurrence of carbonaceous fault zone also have been found from the Median Tectonic Line in Kii peninsula and Shikoku district, the Chichibu and the Shimanto accretionary complexes, Japan. The former faults are developed in continent metamorphic belts, and latter are in accretionary terranes, but in common, these appear characteristically as blackish ultracataclasite or fault gouge in the fault core, and graphite is contained within the fine matrix of those fault rocks. This section outlines the general features of the carbonaceous fault zones; mineral composition, crystallinity of graphite, meso- to micro-scale texture and special distribution of carbonaceous minerals.

The outcrop shown in Figure 2.1 is located in the central region of the Ushikubi fault. The fault core consists mainly of foliated cataclasite and foliated fault gouge zone that is characterized by alternation of blackish fault gouge and layer of leucocratic coarse fragments (Figure 2.1a and b). According to the X-ray diffraction (XRD) analyses of blackish fault gouge collected from the outcrop suggest that quartz, feldspar and highly crystallized graphite are principal compositions and titanium mineral (anatase) and pyrite are found as an accessory mineral (Figure 2.1 c). Based on mass measurement before and after the extraction of graphite, these blackish fault gouge contains about 3-10 wt.% of graphite with particles < 2 μm in size. The outcrop of the Tanakura Western Marginal fault (Figure 2.2; Awaji et al., 2010) also contains about 10

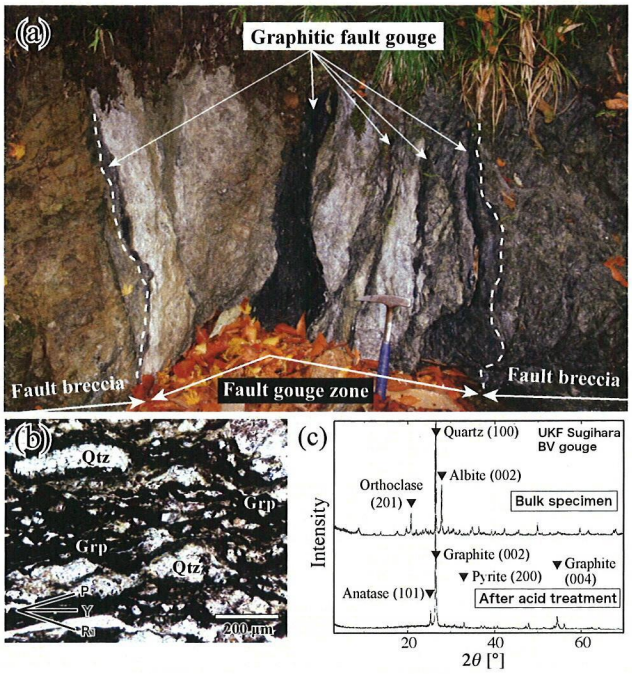

Fig. 2.1. An example of the graphite bearing fault rock along the Ushikubi fault (E1 strand). (a) Photograph of carbonaceous (graphitic) fault zone in central portion of the Ushikubi fault. Locality of this outcrop is shown in Fig.2.3. Highly deformed blackish fault gouge zones are developed within the fault core. (b) Plane-polarized light photograph of thin section of the graphitic fault gouge (XZ section). P, R1, and Y denote the P-, R1-, and Y-surfaces, respectively. (c) X-ray powder diffraction patterns of black fault gouge. Specimen of bottom pattern wes treated with hydrofluoric acid and hydrochloric acid for extraction of carbonaceous materials.

wt% of carbonaceous materials within the fault gouges.

2-1-2. Reports of carbonaceous materials from worldwide fault/shear zones

Both amorphous carbon (e.g. organic matter) and graphite are also found from worldwide fault zones except for the Atotsugawa fault and the Tanakura tectonic line. Bustin (1983) reported that the vitrinite, a kind of bituminous coal, is contained in fault zones which displaces sedimentary rocks (shale and silt stone). Zulauf et al. (1990) firstly paid attention to graphite-bearing fault rock which is came from the superdeep research well KTB, Germany. They named graphite (and phyllosilicate)-enriched fault rock a "graphitic cataclasite" and interpreted that its fabric developed by aseismic than by seismic slip. Quantitative analysis of chemical composition along the KTB borehole (Winter et al., 2002), revealed the enrichment of carbon (graphite) content from almost carbon-free hostrock (paragneiss, amphibolite and metagabbro) toward the cataclastic

shear zones (maximum 1 wt% in bulk content). Another graphite-bearing fault is reported from the Err nappe detachment, Switzerland (Manatschal, 1999). In this fault zone, 2-6 wt% of carbon (graphite) is only detected from the fault core, whereas the hanging and foot wall rock are consists of carbon-free orthogneiss and granite. Graphite-enriched fault is reported from not only the upper crustal fault zone but also ductile shear zone. Craw (2002) found ~ 4 wt% of graphite from the Hyde-Macraes shear zone in the Otago shist, New Zealand. The shear zone is consists of greenshist facies schists and graphite-bearing microshears, and graphite enrichment occurs only in association with hydrothermal mineralized shears within the schists. These reports related to carbonaceous fault/shear zones from worldwide various types of geology,

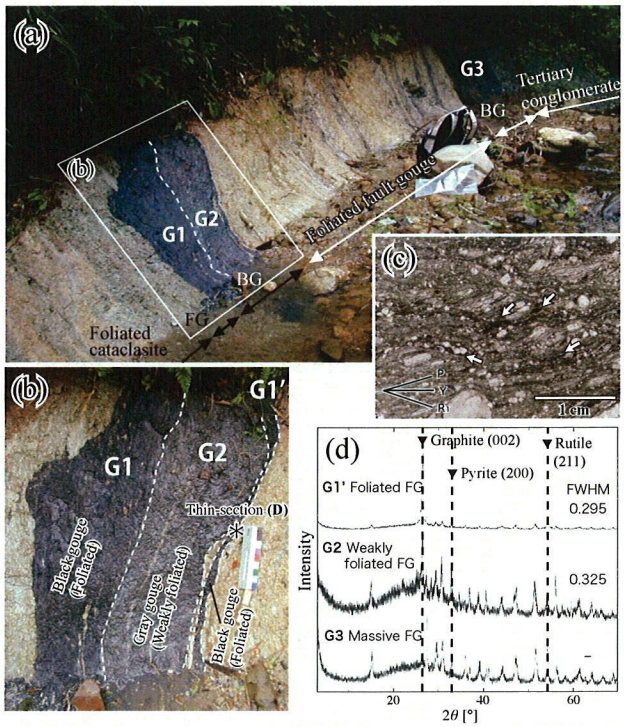

Fig. 2.2. Carbonaceous fault rock in the Tanakura Tectonic Line and its mineralogical features. (a) Photograph of the Inasawa outcrop of the Tanakura Western Marginal Fault (FG, fault gouge; BG, black fault gouge; G1, strongly foliated black fault gouge (slip localized zone); G2, weakly foliated gray fault gouge; G3, almost nonfoliated black fault gouge). (b) Closeup of the carbonaceous fault gouge. Narrow, highly deformed fault gouge G1′ (a few centimeters wide) is between G2 and the foliated gouge zone. We defined G1′ as the principal slip zone. (c) Plane-polarized light photograph of thin section of the G1′ fault gouge (XZ section). P, R1, and Y denote the P-, R1-, and Y-surfaces, respectively. (d) X-ray powder diffraction patterns of black fault gouge. Specimens were treated with hydrofluoric acid and hydrochloric acid for extraction of carbonaceous materials. The graphite corrected from G1′ gouge zone (principal slip zone) shows higher crystallinity than that of G2 and G3 gouge.

formation depth and tectonic background suggest that the possibility of universal appearance of carbonaceous materials within the fault zones.

2-1-3. What is the essential process for carbon-enrichment along the fault zones?

As mentioned in chapter 1, a few to more than a dozen % of graphite (in bulk content) is found from the blackish fault rocks along the Atotsugawa fault system and the Tanakura tectonic line. On the other hand, a protolith of these faults contains 0 (i.e. granitic rocks) ~ only 2-3 wt% of graphite. This quantitative difference on content suggests that the enrichment process(es) of graphite probably acted within the fault zones. Zulauf et al. (1999) also pointed out this graphite enrichment from the KTB borehole; +80 ~ 140 % increment (wallrock: 300-400 and 2300 ppm, shear zone: 900 and 3700 ppm) of carbon was detected from the shear zones against to the wallrock gneiss. They speculated that the graphite was derived from the following chemical reaction along the fault zones;

$$CH_4 + CO_2 \rightarrow 2\,\overset{\text{Graphite}}{C} + 2H_2O \qquad (1)$$

that is reducing reaction of carbon dioxide by methane and generation of solid carbon with water. This is an "active" enrichment process of graphite due to the fluid-related precipitation of carbon within the fault zone. In fact, graphite-bearing fluid inclusions and reasonable composition of coexisting fluid are reported from several metamorphic belts including paragneiss of KTB core samples (Pasteris and Chou, 1998). However, (1) direct evidence of graphite-precipitation, (2) its relation with faulting and (3) other possible candidates for graphite-enrichment are not well examined up to now. Additionally, concentration mechanisms of another carbonaceous fault zone are not explored individually. Therefore, purpose of this chapter is focused to identify the mechanism for carbon-enrichment along the fault zones base on the fault rock analysis of the Atotsugawa fault system.

2-2. Geological setting

The rocks in the area of the Atotsugawa fault system are all part of the Hida belt which is composed of the Paleozoic to early Mesozoic Hida metamorphic rocks,

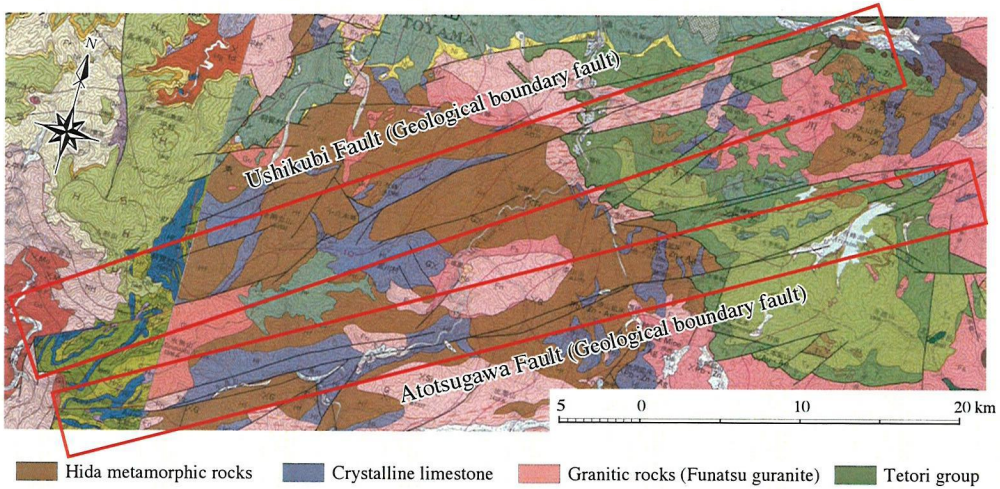

Fig. 2.3. Geological map around the Atotsugawa fault system after Geological maps of Japan 1/200,000 TAKAYAMA and KANAZAWA.

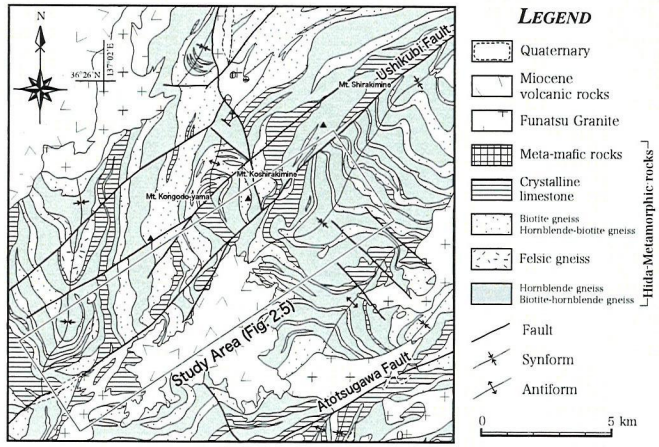

Fig. 2.4. Detained geological map around the study area (after Sohma and Akiyama, 1984).

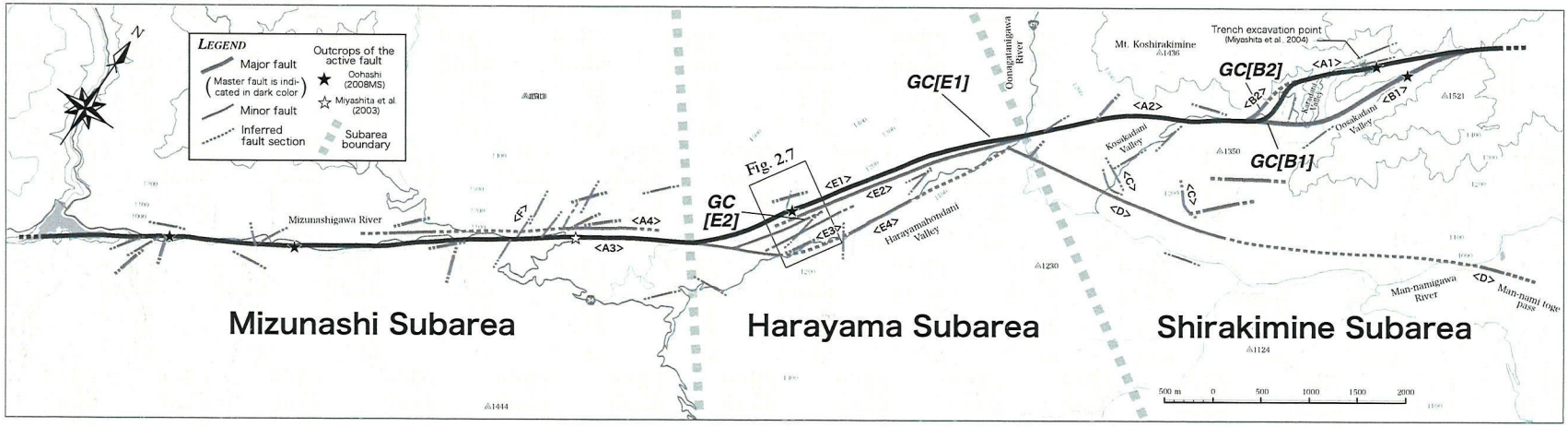

Fig. 2.5. Fracture distribution and geometry of the shear zone along the Ushikubi fault and the Man-nami toge fault in the study area. GC: location of the outcrop of graphitic cataclasite.

upper Jurassic-lower Cretaceous sedimentary rocks (the Tetori group), intrusions of Cretaceous graphitic rocks and Miocene volcanic rocks (Figure 2.3 and 2.4). The Hida metamorphic rocks are consists of paragneiss (sedimentaty origin), volcanic gneiss and older granitoids which undergo lower crustal metamorphism. Paragneiss such as biotite gneiss or amphibole gneiss often contains small amount of graphite for accessory minerals. According to Sohma and Akiyama (1983), the Hida metamorphic belt around the Atotsugawa fault system can be divided into two massifs in terms of petrological features. One is characterized by dominance of pelitic gneiss, and is distributed in western half of the Atotsugawa fault system. The other is characterized by dominance of igneous-origin amphibole gneiss, and is distributed in eastern half. The Tetori group is distributed in near surface (< 2 km in depth) of eastern half.

The Atotsugawa fault system is an active fault which is composed of four different faults; the Atotsugawa fault, the Ushikubi fault, the Mozumi-sukenobe fault and the Man-nami toge fault. From all of these faults, large fault damage zones (> 30 m in width) correspond to the master fault, and accompanying large-scale shear zone (> 1 km in width) are reported.

2-3. Methods

Graphite-bearing fault rocks along the Atotsugawa fault system mostly appear as an altered cataclasite or incohesive fault gouge which is suffered subsequent alteration at the near ground surface and deformation overprints. Therefore, it was difficult to recognize the primitive structures and elementary process related to the carbon-enrichment. In order to break through this problem, the author conducted field survey and rock sampling especially focused on away from the active, master fault to find the cohesive cataclasites which may be preserving primitive structures. About 20 days field survey with description of fault outcrop and more than 30 of fault-rock sampling were done along the central portion of the Ushikubi fault and western portion of the Atotsugawa fault (Figure 1.2).

Collected fault rocks were analyzed by an optical microscope, a laser Raman spectroscope and a scanning electron microscope (SEM) with energy dispersive spectroscopy (EDS) after making thin sections. Techniques of sample preparation and

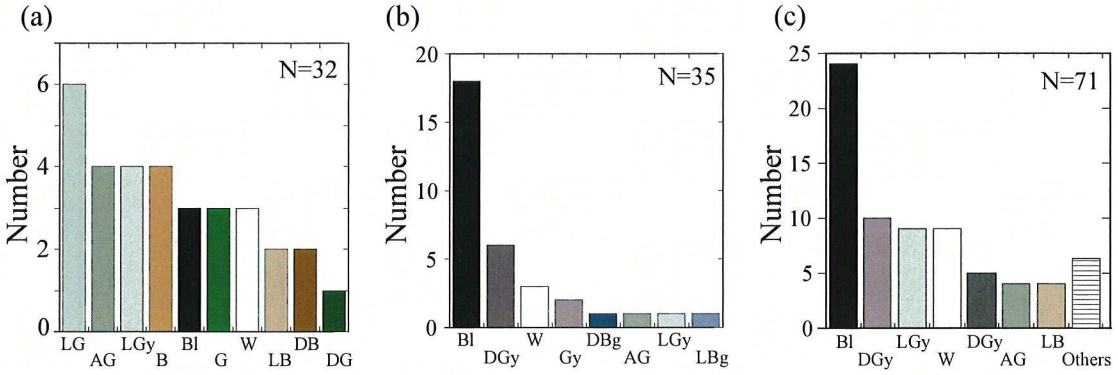

Fig. 2.6. Histograms showing occurrence probability of the blackish fault gouge for (a) Mizunashi, (b) Harayama and (c) Shirakimine subarea along the central part of the Ushikubi fault. Blackish fault gouge contains few to 10 wt. % of graphite. Graphitic fault gouge takes up almost half of the whole at central (Harayama) and northeastern (Shirakimine) subarea. LG=Light green, AG=Ash green, LGy=Light gray, B=Brown, Bl=Black, G=Green, W=White, LB=Light brown, DB=Dark brown, DG=Dark green, DGy=Dark gray, DBg=Dark bluish gray, LBg=Light bluish gray.

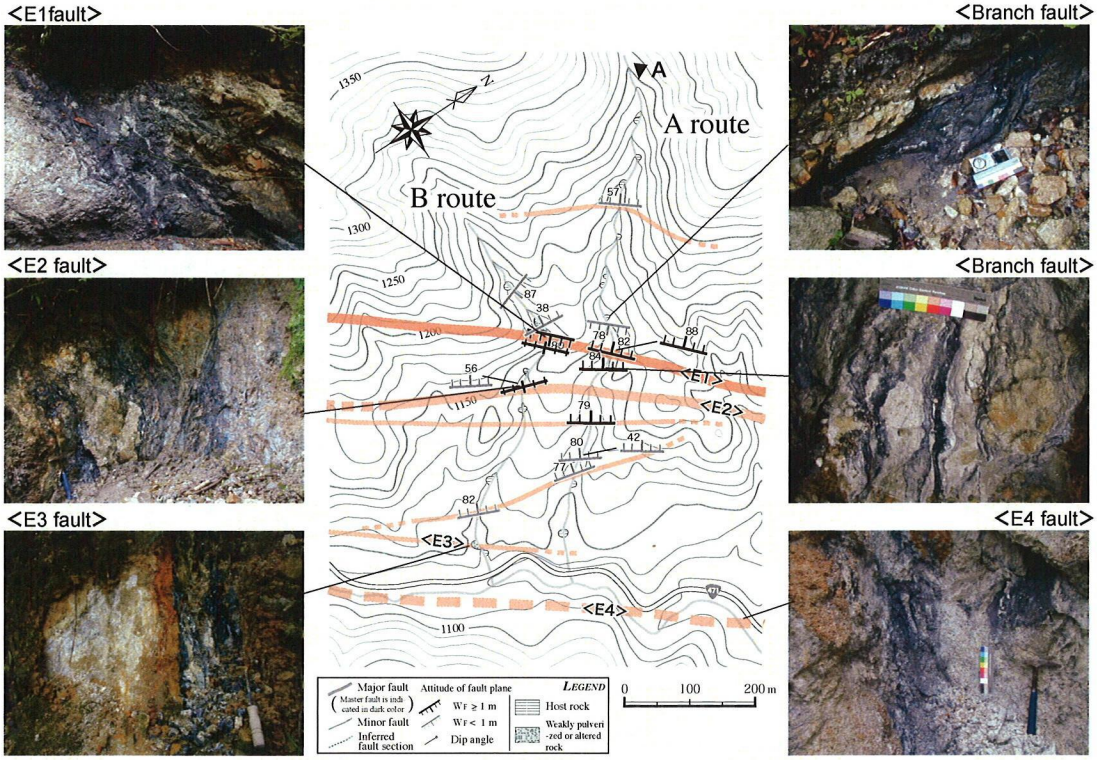

Fig. 2.7. Route map and photographs of the graphite-bearing blackish fault zones along the Ushikubi fault. See Fig. 2.5 for the location.

making thin-section for incohesive fault rock are newly developed and reported in Oohashi et al., (2008). The double-polished thick sections (approximately 100μm in thickness) were made on several rock samples for fluid inclusion analysis.

2-4. Results

More than three fault outcrops which are composed of cohesive graphitic cataclasite, and several graphitic cataclasite floats (fragments) are newly found from the survey along the central portion of the Ushikubi fault, Atotsugawa fault system. This section summarizes the fault structure of each of the three outcrops and one cataclasite fragment that are studied in detail. Each constituent fault strand of the Ushikubi shear zone is named by Oohashi (2008 MS) and Oohashi and Kobayashi (2008) (see Figure 2.5).

2-4-1. Graphite-bearing cataclasite from the B1 strand of the Ushikubi fault

The B1 strand of the Ushikubi fault which located in northeast of the study area (the Shirakimine subarea), strikes ENE-WSW and dips almost vertical. The blackish fault zone shown in Figure 2.8 is a component of SW portion of the B1 strand. Fault zone has 20–30 centimeter in width and is consists of discrete fine cataclasite zone (few centimeter in width) and weakly deformed cataclasite with wavy foliation. Host rock is consists of crystalline limestone (marble) which contains minor amount of graphite flakes. From the observation on polished section and thin section, jagged blackish stylolites are frequently found from weakly deformed cataclasite. These stylolites are usually parallel or subparallel to the fault zone, and basically does not accompany shear deformation. However they transforms to the minor fault near the discrete cataclasite zone. According to the laser Raman spectroscope and SEM-EDS analyses, graphite is commonly detected from these blackish stylolites. On the other hand, quartz veins almost perpendicular to the fault and stylolite are developed in the cataclasite. Pod-like quartz veins are also recognized. Additionally, quartz veins and stylolites show crosscutting relationship.

2-4-2. Cataclasite fragment from the B2 strand of the Ushikubi fault

The B2 strand of the Ushikubi fault, which is located in northeast of the study

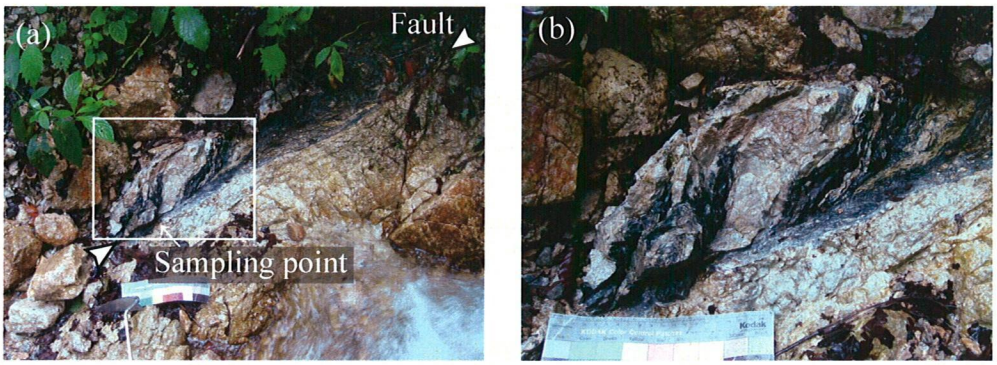

Fig. 2.8. (a) Photograph of the graphite-bearing cataclasite from B1 strand of the Ushikubi fault. (b) Enlargement view of the blackish cataclasite. Alternation of graphite concentration and lens of leucocratic limestone (host rock) defines wavy foliation parallels to the P-surface.

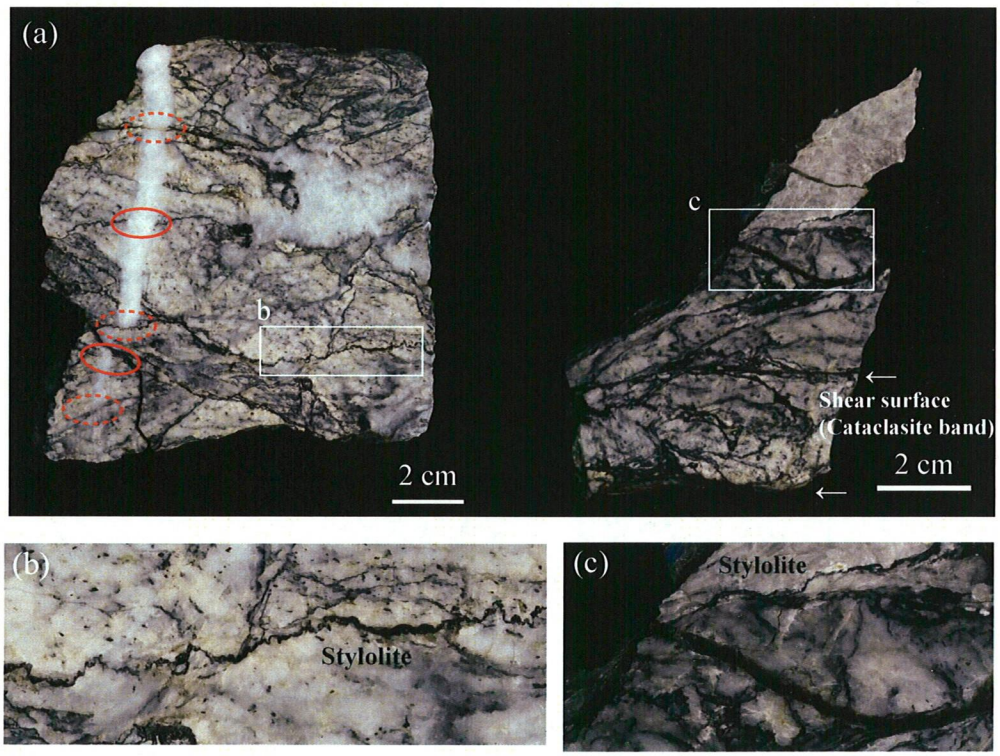

Fig. 2.9. (a) Polished sections of the graphite-bearing cataclasites from B1 strand of the Ushikubi fault. Crosscutting relation is recognized between the stylolites and the quartz vain. Red solid circles showing the stylolite cutted by the quartz vein, and dotted lines shows the veins cutted by the stylolites. (b, c) Enlargement view of the stylolites. Hostrock crystalline limestone contains minor amount of graphite flakes.

area (the Shirakimine subarea). In this area, fault system of the Ushikubi fault shows flat-ramp geometry, and the B2 strand corresponds to ramp fault, which strikes N-S and dips almost vertical. Around this strand, blackish fault gouges are widely exposed. Blackish fault zone in Figure 2.10 has approximately 10 m in width, and mainly composed of incohesive, clayey fault gouge and fault breccia. Within the fault gouge, fragments of cohesive cataclasite (few to 20 cm in diameter) are often found. Mostly fragmented cataclasites show crystalline limestone parentage, and accompany blackish seam in it. Polished section and thin section of these fragments (Figure 2.10d) shows

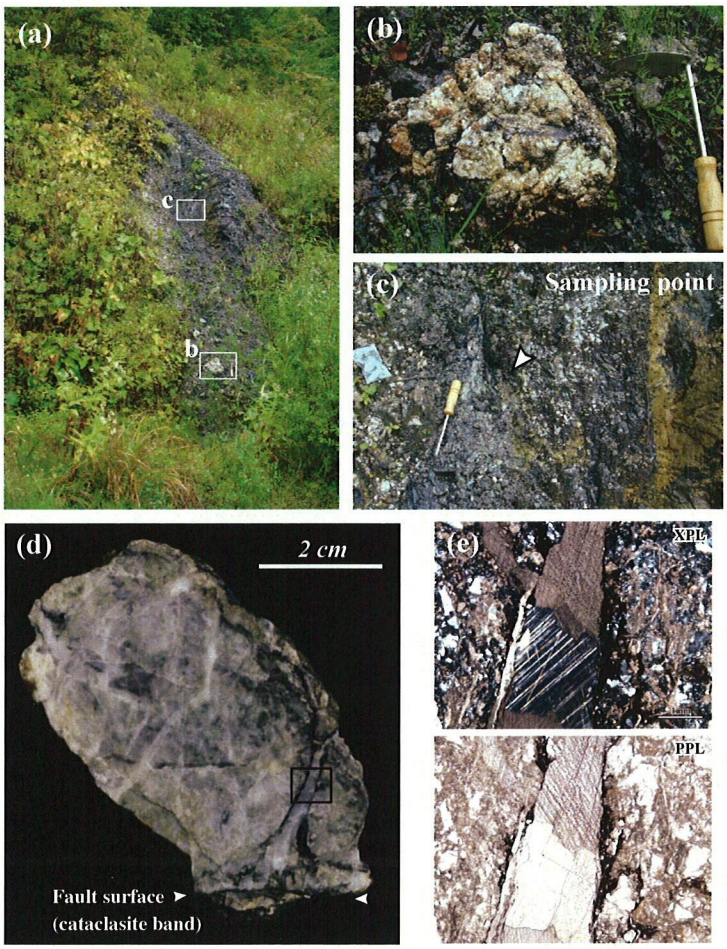

Fig. 2.10. (a) Photograph of the graphite-bearing fault zone from B2 strand of the Ushikubi fault. (b) Flagmented cataclasite of crystalline limestone within the fault gouge zone. (c) Sampling point of cataclastic fragment. (d) Polished section of of cataclastic fragment. Black seam is recognized along the wall of the dilated vein of calcite. (e) Microscopic photographs of calcite vein.

distribution of blackish seam along the wall of the dilated vein of calcite. Calcite shows euhedral form without obvious zoning, and includes small broken pieces of blackish seam. SEM observation with EDS analysis revealed that the existence of graphite from blackish seam. Graphite along the vein of calcite appears as euhedral, flake graphite. These are typically co-exists with euhedral illite.

2-4-3. Graphite-bearing cataclasite and injection veins from the E3 strand of the Ushikubi fault

The E2 strand of the Ushikubi fault which located in central of the study area (the Harayama subarea), strikes ENE-WSW and dips vertical or high angle NW dipping. The blackish fault zone shown in Figure 2.11 is a master fault of the E3 strand which has approximately 20 m in width. Greater part of the fault zone consists of cohesive cataclasite except for the clayey gouge zone developed in the southwest margin of the zone. Two types of cataclasite of highly deformed blackish cataclasite and highly deformed leucocratic cataclasite are found from the observation. Along the Blackish cataclasite zone, black injection veins (Figure 2.10c to e) are frequently found. Additionally, dilatational jog which is filled with black matrix is observed near the cataclastic fault zone. According to the laser Raman measurement of injection vein, graphite is detected from the matrix. SEM observation also supports the existence of aggregate of flake graphite (Figure 2.12). Graphite aggregate is characterized by absence of clashed fragments. In general, flake graphites are concentrated along the wall surface of the dilatational crack.

2-4-4. Graphite-bearing fault zone from the E1 strand of the Ushikubi fault

The E1 strand of the Ushikubi fault which is located in southwest of the study area (the Mizunashi subarea), strikes ENE-WSW and dips almost vertical. The blackish fault zone shown in Figure 2.13 is a component of the E1 strand. Fault zone consists of incohesive, clayey fault gouge zone and fault breccia zone ($\approx$ 2 m in width). Along with the fault zone, damage zone which is characterized by development of narrow cataclastic shear bands (few mm in thickness) are accompanied. Cataclasite samples with undeformed biotite gneiss are collected from 2 m away from the fault zone. According to the observation on polished section and thin section, three types of

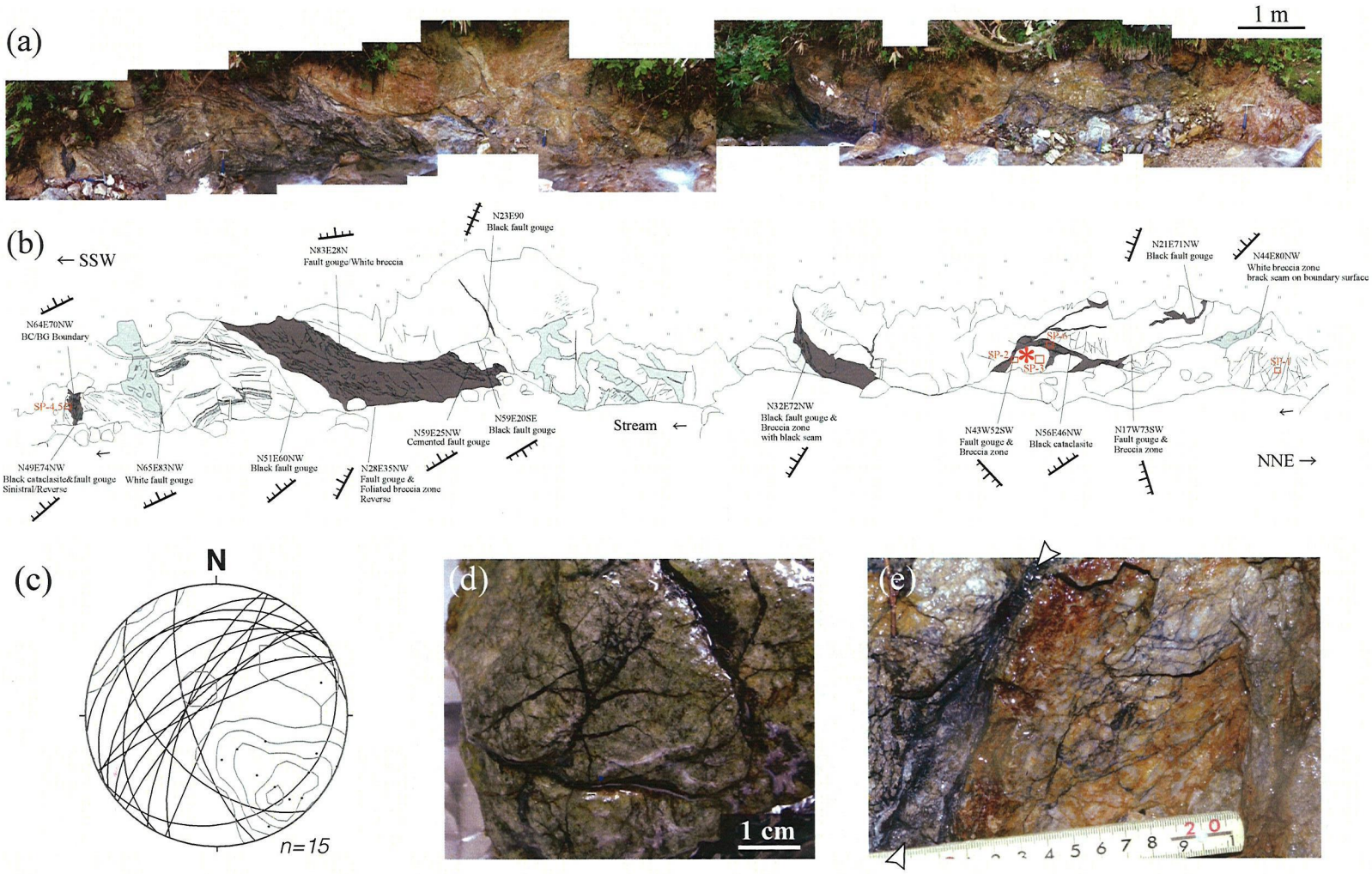

Fig. 2.11. (a) Photograph of the graphite-bearing fault zone from E2 strand of the Ushikubi fault. (b) Sketch of the outcrop. Dark and light shadow corresponds to the highly and weakly deformed blackish cataclasite and fault gouge zone, respectively. (c) Lower-hemisphere, equal-area stereographic projection of fault surfaces. The great circles show attitude, and black dots show pole of the fault surfaces, respectively. (d) Blackish injection veins accompanied with the cataclasite zones. (e) Blackish fault gouge zone (white arrow) and injected vein network .

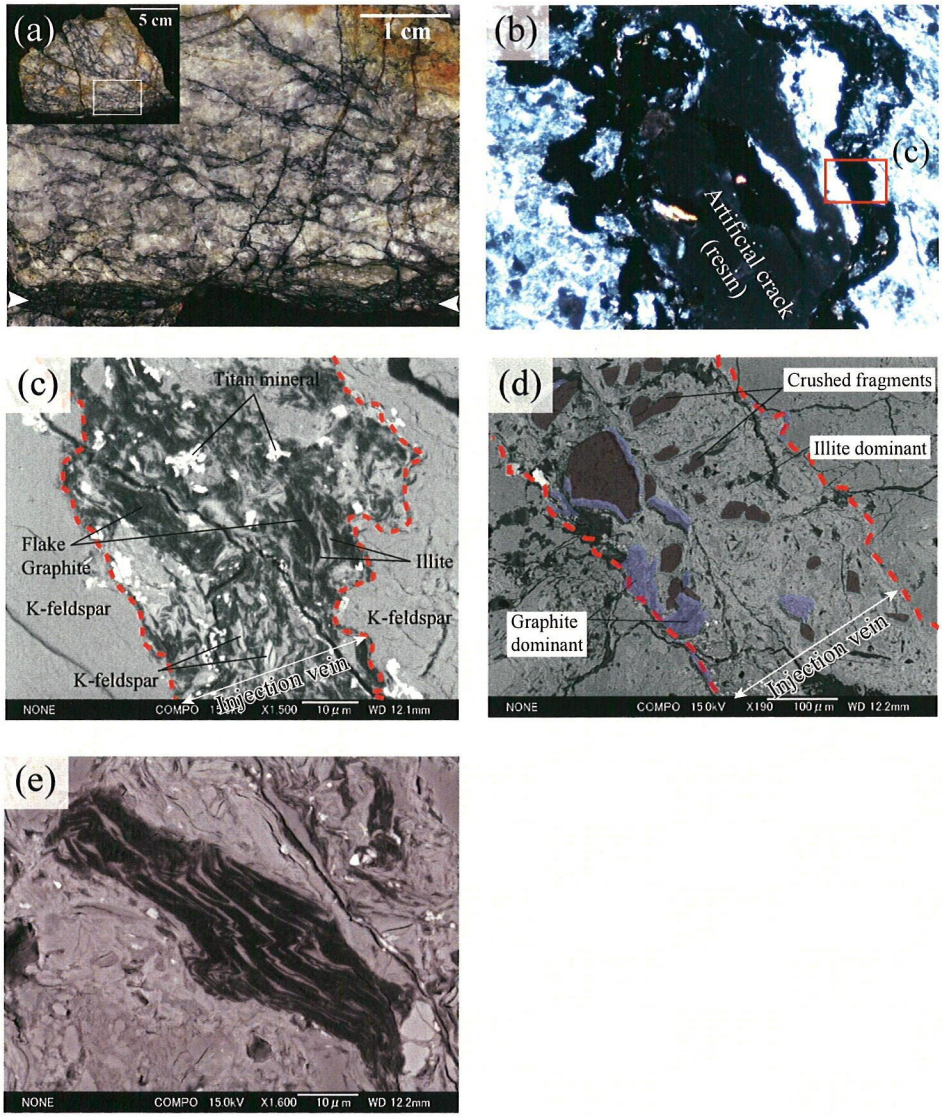

Fig. 2.12. (a) Photograph of polished section of graphitic cataclasite and injection veins from E2 strand of the Ushikubi fault. White arrows show the location of cataclasite band. (a) Photograph of blackish injection vein under optical microscope (XPL). (c, d) SEM images of blackish injection vein. (e) Magnified image of euhedral flake graphite within the injection vein .

microstructure are found (Figure 2.13c to e), that is, (1) undeformed original texture, (2) discontinuous, incipient shear surface and (3) minor fault zone. Texture 1 is characterized by lack of deformation except for original gneissosity which defined by weak orientation of biotite and graphite. Texture 2 corresponds to the minor shear

surface which is hardly distinguished from the comminution of the surface. Stretched graphite along the surface is frequently found within the specimen. Texture 3 is characterized by blackish cataclastic band (few mm in width) with fine matrix. To see the relationship between textural development (shearing) and amount of graphite, image analysis was done for the thin section images under the optical microscope. The results shown in Figure 2.14 clearly demonstrate that the apparent content of graphite increases with deformation from original content of 2–3 % to more than 14 %. Although content of undeformed hostrock varies from 1–9 % depends on the measuring localities, more than 10 % of graphite were only recognized from Texture 3. To investigate the concentration mechanism along this narrow fault, detailed textural observation was done. As a result, a number of stylolites were found from the inside of the fault. Stylolites are basically oriented subparallel to the fault surface (Y shear), and parallel to the P foliateon. Along the fault zone, pressure solution seams were also recognized. On the other hand, the kind of injection vein which was observed from E1 strand was not recognized from this outcrop.

2-5. Discussion

2-5-1. Pressure solution as a possible mechanism for carbon-enrichment

According to the field survey and analysis of fault rock, two petrological features are closely related to the cataclasite enriched in graphite along the Ushikubi fault. Firstly, cataclasite from B1 and E1 fault frequently bears stylolite which is evidence of pressure solution near/within the fault zone. Additionally, remarkable increment in graphite was detected from the cataclasite band of E1 fault which abounds in stylolite. Pressure solution is a solution-precipitation process enhanced by pressure and existence of fluid, and is common in low-grade deformation. Pressure solution can locally be enhanced by elevated pressure (for example in strain caps aside a rigid object) or abundant fluid flow. Localized pressure solution is often concentrated along the surfaces that may originate as joint or fractures especially in limestone (Dunne and Hancock, 1994). And these surfaces are usually highly indented due to the preferred pressure solution. Stylolites are generally enriched in insoluble materials such as opaque mineral and mica because of dissolve and escape of soluble minerals along the surface.

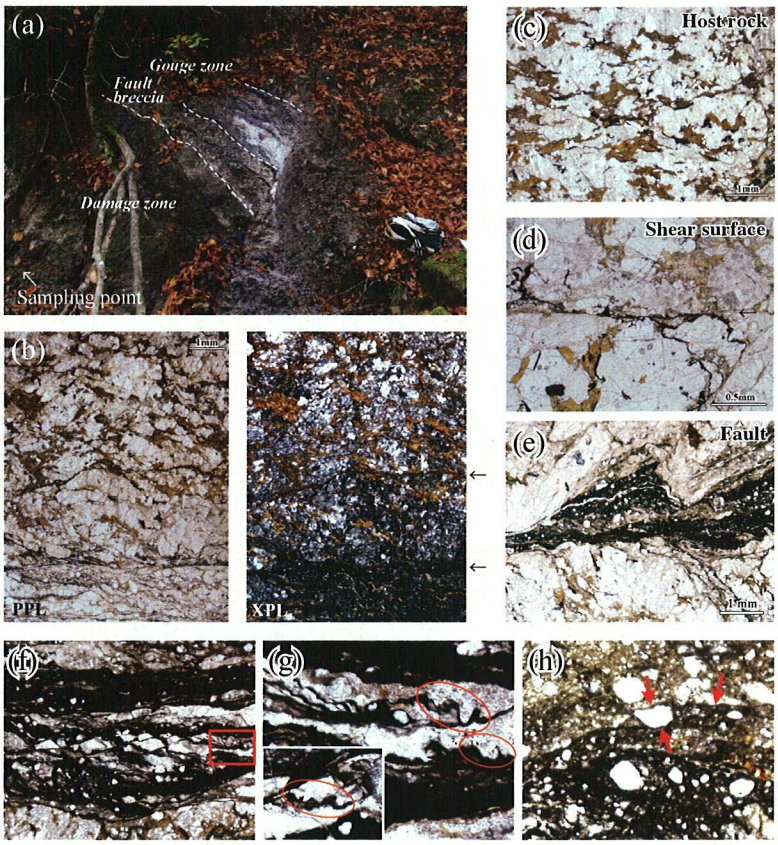

Fig. 2.13. (a) Photograph of the graphite-bearing fault zone from E1 strand of the Ushikubi fault. (b) Thin section of the cataclastic shear band (arrows) and undeformed host rock (upper part). (c) Weak gneissosity defined by foliation of biotite and graphite in host rock. (d) Elongated graphite along the shear surface. (e) Cataclastic shear band (blackish fault) within the damage zone. (f) Photomicrograph of cataclastic sherar band. Composite planar fabrics are depeloped within the zones. (g) Stylolites or slickolites (red circles) parallel to the P-foliaton are often found within the shear band. (f) Pressure solution seams (red arrows) within the shear band.

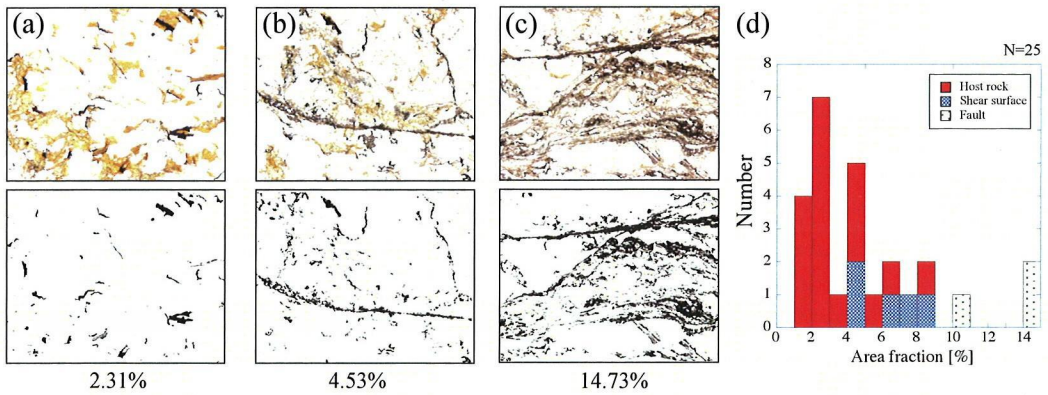

Fig. 2.14. Representative results of image analysis for (a) host rock, (b) shear surface and (c) cataclastic fault. NIH image software is used for the analysis. (d) Histograms of the apparent graphite content for host rock, shear surface and cataclastic fault zone, respectively.

This may regarded as concentration mechanism of carbon along the fracture surface since carbonaceous materials are insoluble materials in comparison with other rock forming minerals such as quartz or calcite. The occurrence from B1 strand suggests that the formation of stylolites and concentration of flake graphite originally contained in the host rock marble, has happened prior to the formation of fault. Weakness of graphite possibly led to the subsequent faulting. On the other hand, there is no visible development of stylolites in the hostrock of E1 fault in spite of existence of graphite in it. However, marked enrichment was observed only from stylolite-bearing fault. This fact suggests that the concentration of graphite occurred after the formation of fault. Take into account of no obvious enrichment along the discontinuous shear surface, enhanced fluid flow due to the formation of continuous fault zone may lead to significant pressure solution and subsequent graphite enrichment within the zone.

2-5-2. Vein graphite as an evidence for "active" carbon-enrichment

On the other hand, the graphitic cataclasite from B2 and E3 fault zones appear different from those of B1 and E1 fault in petrographic feature. These cataclasites characteristically accompany with blackish veins which consist of euhedral graphite flakes, and I can hardly find pressure solution seam or stylolite in it. Graphite is usually considered to forms by maturation of organic matter due to the relatively high P/T metamorphism. Therefore, euhedral graphite generally appears in matrix of metamorphosed rocks rich in carbon. However, vein-filling graphite is also reported from several graphite deposit in Sri Lanka (Katz, 1987), New Hampshire, USA (Rumble and Hoerign, 1986), and so on. The graphite occurs as flakes (or clusters of flakes) or rounded, nodule-like aggregates (Crespo et al., 2006) and is considered to precipitate from C-O-H reduction fluid. Basically, graphite aggregate within the vein along the Ushikubi fault does not contain crushed fragments but coexists with low-temperature hydrothermal minerals like euhedral illite or calcite. Furthermore, evidence of melt is hardly recognized. These features suggest that graphite was formed by not mechanical segregation, crystallization from melt or in situ metamorphism but precipitation by fluid, same as other vein graphite. This is a first report to discover the fluid-precipitated graphite vein along the brittle fault zone. Elevated temperature can be required to the precipitation of graphite at relatively shallow depth (brittle regime). Take into account of graphite often appears only along the wall of the dilated vein or margin

of the crushed fragment, graphite precipitation can be regarded as a transient phenomenon just after the dilation of cracks. Such transient temperature rise along the fault is attributable to the frictional heat or inflow of high-temperature fluids. Hydrogen may be produced by free-radical reaction of newly-formed mineral surfaces and water during faulting (Kita et al., 1982).

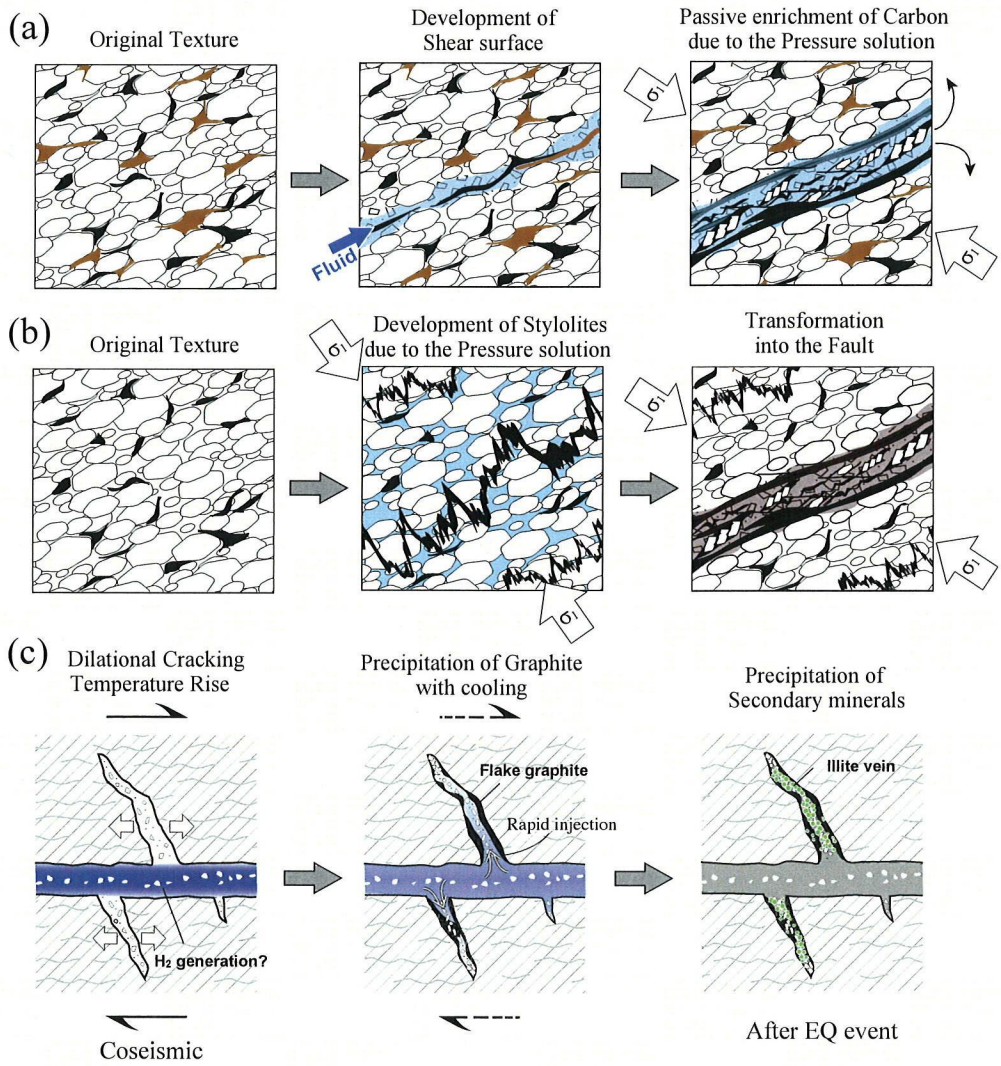

Fig. 2.15. Possible origins of graphite-enriched fault zones along the Ushikubi fault. (a) Pressure solution driven, passive enrichment of graphite within the fault zone, (b) stylolite-related fault and (c) active enrichment due to the vein-graphite precipitation accompanied with brittle faulting. Pressure solution process is essential for both (a) and (b).

2-5-3. Spatial distribution of graphitic fault zones along the Atotsugawa and Ushikubi fault zone

Notable feature on the Ushikubi fault is widespread outcropping of graphite bearing fault zone such as in Figure 2.1. Histogram in Figure 2.6 shows frequency of blackish fault zone characterized by existence of graphite, along the central portion of the Ushikubi fault. To simplify, histogram is shown in each divided subareas, but in central and northeastern subarea that extends at least 10 km along the master fault, shows strikingly high frequency on appearance of graphite bearing fault.

2-6. Conclusion

The first aim of this Chapter 2 is to determine the mechanism for carbon enrichment along the fault zones base on the field survey and fault rock analysis. I revealed two different processes for graphite enrichment along the fault zone. One is a pressure solution process: it enhances the mass transfer of water-soluble minerals such as quartz and carbonates and the enrichment of insoluble minerals such as carbon and metals along the fault zones. The other process is the precipitation of graphite from high-temperature carbon-rich fluid: this type of graphite typically appears as injection veins within the cataclasitic fault zones. The two processes lead to ~15 wt% of graphite concentration in the Atotsugawa fault zones, while their hostrock contains only 0~3 wt% of graphite.

3. Frictional properties of carbonaceous fault gouge; Graphite, amorphous carbon and natural carbonaceous fault gouge

3-1. Introduction

Among carbonaceous minerals, graphite is well known as a classical-solid lubricant (e.g. Savage, 1948) owing to its low friction coefficient, and has been used in industrial field. However, the importance of graphite in earth science, especially for faulting or deformation mechanism is not well examined up to now in spite of it exists as natural mineral and is found from the fault/shear zones. And there is no report of frictional experiment of graphite and its precursor, amorphous carbon for the purpose of applying to fault mechanics, except for Moore and Lockner (2004). They conducted frictional experiments for 0.6 mm-thick simulated graphite gouge under the normal stress of 100 MPa and slip rate of 0.5 μm/s. The friction varied from peak friction coefficient of ~ 0.2 to steady-state friction coefficient of 0.15 for both dry and water-saturated conditions. Consequently, first purpose is to determine the mechanical significance of carbonaceous materials on fault by examining how frictional properties change from pure amorphous carbon to graphite gouge at a wide range of slip rate.

Another interesting aspect of this study is the characterization of frictional properties for amorphous materials at a wide range of slip rate. Amorphous materials are known to form during friction experiments (Yund et al., 1990) and formation of silica gel or amorphous wet materials is suggested to cause dramatic fault weakening at intermediate to high slip rates (Goldsby and Tullis, 2002; Di Toro et al., 2004). High-velocity gouge experiments also produced amorphous materials in decomposed kaolinite (Brantut et al., 2008) due to frictional heating. Mineral decomposition during seismic fault motion was confirmed also by Han et al. 2007a, 2007b; Hirose and Bystricky, 2007) although presence of amorphous materials was not reported. Formation of amorphous materials seems to be a wide-spread phenomenon in fault zones, but the mechanical properties of amorphous geomaterials have not been investigated systematically, except for coal (O'Hara et al., 2006). Thus, our experiments for amorphous carbon may provide insight into the possible role of amorphous materials

on mechanical properties of fault zone.

3-2. Experimental procedures

I used three starting materials for simulated fault gouge: (1) synthetic amorphous carbon powder (angular shape and grain size <45 μm, Strem Chemicals, Inc., product number 93-0601, see Figure 3.1 a), (2) highly crystallized natural graphite (platy shape and grain size <45 μm, Wako Pure Chemical Industries, Ltd., product number 072-03845, Figure 3.1 b) and (3) natural carbonaceous fault gouge (Grain size: <105 μm). Natural carbonaceous fault gouge (3) is black, clayey fault gouge collected from the fault outcrop of the Tanakura Tectonic Line and Ushikubi fault, Atotsugawa fault system. The fault gouge of the Tanakura Tectonic Line is collected from G3 gouge zone in Figure 2.2 (Natural Fault Gouge TTL in Table 1). Another carbonaceous fault gouge was taken from the Ushikubi fault, central Japan (Natural Fault Gouge UF in Table 1). Occurrence between the fault gouge on two faults is well resemble, and based on X-ray diffraction analysis, both of fault gouges are composed of quartz, orthoclase, illite, smectite, graphite and small amount of pyrite and titanium minerals. Almost 10 wt% of carbonaceous materials is contained within the fine particles of the fault gouge. For experimental uses, Fragments >105 μm are eliminated from the sample by sieving.

Friction experiments were performed using a rotary-shear, high-velocity friction apparatus (HVR) at Kochi/JAMSTEC (Shimamoto and Tsutsumi, 1994; Hirose and Shimamoto, 2005) and a rotary-shear, low to high-velocity friction apparatus

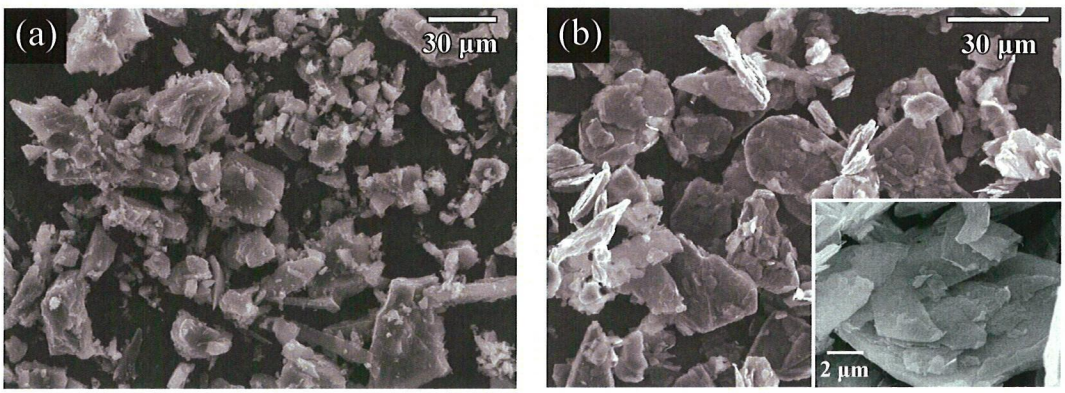

Fig. 3.1. SEM microphotographs of (a) amorphous carbon and (b) graphite powder used for the experiments. Original grain size varies from 50 to few microns in diameter (mean diameter ≈40 μm).

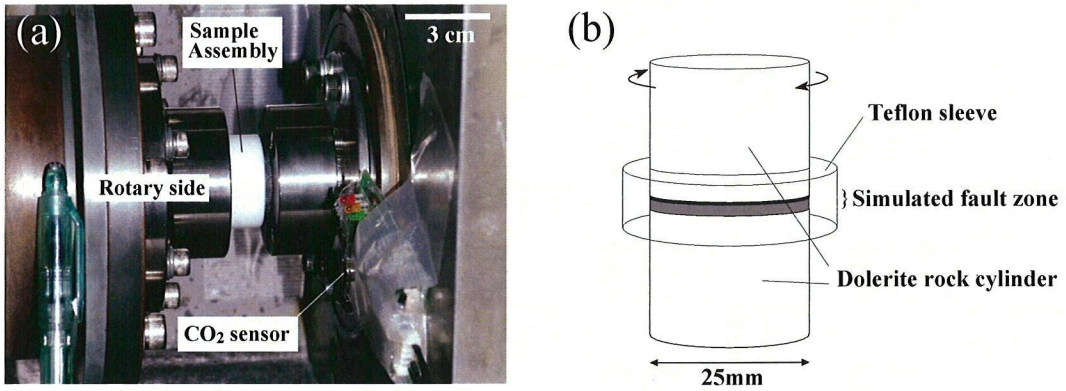

Fig. 3.2. (a) Photograph showing the specimen chamber of the HVR apparatus including placement of the CO_2 sensor. (b) Specimen configuration used in this study.

(HDR) at Hiroshima University (Shimamoto and Hirose, 2006). The experiments were conducted at normal stresses (σ_n) of 0.5 to 2.8 MPa, equivalent slip rates (V_e) of 50 μm/s to 1.3 m/s, and displacements of 0.09 to 118 m. Because the slip rate increases from the center to the periphery of the cylindrical specimens, I used the equivalent slip rate, V_e, defined such that $\tau V_e S$ gives the rate of total frictional work on a fault with area S, assuming a constant shear stress τ over the fault surface (Shimamoto and Tsutsumi, 1994). Hereafter, for convenience, I refer to "equivalent slip rate" as simply "slip rate" or "velocity".

Some experiments for graphite gouge and natural carbonaceous fault gouge were conducted using a high-temperature biaxial friction apparatus (HTB) at Hiroshima University (Noda and Shimamoto, 2009), to obtain more precise frictional data and to achieve higher normal stress (more than 10 MPa) than rotary-shear friction apparatus.

Simulated fault gouge was placed between two cylinders of dolerite host rock with 25.0 mm diameters whose end surfaces were ground with SiC 80# powder (see Figure 2c). A Teflon sleeve of 24.9 mm in inner diameter was attached around the simulated fault zone to prevent gouge leakage. To correct for the effect of friction between the Teflon sleeve and the cylinders, I measured the shear traction caused by the sleeve in experiments without gouge, and then subtracted that traction from the measured raw data (see details in Appendix A). Thus, the effect of the Teflon sleeve is removed from the frictional data reported in this paper.

All starting materials and host rock cylinders were dried in an oven at 80 °C for at least 48 hours before experiments. The experiments with HVR and HDR used 0.3

g of amorphous carbon, 0.5 g of highly crystallized graphite or 1.0 g of natural carbonaceous fault gouge to provide a consistent gouge thickness at about 1 mm for all runs. The experimental conditions and results are summarized in Table 1.

3-3. Results

3-3-1. Representative slip behaviors

Figure 3.3 shows a representative experimental result for amorphous carbon gouge subjected to a slip rate v of 1.3 m/s and normal stress σ_N of 1.4 MPa. Friction increased rapidly to an initial peak friction coefficient μ_p (0.56) and then decreased exponentially with displacement toward a steady-state friction coefficient μ_{ss} (0.12) over a slip-weakening distance D_c (12.9 m). This behavior can be described by an empirical equation (Mizoguchi et al., 2007; see dashed line in Figure 3.3):

$$\mu = \mu_{ss} + (\mu_p - \mu_{ss}) \exp [\ln(0.05)(D/D_c)] \qquad (2)$$

where D is the fault displacement after the peak friction and D_c is the slip-weakening distance over which $\mu - \mu_{ss}$ falls to 5% of $\mu_p - \mu_{ss}$. Experimental data for amorphous carbon were fit with this equation (Table 1).

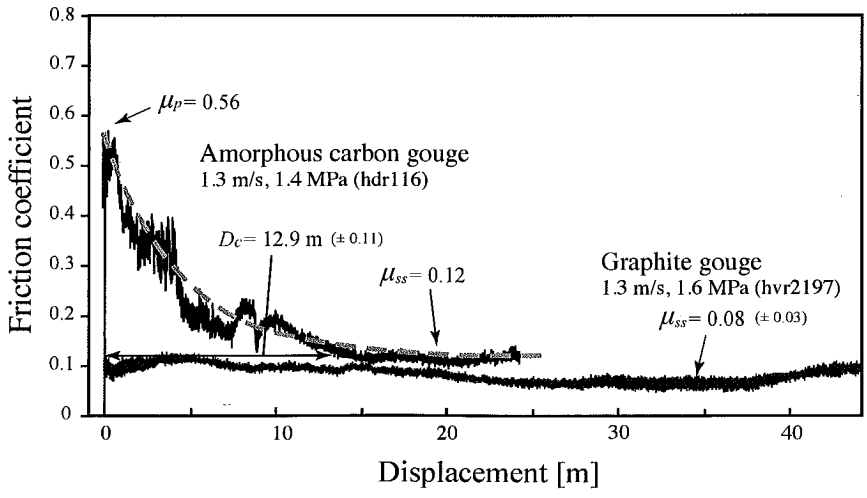

Fig. 3.3. Representative frictional behavior of amorphous carbon (black line) and graphite gouge (grey line) at a slip rate of 1.3 m/s and normal stresses of 1.4 MPa (amorphous carbon) and 1.6 MPa (graphite). Dashed line is a least-squares fit to the slip-weakening behavior with an empirical equation (Eq. 5).

Table 1
Summary of experimental data reported in Chapters 3 and 5.

Run No.	Material	Atmospheric Condition	Velocity [m/s]	Normal stress [MPa]	Displace -ment [m]	Peak Friction τ [MPa]	Peak Friction μ	Steady-state friction τ [MPa]	Steady-state friction Error	Steady-state friction μ	D_c [m]	Remarks	XRD measurement of recovered gouge: Slipping zone d_{002} [Å]	Slipping zone Int. [cps]	Undeformed zone d_{002} [Å]	Undeformed zone Int. [cps]	
hvr1546	Graphite	Air	1.3	1.01	11.8	0.17	0.17	–	–	–	–	*					
hvr1549	Graphite	Air	1.3	1.0	47.95	[b]	–	0.09	±0.01	0.09	–						
hvr1555	Graphite	Air	0.87	1.0	83.28	[b]	–	0.1	±0.02	0.1	–	CO_2 monitoring (Max: 40 ppm)					
hvr1558	Amorphous Carbon	N_2	1.3	1.0	16.2	0.70	0.70	0.15	±0.02	0.15±0.02	14.7						
hvr1561	Amorphous Carbon	Air	1.3	1.0	11.0	0.63	0.62	0.13	±0.02	0.19	38.2	CO_2 monitoring (Max: 160-180 ppm)					
hvr1556	Graphite	Air	0.43	1.0	38.01	[b]	–	0.14	±0.02	0.13	–						
hvr1557	Graphite	Air	0.043	1.0	7.6	[b]	–	0.13	±0.01	0.13	–						
hvr1560	Amorphous Carbon	Air	1.3	1.0	22.0	0.59	0.59	0.18	±0.03	0.18	13.7						
hvr1564	Graphite	Air	1.3	1.0	43.8	[b]	–	0.12	±0.02	0.12±0.02	–						
hdr050	Amorphous Carbon	N_2	1.3	1.0	17	0.52	0.52	0.17	±0.02	0.15±0.05	11.0		3.333	524	3.358	170	
hdr051	Amorphous Carbon	N_2	1.3	2.0	23.7	0.84	0.42	0.24	–	0.11	12.0						
hdr066-1	Amorphous Carbon	Air	0.04	1.0	2.94	0.57	0.57	0.57	±0.05	0.54±0.05	[a]						
hdr066-2	Amorphous Carbon	Air	0.009	1.85	17.13	1.0	0.56	1.0	±0.02	0.51±0.02	[a]		3.36?		No peak		
hdr114	Amorphous Carbon	N_2	0.009	2.0	15.0	[b]	–	0.87	±0.02	0.43±0.02	–						
hdr115	Amorphous Carbon	N_2	1.3	2.0	29.5	1.11	0.6	0.36	±0.03	0.19	2.5		3.343	162			
hdr116	Amorphous Carbon	N_2	1.3	1.4	32.6	0.78	0.56	0.17	±0.01	0.12	12.9						
hdr117	Amorphous Carbon	N_2	1.3	1.44	18.7	0.61	0.53	0.3	–	0.21	7.3						
hdr119	Amorphous Carbon	N_2	1.3	2.0	35.4	1.28	0.59	0.27	–	0.13	9.1						
hdr121	Amorphous Carbon	N_2	1.3	2.0	21.1	1.18	0.58	0.3	±0.05	0.15	6.39		3.346	230	No peak	–	
hdr124	Amorphous Carbon	N_2	1.3	2.0	33.4	1.07	0.58	0.3	±0.02	0.12±0.02	11.4		3.355	209	No peak	–	
hdr125	Amorphous Carbon	Air	1.3	2.0	27.3	1.1	0.55	0.24	±0.02	0.12	5.8		No peak	–	No peak	–	
hdr192	Amorphous Carbon	N_2	1.3	2.0	30.8	1.21	0.62	0.37	±0.02	0.18	6.7		3.338	464	No peak	–	
hdr193	Amorphous Carbon	N_2	1.3	2.8	28.2	1.42	0.51	0.46	–	0.16	4.2		3.347	223	3.353	160	
hdr194	Amorphous Carbon	Air	1.3	2.0	43.0	1.14	0.57	0.28	±0.05	0.12	12.7						TC
hdr195	Amorphous Carbon	N_2	1.3	2.0	31.3	1.13	0.59	0.40	±0.05	0.15	[a]		3.338	331	3.348	459	TC
hdr196	Amorphous Carbon	N_2	1.3	2.0	28.0	0.92	0.46	0.36	–	0.13	7.3						
hdr197	Amorphous Carbon	N_2	1.3	2.0	32.7	1.01	0.51	0.29	±0.03	0.15	9.2						
hdr198	Amorphous Carbon	N_2	1.3	2.0	30.6	0.95	0.47	0.24	±0.03	0.11	7.7						
hdr199	Amorphous Carbon	N_2	1.3	2.0	25.5	1.02	0.51	0.19	±0.005	0.09	10.45						
hvr2264	Amorphous Carbon	Air	0.00022	2.0	36.5	[b]	–	1.05	±0.04	0.53±0.02	–		No obvious peak		No obvious peak		
hdr623-0-1	Graphite	Air	0.00016	1.85	0.17	[b]	–	0.17	±0.02	0.09	–						
hdr623-0-2	Graphite	Air	0.00005	1.85	0.09	[b]	–	0.17	±0.05	0.09	–						
hdr623-0-3	Graphite	Air	0.0005	1.85	0.16	[b]	–	0.21	±0.01	0.11	–						
hdr623-0-4	Graphite	Air	0.001	1.85	0.16	[b]	–	0.23	±0.01	0.12	–						
hdr623-1	Graphite	Air	0.001	1.85	0.16	[b]	–	0.14	±0.01	0.08	–						
hdr623-2	Graphite	Air	0.004	1.85	1.14	[b]	–	0.16	±0.02	0.09	–						
hdr623-3	Graphite	Air	0.044	1.85	6.4	[b]	–	0.29	±0.01	0.16	–						
hdr623-4	Graphite	Air	0.13	1.85	13.0	[b]	–	0.15	±0.03	0.08	–						
hdr624-0	Graphite	Air	0.00005	1.85	0.05	[b]	–	0.27	±0.01	0.15	–						
hdr624-1	Graphite	Air	0.056	1.85	12.4	[b]	–	0.22	±0.01	0.12	–						
hdr624-2	Graphite	Air	0.056	1.85	6.36	[b]	–	0.19	±0.02	0.10	–						
hdr624-3	Graphite	Air	0.13	1.85	5.5	[b]	–			–	–						
hdr625	Graphite	Air	0.13	1.85	17.1	[b]	–	0.24	±0.01	0.13	–						
hdr626-0	Graphite	Air	0.436	1.85	17.0	[b]	–	0.25	±0.01	0.14	–						
hdr626-1	Graphite	Air	0.436	1.85	25.5	[b]	–			<0.20	–	*					
hdr627	Graphite	Air	0.436	1.85	20.8	[b]	–	0.22	±0.01	0.12	–						
hdr628	Graphite	Air	0.872	1.85	101	[b]	–	0.2	±0.01	0.11	–						
hdr629-0-1	Amorphous Carbon	Air	0.00005	1.84	0.10	[b]	–	0.99	±0.05	0.55	–						
hdr629-0-2	Amorphous Carbon	Air	0.0001	1.84	0.10	[b]	–	0.98	±0.02	0.54	–						
hdr629-0-3	Amorphous Carbon	Air	0.0005	1.84	0.21	[b]	–	1.01	±0.02	0.56	–						
hdr629-0-4	Amorphous Carbon	Air	0.001	1.84	0.36	[b]	–	1.02	±0.04	0.56	–						
hdr629-1-1	Amorphous Carbon	Air	0.005	1.84	0.8	1	0.59	0.96	±0.02	0.55	0.01						
hdr629-1-2	Amorphous Carbon	Air	0.009	1.84	2.1	0.97	0.58	0.9	±0.02	0.51	0.9						
hdr629-1-3	Amorphous Carbon	Air	0.044	1.84	9.4	0.91	0.54	0.59	±0.01	0.32	6.2						
hdr629-2	Amorphous Carbon	Air	0.13	1.84	10.1	0.81	0.50	0.57	±0.03	0.29	[a]						
hdr630-0	Amorphous Carbon	Air	0.436	1.84	15.2	1.23	0.67	0.54	±0.02	0.27	9.8						
hdr630-1	Amorphous Carbon	Air	0.872	1.84	16.8	1.18	0.65	0.28	±0.01	0.15	8.4						
hdr639-0	Amorphous Carbon	Air	1.3	1.95	25.9	1.14	0.57	0.21	±0.01	0.11	9.2						
hvr2187	Graphite	Air	1.3	0.47	103.7	[b]	–	0.04	±0.02	0.09	–						
hvr2188	Graphite	Air	1.3	0.48	102.7	[b]	–	0.04	±0.01	0.08	–						
hvr2189	Graphite	Air	1.3	0.66	118.6	[b]	–	0.06	±0.05	0.09	–						
hvr2190	Graphite	Air	1.3	0.87	94.1	[b]	–	0.1	±0.01	0.10	–						
hvr2191	Graphite	Air	1.3	0.95	68.6	[b]	–	0.11	±0.02	0.11	–						
hvr2192	Graphite	Air	1.3	1.3	67.5	[b]	–	0.13	±0.01	0.10	–						
hvr2193	Graphite	Air	1.3	1.28	84.9	[b]	–	0.13	±0.02	0.10	–						
hvr2194	Graphite	Air	1.3	1.62	78.9	[b]	–	0.16	±0.02	0.10	–						
hvr2197	Graphite	Air	1.3	1.58	58.8	[b]	–	0.17	±0.01	0.11	–						
hvr2199	Graphite	Air	1.3	2.1	47.7	[b]	–	0.26	±0.03	0.12	–						
hvr2200	Graphite	Air	1.3	2.04	65.7	[b]	–	0.21	±0.02	0.10	–						
hvr2201	Graphite	Air	1.3	2.44	40.7	[b]	–	0.25	±0.04	0.10	–						
hvr2202	Graphite	Air	1.3	2.48	60.7	[b]	–	0.26	±0.05	0.10	–						
hvr2198	Amorphous Carbon	Air	1.3	1.84	22.0	1.13	0.61	–	–	–	[a]	*					
hvr2203	Amorphous Carbon	Air	1.3	2.84	17.6	1.69	0.60	0.42	±0.05	0.16	5.43						
hvr2204	Amorphous Carbon	Air	1.3	0.74	62.5	0.47	0.61	0.1	±0.03	0.15	28.6						
hvr2205	Amorphous Carbon	Air	1.3	0.74	57.7	0.48	0.65	0.07	±0.03	0.09	25.1						
hvr2209	Amorphous Carbon	Air	1.3	2.0	23.9	1.29	0.63	0.3	±0.04	0.15	4.4	CO_2 monitaring (Max: 2894 ppm)					

[a] Dc was not well defined due to the noise on shear stress, gouge leakage or overall gradual weakening during experiment.
[b] Peak friction was not recognized.
TC: Temperature measurement by thermocouple.
*: Experiment was stopped during weakening

For similar conditions (σ_n =1.6 MPa and v = 1.3 m/s), graphite gouge showed very different behaviors with much smaller peak friction than for amorphous carbon and with friction remaining nearly constant (μ_{ss} = 0.08) without obvious slip weakening or strengthening throughout the experiment (Figure 3.3). I did not fit graphite data with eq. (2).

3-3-2. Normal Stress Dependence of Friction at slip rate of 1.3 m/s

Figure 3.4a, b and 4c, d shows frictional behaviors of amorphous carbon and graphite gouge at various normal stresses. Initial peak friction and steady-state friction are almost independent on normal stress for both amorphous carbon and graphite gouge. Figure 3.5a and b give shear stress plotted against the normal stress of initial peak and steady state friction at slip rate of 1.3 m/s. The figure shows linear dependence between shear stress and normal stress, which is consistent with a Mohr-Coulomb friction law:

$$\tau = \mu\sigma_n + C \quad (3)$$

μ is the 'intrinsic' friction coefficient and C the cohesive term, respectively. A linear fit of the data on amorphous carbon gives the following values:

$$\tau_p = 0.54\ \sigma_n + 0.007 \quad (4)$$

$$\tau_{ss} = 0.15\ \sigma_n + 0.05 \quad (5)$$

where τ_p is the peak shear stress and τ_{ss} is the steady-state (or residual) shear stress. In the same manner, high-velocity friction experiments on graphite gouge gives following values:

$$\tau_{ss} = 0.11\sigma_n + 0.0006 \quad (6)$$

Amorphous carbon exhibits dramatic, nearly exponential slip-weakening at all normal stresses (Figure 3.4a and b), with peak and steady-state friction coefficients of 0.54 and 0.15, respectively, neglecting very small cohesion terms (Figure 3.5a; see linear equations fit to the data). This friction coefficient is lower than that for most

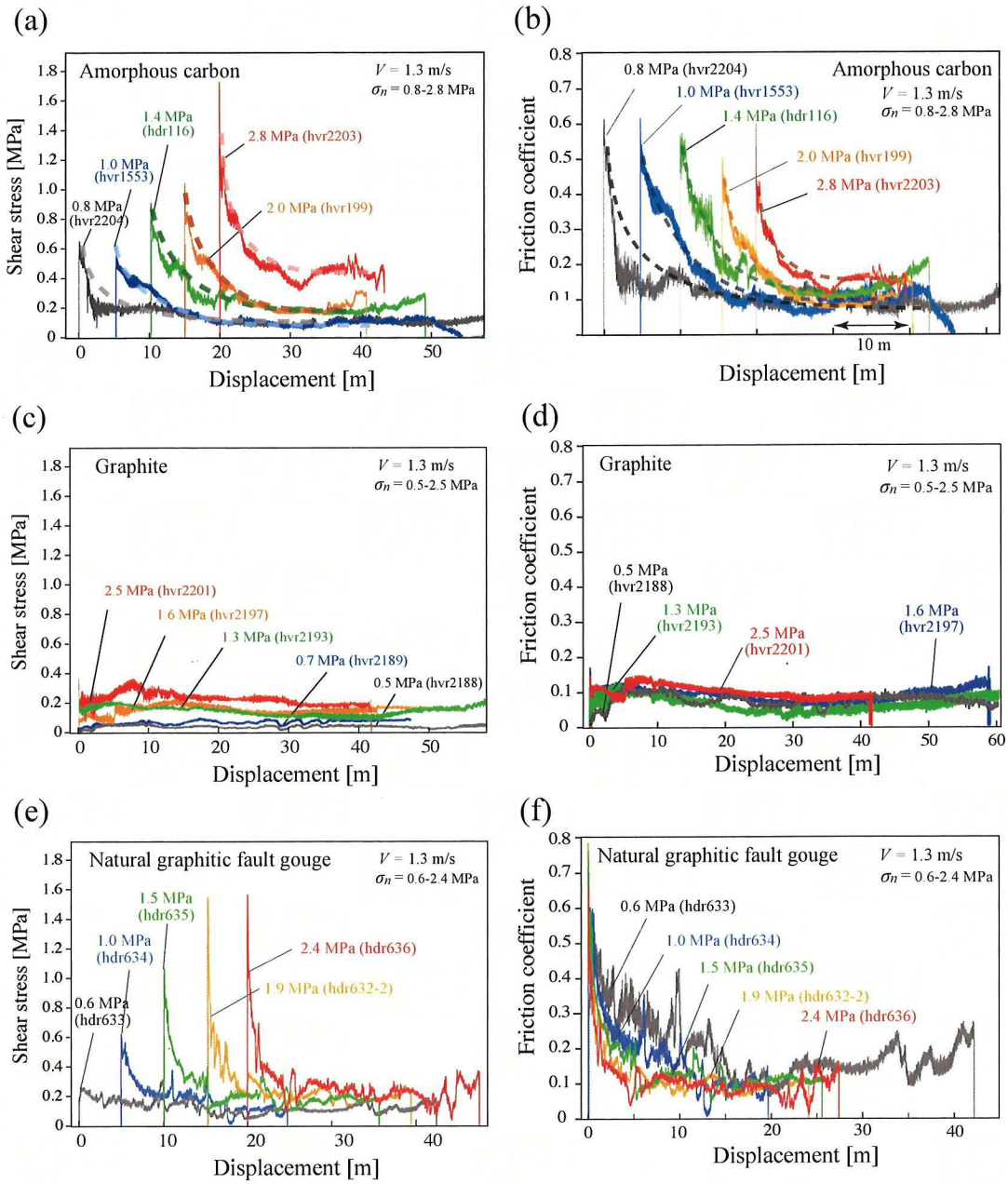

Fig. 3.4. Frictional behavior at various normal stresses of (a, b) amorphous carbon gouge, (c, d) graphite gouge and (e, f) at a slip rate of 1.3 m/s. Left side of figure shows shear stress plotted against displacement (a, c, e) and right side displays friction coefficient plotted against displacement at various normal stresses. Dashed lines are least-squares fitting curves with Eq. (3), and the five trials are shown offset by 5 m for visibility (a, b, e).

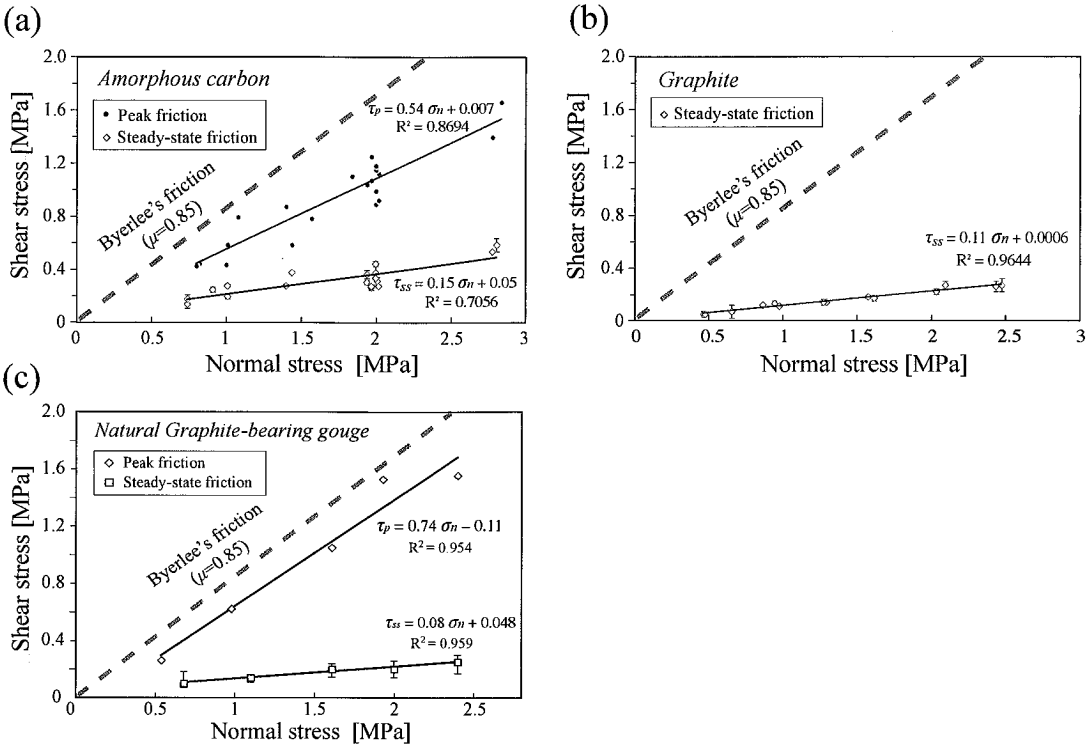

Fig. 3.5. Shear stress is plotted against normal stress at peak and steady-state friction for (a) amorphous carbon gouge, (b) graphite gouge and (c) natural carbonaceous fault gouge from the Ushikubi fault at a slip rate of 1.3 m/s. There is no obvious peak friction from graphite gouge. Byerlee's law ($\tau = 0.85\ \sigma_n$) is shown as a dashed line for comparison.

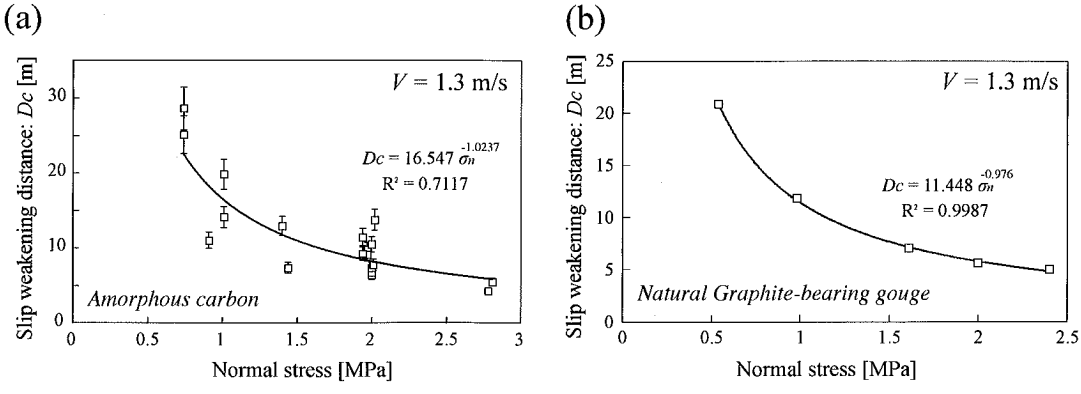

Fig. 3.6. Slip-weakening distance *Dc* plotted against normal stress for (a) amorphous carbon gouge and (b) natural graphite-bearing fault gouge frim the Ushikubi fault at a slip rate of 1.3 m/s. The solid line is a power-law relationship fitting the data.

rocks compiled by Byerlee (1978). Slip-weakening distance D_c decreases from about 25 m to 6 m as the normal stress σ_n increases from 0.8 to 2.8 MPa (Figure 3.6a). On the other hand, graphite shows low friction throughout the tests (Figure. 3.4b and d) with the friction coefficient of 0.11 (Figure. 3.5b).

Figure 3.4e and f shows frictional behaviors of natural graphitic fault gouge from the Ushikubi fault at various normal stresses. Initial peak friction and steady-state friction displays almost independent on normal stress as well as amorphous carbon and graphite gouge. Figure 3.5c give shear stress plotted against the normal stress of initial peak and steady state friction at slip rate of 1.3 m/s. A linear fit of the data on natural graphitic fault gouge gives the following values in the same manner:

$$\tau_p = 0.74\,\sigma_n - 0.11 \quad (7)$$

$$\tau_{ss} = 0.08\,\sigma_n + 0.048 \quad (8)$$

This peak friction coefficient (0.74) is almost comparable to that of other rocks (Byerlee, 1978). Natural graphite-bearing fault gouge also exhibits dramatic slip-weakening at all normal stresses same as amorphous carbon. Slip-weakening distance D_c decreases from about 21 m to 6 m as the normal stress σ_n increases from 0.6 to 2.4 MPa (Figure 3.6b). These relationships are quite comparable to that from Nojima fault gouge examined by Mizoguchi et al. (2007).

3-3-3. Velocity dependence of friction

Frictional behaviors at various slip rates (Figure 3.7) indicate that the friction varies with slip rate for all three of gouges. Peak friction coefficient of amorphous carbon is about 0.55 at all slip rates. But the steady-state friction coefficient decreases from 0.51 to 0.1 as the slip rate increases from 0.04 to 1.3 m/s (Figure 3.7a), whereas it remains nearly the same (about 0.55) at low slip rates (50 μm/s to 5 mm/s) with no slip-weakening (Figure 3.7c). On the other hand, friction coefficient of graphite is low (about 0.1) and remains about the same all throughout the tests (Figures 3.7b and d). This result is comparable to the friction coefficient reported by Moore and Lockner (2004) using a triaxial deformation apparatus at low slip rate (5 μm/s). Frictional behaviors of natural graphite-bearing fault gouge can be divided into three characteristic

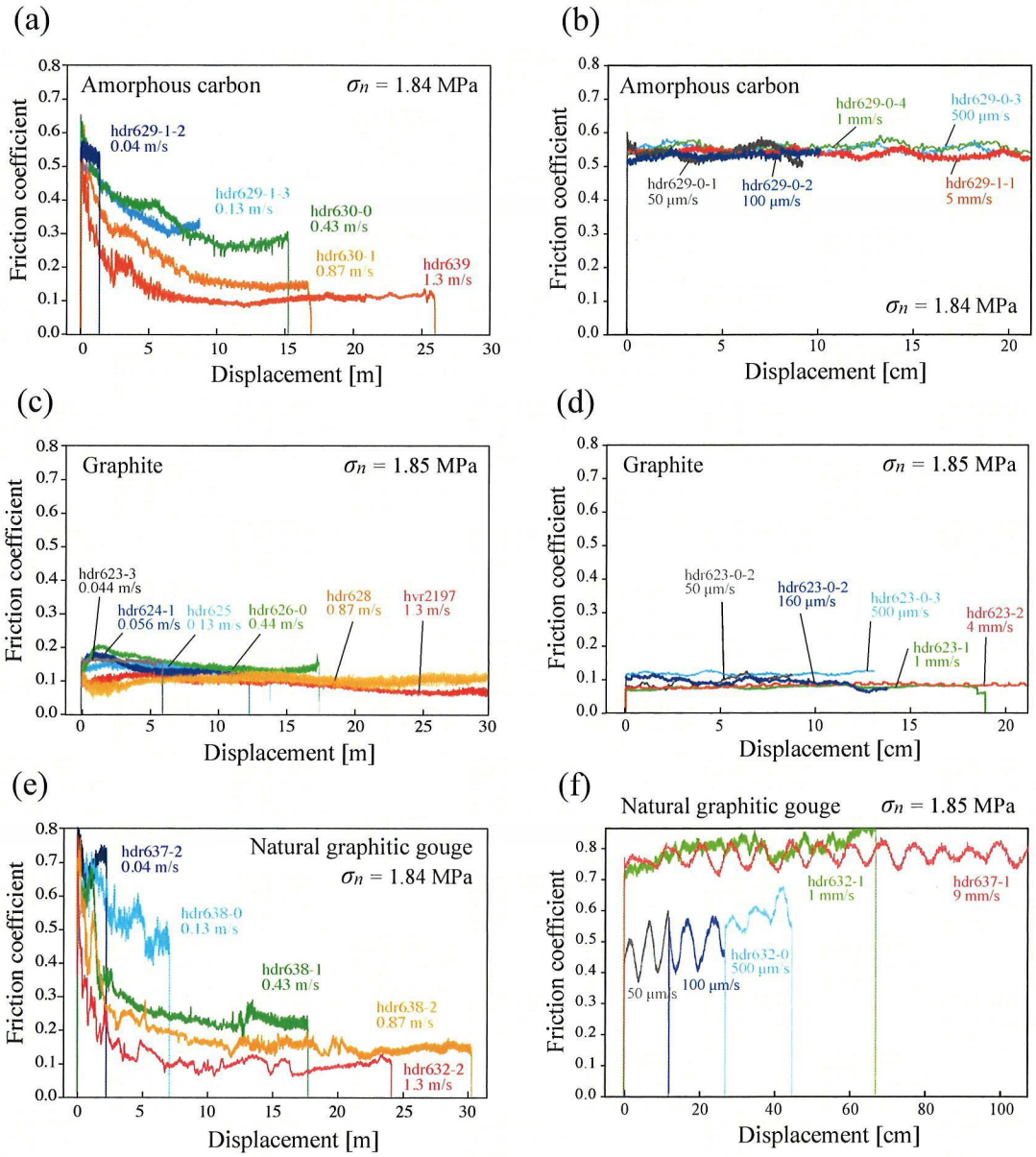

Fig. 3.7. Frictional behaviors at various slip rates on amorphous carbon gouge (a, c) and graphite gouge (b, d) at a normal stress of ~1.8 MPa in a intermediate to high-velocity regime (slip rate of 0.04 to 1.3 m/s) (a, b) and a low to intermediate-velocity regime (slip rate of 50 µm/s to 5 mm/s) (c, d).

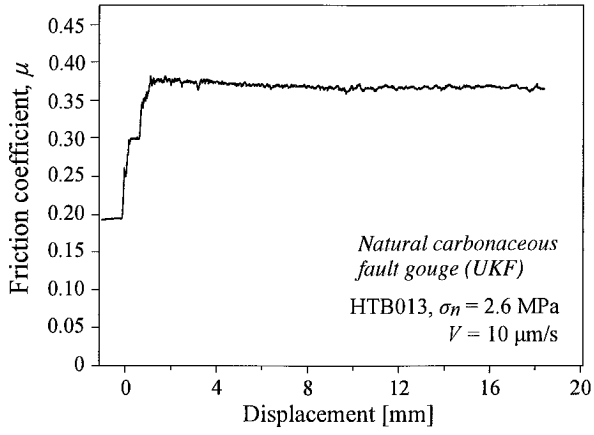

Fig. 3.8. Frictional behavior of natural carbonaceous fault gouge from the Ushikubi fault from biaxial friction experiment.

groups. At the high velocity range from 0.04 to 1.3 m/s, peak friction coefficient is about 0.7-0.8 at all slip rates, but steady-state friction coefficient decreases from 0.7 to 0.1 as the slip rate increases. At the intermediate velocities from 1 to 9 mm/s, friction remains about the same high value (0.75-0.8) throughout the tests. In contrast to the high, constant friction at the intermediate velocities, friction coefficient at low slip rates (50-500 μm/s) shows low, constant friction around 0.4 -0.5 in μ_{ss}.

Plots for frictional coefficients at all slip rates (Figure 3.11) clearly indicate that slip-weakening of amorphous carbon gouge begins to occur at slip rate of around 10^{-2} m/s and that its steady-state friction reduces to the same level (0.1) as that of graphite at slip rate of about 1 m/s. However, the peak friction μ_p did not exhibit velocity weakening, remaining at 0.58 ± 0.08 throughout the velocity range from centimeters to meters per second (open circles in Figure 6). Graphite gouge had a very low friction coefficient ($\mu < 0.2$) over a range of more than five orders of magnitude in slip rate (filled squares in Figure 3.8). Natural graphitic fault gouge from the Ushikubi fault indicates that the relatively low friction at low slip-rates of around 10^{-5}–10^{-4} m/s, velocity-strengthening begins to occur at intermediate slip-rates of around 10^{-3}–10^{-2} m/s and abrupt velocity-weakening begins to occur at slip rate of the middle of 10^{-2} m/s.

3-3-4. Velocity step tests of pure graphite

The results from velocity step tests of pure graphite gouge are shown in Figure 3.9. These results indicate that the negative response in a-b with positive abrupt change in slip rate, that is, strength reduction with increasing slip rate. Thus, graphite is characterized by slight velocity weakening behavior – strength reduces with increasing velocity – over the range of velocities measured in this experiments.

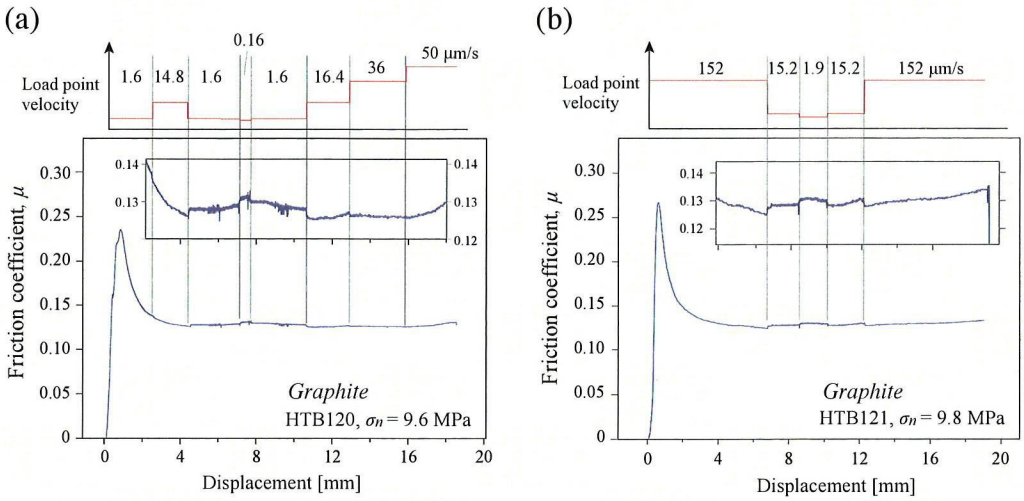

Fig. 3.9. Frictional behaviors of pure graphite gouge from biaxial friction experiments. Step changes in velocity were done in the range of (a) 0.16 ~ 50 μm/s and (b) 1.9 ~ 152 μm/s.

3-4. Interpretation and Discussion

3-3-2. Frictional properties of "amorphous" carbon

High-velocity friction experiments have demonstrated dramatic weakening of faults without frictional melting at slip rates greater than the order of 10 mm/s (e.g., Di Toro et al., 2004; Han et al., 2007a; Hirose & Bystricky, 2007; Mizoguchi et al., 2009). Surprisingly, the overall behavior of amorphous carbon is quite similar to those behaviors; i.e., fairly high friction at low to intermediate slip rates, but dramatic weakening at high slip rates. Amorphous materials have received attention since they forms during frictional sliding (Yund et al., 1990) and silica gel, a form of amorphous materials, is proposed to cause such weakening (Goldsby and Tullis, 2002; Di Toro et al., 2004). Previous experiments are inconclusive in this regard since amorphous materials form during frictional slip and may not be controlling the entire behavior. We did use amorphous carbon as the starting material, and given that the host-rock dolerite is stronger, we believe that the amorphous carbon is likely to control the overall behavior. Amorphous solid materials are defined by lack of long-range order characteristic of a crystal. Therefore, crystalline structures are not acceptable for weakness of this "disordered" material. According to the thin-film lubrication theory of nanotribology, friction of amorphous materials is high due to the molecular

interdigitations and entanglements (jamming of molecule chains) occurring between the two surfaces (Bhushan et al. 1995). But once sliding velocity increase, it is considered that the entangled molecule at the interface undergo "shear-induced ordering" (distangle and allingment), and in consequence friction drops significantly. Although I don't have enough data to extend this theory to the frictional behaviors of amorphous carbon yet, amorphous materials may generally cause such velocity weakening behaviors. Friction experiments using a variety of amorphous materials from rocks are needed to resolve this important issue.

3-3-2. Weakness and frictional instability of graphite

Friction of graphite gouge displayed very low friction coefficient (≈ 0.1) throughout the range of our velocity conditions (0.16 μm/s to 1.3 m/s). Additionally, slight velocity weakening behavior is observed over the range 0.16 to 152 μm/s. These frictional properties such as low frictional resistance and frictional instability may be related to the generation of microearthquakes. It is said that the presence of vapors, such as water, is required for graphite to lubricate; in highly vacuum or dry environments, the friction of graphite are high. However, it is uncommon for the fault, since fault zone may act as a conduit of fluids, and water fluids are certainly present along the grain boundaries, microshear zones and cracks in not only fault zones but also host rock. Take into account of thermal and chemical stability of graphite and low friction coefficient even at the high-normal stresses (Figure 3.10), graphite may form a weak fault even at the depths.

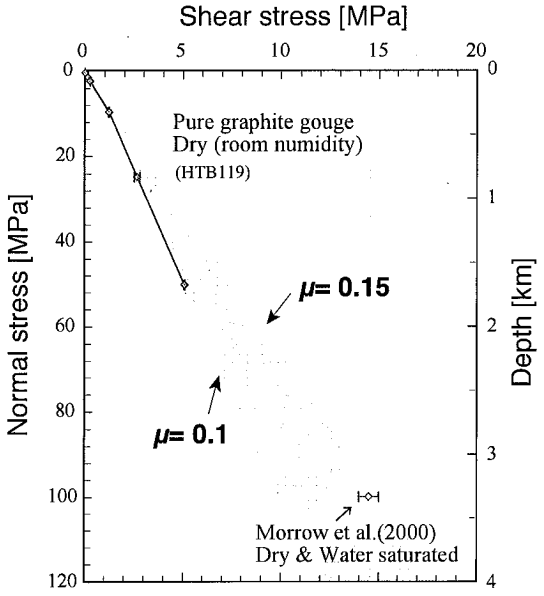

Fig. 3.10. Steady-state shear stress plotted against normal stress for pure graphite gouge. Results from biaxial (HTB119, this study) and triaxial experiments (Morrow et al., 2000) are plotted between 0.1 to 0.15 in friction coefficient.

3-3-2. Comparison between synthetic carbonaceous materials and natural carbonaceous fault gouge

Natural graphitic fault gouge from the Ushikubi fault indicates that the relatively low friction at low slip-rates, velocity-strengthening behavior at intermediate slip-rates and abrupt velocity-weakening behavior at high slip-rates. These behaviors are different from both amorphous carbon and graphite. This topic will discuss in Chapter 5 and 6, since frictional property of multimineralic natural fault gouge cannot compare directly with that of monomineralic amorphous carbon or graphite.

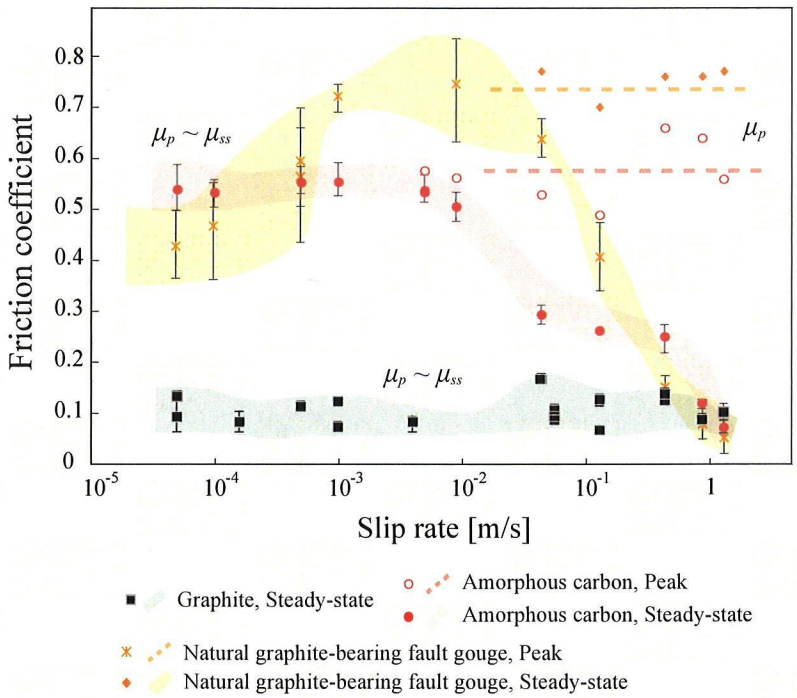

Fig. 3.11. Peak and steady-state friction plotted against slip rate for amorphous carbon (open and solid circles) , graphite gouge (squares) and natural graphite-bearing fault gouge from the Ushikubi fault.

3-5. Conclusions

1. For amorphous carbon gouge sheared at 1.3 m/s, the friction coefficient rapidly increased to ~0.54 at the initiation of slip, then decreased exponentially with displacement toward a steady-state friction coefficient of ~0.15. On the other hand, for slip rates from 50 μm/s to 5 mm/s, friction coefficients exhibited nearly constant values

of 0.54 ± 0.04. These frictional behaviors of amorphous carbon are concluded to high friction at low- to intermediate-slip rates and marked slip weakening at high-slip rates.

2. Gouge composed of amorphous carbon exhibits frictional behaviors quite similar to those of natural fault gouges (i.e. Nojima fault gouge; Mizoguchi et al., 2007), middle to high friction at low to intermediate-slip rates, but dramatic high-velocity weakening. Amorphous gouge was often found in the slip localization zones recovered after high-velocity experiments (e.g., Brantut et al., 2008), and hence, amorphous materials may generally cause such velocity weakening behaviors.

3. Graphite gouge sheared at 1.3 m/s showed a nearly constant friction coefficient of ~0.08 without visible slip weakening or strengthening throughout the experiment. Additionally, graphite gouge was very low throughout the range of our velocity conditions (50 μm/s to 1.3 m/s). Precise examination using biaxial friction apparatus reveals slight velocity weakening behavior over the range 0.16 to 152 μm/s. These frictional properties suggest that the possible agent of graphite for microearthquakes.

4. Frictional properties of quartz-graphite mixture gouge

4-1. Introduction

Graphite-bearing natural fault gouges are often composed of finely crushed quartzo-feldspathic fragments and highly crystallized graphite with minor accessory clay minerals. Although the graphite content varies depending on faults, most of the blackish fault gouge contains about 3-10 wt% of graphite (particles size of < 10 μm) in bulk fault gouge. Oohashi et al. (2011) revealed that graphite shows very low friction coefficient ($\mu < 0.2$) over a wide range of slip rates of 50 μm/s to 1.3 m/s. Consequently, the presence of graphite, even if its proportion is small, possibly reduces the fault strength efficiently.

Frictional experiments on mixtures with phyllosilicates (mainly for clay minerals) are conducted to examine its operation for weakening agent on frictional strength of gouge. Mixture of kaolinite and illite; which is often found from fault gouge and quartz shows almost linear, monotonic relationship with increasing clay content (Crawford et al., 2008). On the other hand, montmorillonite-quartz mixtures represent almost linear trend (Logan and Rauenzahn, 1987; Brown et al., 2003 and Takahashi et al., 2007) or slow exponential decay trend above about 20 % of clay content (Tembe et al, 2010) depends on displacement. Moore and Rymer (2007) speculate that talc, which is found in creeping section of the San Andreas fault, cause the reduction of fault strength. Latest laboratory experiments on talc-quartz mixture gouge by Moore and Lockner (2010) revealed that its initial linear trend to 15 % and following high rates of weakening between 15 to 40–50 % that is quite similar to montmorillonite-quartz mixtures by Tembe et al. (2010). These experiments are conducted with limited shear strain ($\gamma <$ a few dozen) depending on experimental geometry of biaxial or triaxial testing apparatus in spite of significance of applied shear strain and fabric development on weakening has been pointed out (e.g. Collettini et al., 2009).

The effect of graphite content on fault strength and its contribution on fault weakening have not been investigated systematically up to now, even though graphite was often found in the fault zones, especially developed in metamorphic belts, sedimentary basins and accretionary complexes. Meanwhile, quartz is major

rock-forming mineral and typically found from fault gouge or cataclasite not only from graphite bearing faults but also all over the continental faults. Furthermore, quartz can be regard as an analog mineral since its friction is comparable to other rock-forming minerals (Byerlee, 1978, Wibberley et al., 2008). In this study, I thus performed friction experiments of graphite-quartz bimineralic gouges in different graphite fractions and slip rates with large displacement, in order to understand how frictional behavior changes with increases in graphite content and to examine the possibility that the graphite makes fault slippery in natural graphite bearing faults. Our experiments may give insight into potential of graphite for weakening agent on natural faults and mechanisms for making statically weak faults.

4-2. Experimental procedures

I used three types of starting materials for simulated fault gouge: pure quartz powder (angular shape and grain size <200 μm), pure graphite powder (platy shape and grain size <45 μm; Figure 1a, frictional datum are already reported in Oohashi et al., 2011) for end members and mixtures of quartz and graphite powder. The quartz and graphite powders were bought from Wako Pure Chemical Industries, Ltd (product No. 199-00625 and 072-03845, respectively). I prepared six mixtures with specific graphite content: 5, 7.5, 10, 15, 25, 50 wt% (corresponds to 5.8, 8.7, 11.6, 17.2, 28.2, 54.1 vol%, respectively), in order to elucidate the effect of graphite quantitatively on mechanical behavior of faults. Friction experiments were performed using a rotary-shear, low- to high-velocity friction apparatus (HVR; Figure 3.2a) at Kochi/JAMSTEC (Shimamoto and Tsutsumi, 1994; Hirose and Shimamoto, 2005). The experiments were conducted at normal stresses (σ_n) of 1.0 to 2.0 MPa and equivalent slip rates (V_e) of 50 μm/s to 1.3 m/s with displacements of 0.39 to 94 m. Because the slip rate increases from the center to the periphery of the cylindrical specimens, I used the equivalent slip rate, V_e, defined such that $\tau V_e S$ gives the rate of total frictional work on a fault with area S, assuming a constant shear stress τ over the fault surface (Shimamoto and Tsutsumi, 1994). Hereafter, for convenience, I refer to "equivalent slip rate" as simply "slip rate".

Simulated fault gouges were placed between two cylinders of dolerite host rock with 25.0 mm in diameter whose end surfaces were ground with SiC 80# powder (see Figure 3.2b). A Teflon sleeve of 24.9 mm in inner diameter was attached around the simulated fault zone to prevent gouge leakage. To correct for the effect of friction

between the Teflon sleeve and the cylinders, I measured the shear traction in experiments without gouge, then subtracted the traction from the measured raw data of gouge experiments (see details in Appendix A). Thus, the frictional datum reported in this paper are already removed the effect of the friction from the Teflon sleeve. All starting materials and host rock cylinders were dried in an oven at 80 °C for at least 48 hours before experiments. All experiments were done with nearly constant gouge thickens of 1.2 mm and under room temperature and humidity.

Two series of experiments were carried out at a constant normal stress with slip displacement of more than several dozens of centimeters; (1) test with various slip rates from 0.15 to 56 mm/s during a single run and (2) constant slip rate test at 0.13, 0.44 and 1.3 m/s (Table 2). Some experiments were stopped before the steady state reached, and recovered the specimen in order to understand the microstructural evolution with displacement (hvr2273 and 2274).

4-3. Mechanical behaviors

4-3-1. Mechanical behaviors of pure quartz and graphite gouges

Figure 4.1 shows frictional behaviors of pure quartz and graphite gouges at representative slip rates of 150 μm/s, 56 mm/s and 1.3 m/s. Frictional behavior at low (150 μm/s) to intermediate (56 mm/s) slip rates of quartz gouge represents a nearly constant friction coefficient of 0.6~0.65 throughout the experiment without visible slip weakening or strengthening. On the other hand, at high slip rate (1.3 m/s) friction coefficient increases rapidly to an initial peak friction coefficient μ_p of 0.82 at the beginning of the run and

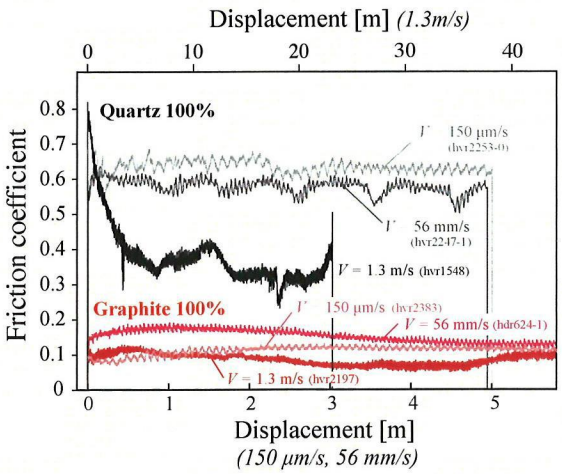

Fig. 4.1. Friction coefficient plotted against fault displacement of pure quartz and graphite gouges at slow (V = 150 μm/s), intermediate (V = 56 mm/s) and high (V = 1.3 m/s) slip-rate and σ_n = 1.9 MPa.

Table 2
Summary of experimental data reported in Chapter 4.

Run No.	Material	Graphite [wt%]	Velocity [m/s]	Displace -ment [m]	Normal stress [MPa]	Initial friction [μ]	Peak friction [μ]	Steady state friction		
								μ	Error+	Error–
hvr2246-0	Quartz	0	0.00015	0.45	2.0	0.59	0.59	0.63	0.02	0.04
hvr2246-1	Quartz	0	0.00044	0.39	2.0	0.7	0.71	0.65	0.02	0.03
hvr2246-2	Quartz	0	0.0013	0.89	2.0	0.74	0.74	0.68	0.02	0.03
hvr2246-3	Quartz	0	0.0044	5.60	2.0	0.73	0.73	0.64	0.04	0.05
hvr2247-0	Quartz	0	0.021	3.79	2.0	0.75	0.81	0.58	0.03	0.03
hvr2247-1	Quartz	0	0.056	4.93	2.0	0.69	0.69	0.61	0.03	0.04
hvr2247-2	Quartz	0	0.13	12.57	2.0	0.71	0.71		[b]	
hvr1548	Quartz	0	1.3	23.09	1.0	0.82	0.82	0.33	–	–
hvr2275	Quartz	0	0.13	10.22	2.0	0.63	0.74	0.615	0.05	0.05
hvr2276	Quartz	0	0.436	12.97	2.0	0.7	0.75	0.415	0.02	0.01
hvr2253-0	Quartz	0	0.00015	4.97	2.0	0.65	0.74	0.62	0.03	0.02
hvr2249-0	G-Q Mixture 5%	5	0.00015	1.63	2.0	0.72	0.71	0.62	0.01	0.01
hvr2249-1	G-Q Mixture 5%	5	0.00044	0.97	2.0	0.68	0.68	0.59	0.006	0.01
hvr2249-2	G-Q Mixture 5%	5	0.0013	0.62	2.0	0.65	0.65	0.56	0.016	0.01
hvr2249-3	G-Q Mixture 5%	5	0.0044	4.97	2.0	0.64	0.64	0.56	0.02	0.03
hvr2249-4	G-Q Mixture 5%	5	0.021	3.86	2.0	0.57	0.57	0.52	0.01	0.01
hvr2249-5	G-Q Mixture 5%	5	0.056	7.66	2.0	0.52	0.53	0.44	0.02	0.03
hvr2249-6	G-Q Mixture 5%	5	0.13	21.90	2.0	0.52	0.56	0.325	0.02	0.02
hvr2269	G-Q Mixture 5%	5	0.00015	2.91	2.0	0.66	0.76	0.56	0.02	0.02
hvr2282	G-Q Mixture 5%	5	0.00015	5.40	2.0		[a]	0.61	–	–
hvr2254-0	G-Q Mixture 7.5%	7.5	0.00015	6.11	2.0	0.62	0.67	0.5	0.03	0.03
hvr2254-1	G-Q Mixture 7.5%	7.5	0.00044	2.87	2.0	0.54	0.54	0.48	0.04	0.03
hvr2254-2	G-Q Mixture 7.5%	7.5	0.0013	6.07	2.0	0.51	[a]	0.55	0.02	0.02
hvr2254-3	G-Q Mixture 7.5%	7.5	0.0044	1.55	2.0	0.6	0.6	0.51	0.02	0.02
hvr2254-4	G-Q Mixture 7.5%	7.5	0.021	7.11	2.0	0.58	0.59	0.43	0.03	0.03
hvr2254-5	G-Q Mixture 7.5%	7.5	0.056	6.98	2.0	0.68	0.68	0.42	0.01	0.02
hvr2254-6	G-Q Mixture 7.5%	7.5	0.13	11.93	2.0	0.57	0.57	0.405	0.01	0.02
hvr2254-7	G-Q Mixture 7.5%	7.5	0.436	16.02	2.0	0.59			[b]	
hvr2270	G-Q Mixture 7.5%	7.5	0.00015	2.51	2.0	0.68	0.72	0.47	0.01	0.01
hvr2277	G-Q Mixture 7.5%	7.5	0.13	16.32	2.0	0.66	0.79	0.435	0.02	0.02
hvr2278	G-Q Mixture 7.5%	7.5	0.436	35.43	2.0	0.65	0.75	0.395	0.04	0.04
hvr2250-0	G-Q Mixture 10%	10	0.00015	1.52	2.0	0.64	0.65	0.51	0.02	0.02
hvr2250-1	G-Q Mixture 10%	10	0.00044	0.43	2.0	0.57	0.57	0.5	0.02	0.02
hvr2250-2	G-Q Mixture 10%	10	0.0013	1.02	2.0	0.57	0.57	0.5	0.01	0.01
hvr2250-3	G-Q Mixture 10%	10	0.0044	3.67	2.0	0.57	0.57	0.4	0.02	0.01
hvr2250-4	G-Q Mixture 10%	10	0.021	7.20	2.0	0.47	0.49	0.32	0.01	0.01
hvr2250-5	G-Q Mixture 10%	10	0.056	5.44	2.0	0.4	0.4	0.31	0.03	0.03
hvr2250-7	G-Q Mixture 10%	10	0.13	15.23	2.0	0.44	0.48	0.365	0.01	0.01
hvr2250-8	G-Q Mixture 10%	10	0.436	7.08	2.0	0.44	0.45	0.33	0.02	0.02
hvr1562	G-Q Mixture 10%	10	1.3	34.81	1.0	0.76	0.76	0.195	0.01	0.01
hvr2272	G-Q Mixture 10%	10	0.00015	3.57	2.0	0.6	0.75	0.29	0.02	0.03
hvr2273	G-Q Mixture 10%	10	0.00015	0.62	2.0	0.59	0.67		[b]	
hvr2274	G-Q Mixture 10%	10	0.00015	1.73	2.0	0.61	0.64	0.48	0.03	0.03
hvr2279-1	G-Q Mixture 10%	10	0.0013	6.78	2.0	0.58	0.74	0.34	0.02	0.02
hvr2279-2	G-Q Mixture 10%	10	0.0044	5.37	2.0	0.41	0.41	0.33	0.03	0.03
hvr2298	G-Q Mixture 10%	10	0.00023	4.09	2.0	0.72	0.69	0.47	0.01	0.01
hvr2251-0	G-Q Mixture 15%	15	0.00015	4.32	2.0	0.61	0.68	0.25	0.02	0.01
hvr2251-1	G-Q Mixture 15%	15	0.00044	0.47	2.0	0.375	0.375	0.305	0.025	0.025
hvr2251-2	G-Q Mixture 15%	15	0.0013	0.62	2.0	0.4	0.4	0.33	0.02	0.02
hvr2251-3	G-Q Mixture 15%	15	0.0044	1.77	2.0	0.41	0.45	0.36	0.03	0.04
hvr2251-4	G-Q Mixture 15%	15	0.021	5.51	2.0	0.45	0.46	0.28	0.02	0.01
hvr2251-5	G-Q Mixture 15%	15	0.056	7.25	2.0	0.37	0.37	0.26	0.01	0.01
hvr2251-6	G-Q Mixture 15%	15	0.00015	27.48	2.0	0.46	0.41	0.24	0.01	0.01
hvr2283	G-Q Mixture 15%	15	0.436	19.55	2.0	0.67	0.72	0.1605	0.01	0.01
hvr2281	G-Q Mixture 15%	15	0.13	32.91	2.0	0.76	0.37	0.31	0.007	0.01
hvr2252-0	G-Q Mixture 25%	25	0.00015	12.17	2.0	0.59	0.59	0.3	0.02	0.02
hvr2252-1	G-Q Mixture 25%	25	0.00044	1.31	2.0	0.4	0.4	0.33	0.05	0.05
hvr2252-2	G-Q Mixture 25%	25	0.0013	0.81	2.0	0.41	0.41	0.32	0.05	0.05
hvr2252-3	G-Q Mixture 25%	25	0.0044	2.86	2.0	0.41	0.42	0.24	0.04	0.05
hvr2252-4	G-Q Mixture 25%	25	0.021	4.57	2.0	0.27	0.27	0.17	0.04	0.04
hvr2252-5	G-Q Mixture 25%	25	0.056	8.65	2.0	0.24	0.24	0.16	0.02	0.03
hvr2252-6	G-Q Mixture 25%	25	0.056	7.65	2.0	0.27	0.27	0.15	0.03	0.02
hvr2252-7	G-Q Mixture 25%	25	0.13	17.46	2.0	0.27	0.28	0.125	0.02	0.03
hvr2252-8	G-Q Mixture 25%	25	0.436	13.04	2.0	0.28	0.28	0.14	0.03	0.02
hvr2271	G-Q Mixture 25%	25	0.00015	1.55	2.0	0.57	0.62	0.32	0.02	0.01
hvr2280-1	G-Q Mixture 25%	25	0.0013	1.96	2.0	0.6	0.6	0.2	0.01	0.01
hvr2280-2	G-Q Mixture 25%	25	0.0044	1.91	2.0	0.277	0.277	0.207	0.009	0.007
hvr2248-0	G-Q Mixture 50%	50	0.00015	0.92	2.0	0.23	0.23	0.08	0.01	0.01
hvr2248-1	G-Q Mixture 50%	50	0.00044	0.67	2.0	0.14	0.14	0.07	0.018	0.016
hvr2248-2	G-Q Mixture 50%	50	0.0013	0.63	2.0	0.17	0.17	0.1	0.01	0.02
hvr2248-3	G-Q Mixture 50%	50	0.0044	3.43	2.0	0.15	0.15	0.07	0.01	0.01
hvr2248-4	G-Q Mixture 50%	50	0.021	5.13	2.0	0.16	0.16	0.09	0.01	0.01
hvr2248-5	G-Q Mixture 50%	50	0.056	5.42	2.0	0.17	0.18	0.105	0.015	0.015
hvr2248-6	G-Q Mixture 50%	50	0.13	11.15	2.0	0.16	0.17	0.115	0.01	0.01
hvr2248-7	G-Q Mixture 50%	50	0.436	33.91	2.0	0.18	0.19	0.08	0	0.01
hvr2248-8	G-Q Mixture 50%	50	0.872	94.58	2.0	0.17	0.17	0.09	0.01	0.01
hvr1563	G-Q Mixture 50%	50	1.3	39.64	1.0	0.31	0.31	0.11	–	–
hvr2383	Graphite	100	0.00015	11.45	2.0	0.1	0.13	0.12	0.01	0.01

[a] No peak friction was observed
[b] Experiment was stopped or failed during weakening

then decreased exponentially with displacement toward a steady-state friction coefficient μ_{ss} of 0.33. In contrast, friction coefficient of graphite gouge is significantly low (about 0.1) throughout the experiments at any slip rates.

4-3-2. Mechanical behaviors of graphite-quartz mixture gouges

Figure 4.2 shows frictional behaviors of graphite-quartz mixture gouges at three representative slip rates. At the experiments at a slip rate of 150 μm/s, slip-weakening behaviors are observed for all gouges; the fault strength starts to drop within the displacement of several dozens of centimeters and reaches to the steady state in few meters displacement (Figure 4.2a). The steady-state friction coefficient lowers with the increase of graphite fraction from 0.58 to 0.3 at the graphite content of 5.8 and 28 vol%, respectively, whereas the initial peak friction coefficient keeps almost constant (μ_p of 0.6-0.7) in spite of the increase in graphite content. On the other hand, an experiment on 54 vol% of graphite shows low initial friction coefficient from just after the onset of experiment (μ_p of 0.14), and steady-state friction becomes equivalent to

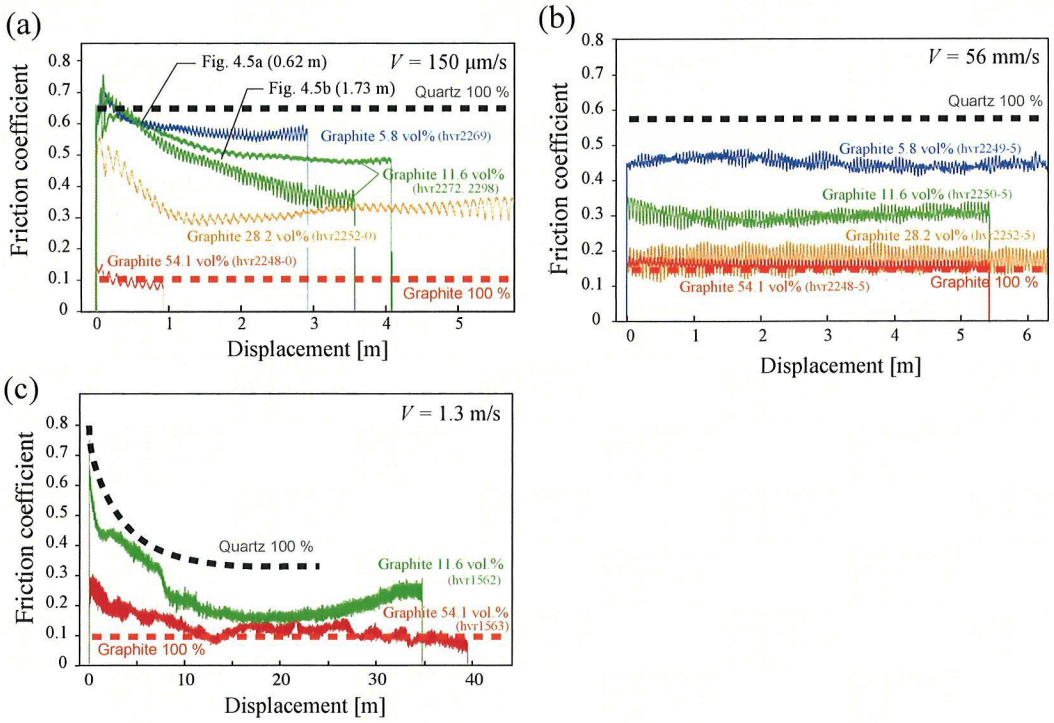

Fig. 4.2. Friction coefficient plotted against fault displacement of graphite-quartz mixture gouges with various graphite content at (a) slow (V = 150 μm/s), (b) intermediate (V = 56 mm/s) and (c) high (V = 1.3 m/s) slip-rate and σ_n = 2.0 MPa. Friction coefficient of pure quartz and graphite gouges at each slip rates are also illustrated in dotted lines.

pure graphite within the displacement of 1 m. Notable point is that only 5.8~11 vol% addition of graphite can cause 20~50 % reduction in friction coefficient against the pure quartz gouge. At slip rates of 56 mm/s and 1.3 m/s (Figure 3b and c), the steady-state friction coefficient lowers with an increase of graphite fraction in the same manner as the low slip rate although no slip-weakening behavior is observed at 56 mm/s. The reason of no appearance of slip weakening at 56 mm/s will be discuss in the 4-5-2.

4-3-3. Velocity dependence of friction

Steady-state friction coefficient of pure graphite, pure quartz and mixtures with different slip rates are summarized in Figure 4.3. The friction coefficient of pure quartz gouge shows nearly constant value of μ_{ss} = 0.6-0.7 at slip rates from 10^{-4} to 10^{-1} m/s (opened diamonds in Figure 4.3), and it lowers dramatically to less than 0.4 in μ_{ss} at > 0.43 m/s. On the other hand, graphite gouge had a very low friction coefficient (μ_{ss} < 0.2) over a range of more than five orders of magnitude in slip rate (filled diamonds in Figure 4.3). On the mixture gouges, the steady-state friction coefficient systematically reduces with increasing of graphite fraction toward the friction of graphite at slip rates from 10^{-4} to 10^{-1} m/s. However at the high slip rate of 10^{0} m/s the steady-state friction coefficient tends to become almost same value of <0.2 irrespective of graphite fraction.

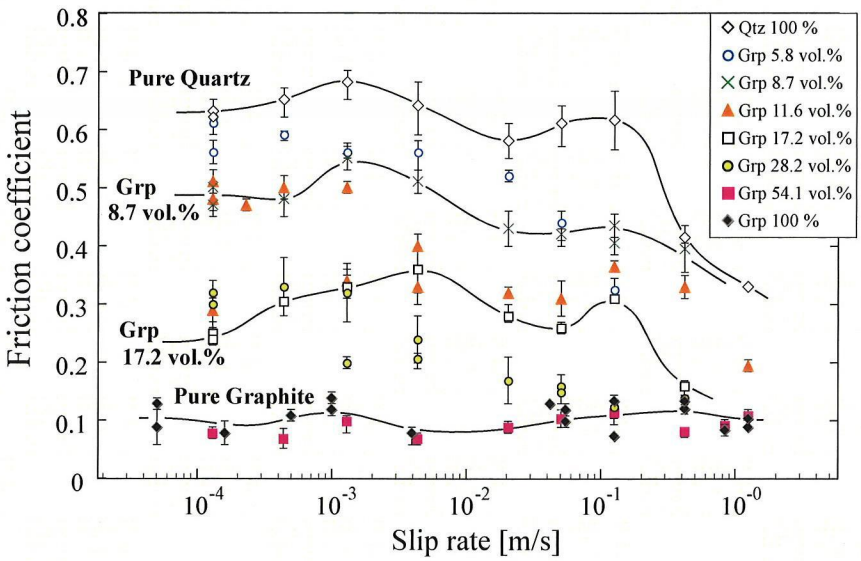

Fig. 4.3. Steady-state friction coefficient plotted against slip rate of pure quartz gouge, pure graphite gouge and various fractions of graphite-quartz mixture gouge.

4-4. Fault zone microstructures

4-4-1. Textural differences with graphite fraction

To understand the observed fault weakening with increasing graphite fraction, I conducted microstructural observation on a polished section (location is shown in Figure 1c) using a field emission scanning electron microscope (FE-SEM) with an energy dispersive X-ray spectroscopy (EDS). Figure 4.4a to f shows SEM images of fault zones prior to the shearing (c, e, g and i) and after the shearing (d, f ,h and i) of 5.8, 11.6 and 28 vol% graphite mixture, respectively. The fault zone textures prior to the shearing show almost homogeneous with slight fractures in quartz grains due to the sample preparation. The specimens from 5.8 and 11.6 vol% graphite mixtures (Figure 4.4c and g) show grain-supported texture. Each quartz grain (bright color) maintains angular shape and contact each other at the edge of them. Graphite flakes (dark stripes) are surrounded by the quartz grains. On the other hand, the specimen of 28 vol% graphite mixture (Figure 4.4i) shows matrix-supported texture, and each quartz grains are surrounded by graphite flakes or thin sheet of graphite.

Figure 5 d, f, h and j correspond to the fault zone textures which are attained to the steady state. Deformed textures from 5.8, 11.6, and 28 vol% graphite mixture are characterized by presence of a highly deformed narrow zone (slip-localized zone; SLZ, approximately 300–400 μm in thickness) at the one of the rock-gouge boundary. The other part of the gouge zone maintains original, undeformed texture. The slip-localized zone from 5.8 and 11.6 vol% mixtures are characterized by "grain-matrix intermingling" texture which is composed by the finely comminuted quartz and graphite grains <10 μm in diameter (Figure 5i). Whereas the comminuted quartz grains down to submicron in diameter, graphite breaks into much finer particle and surrounds the quartz grains. This is also supported by EDS element mapping (Figure 4.4n), matrix of slip-localized zone is composed of both quartz (Si) and graphite (C). Within the center of the slip-localized zone, a throughgoing distinct slip surface (SS; few tens of micron in width) runs through the zones. On the 5.8 vol% mixture gouge, the slip surface is bounded by the fine gouge zones with slight difference of matrix/fragment ratio and no interconnected graphite is recognized along the slip surface (Figure 4.4k). On the contrary, 11.6 vol% mixture makes a thin, interconnected graphite matrix developed along the slip surface (Figure 4.4l). Except for the slip surface, I can hardly distinguish the foliation which is

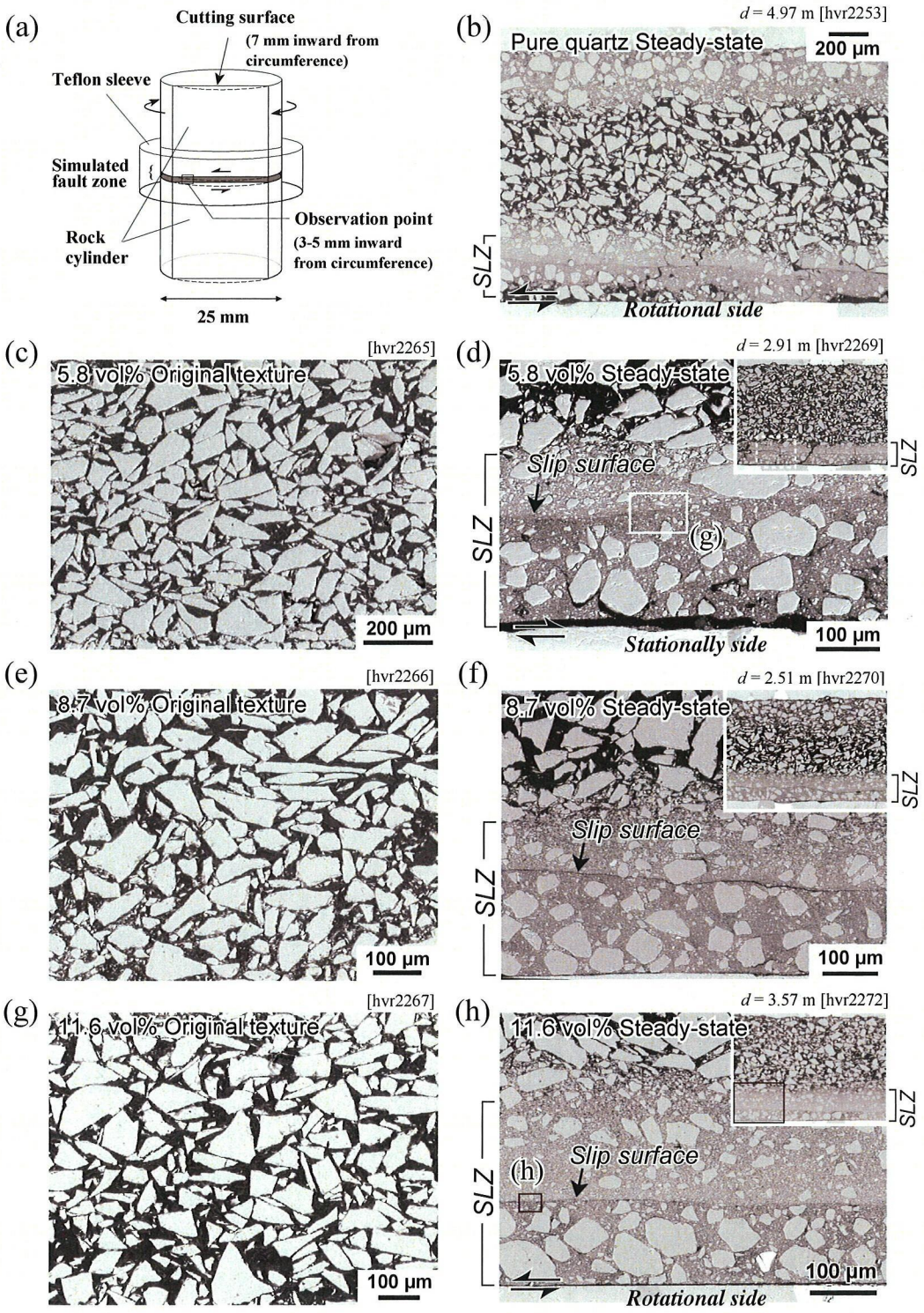

Fig. 4.4. SEM backscattered electron images of simulated gouge zone prior and after the shearing. (a) Thin sections were made along the illustrated longitudinal section.Observations were done at illustrated point. (b) Steady-state textures of pure quartz gouge sheared at V = 150 μm/s and σ_n = 2.0 MPa. (c, e, g, i) Original gouge textures of 5.8, 8.7, 11.6 and 28 vol% graphite-quartz mixtures respectively. (d, f, h, j) Steady-state textures of 5.8, 8.7, 11.6 and 28 vol% graphite-quartz mixtures sheared at V = 150 μm/s and σ_n = 2.0 MPa, respectively. An inset shows entire section of the simulated gouge. (k, l) The magnified images along the slip surface of 5.8 (k) and 11.6 vol% (l) respectively. (m) The magnified image of matrix of the slip-localized zone (11.6 vol%). A magnified area is illustrated in Fig. 5.5c. (n) EDS element mapping of carbon (C) and silica (Si) in boxed area of Fig. 5.5c. Upper dotted line denote the slip surface and lower indicate the boundary between rock cylinder and gouge zone. SLZ, slip-localized zone; SS, slip surface.

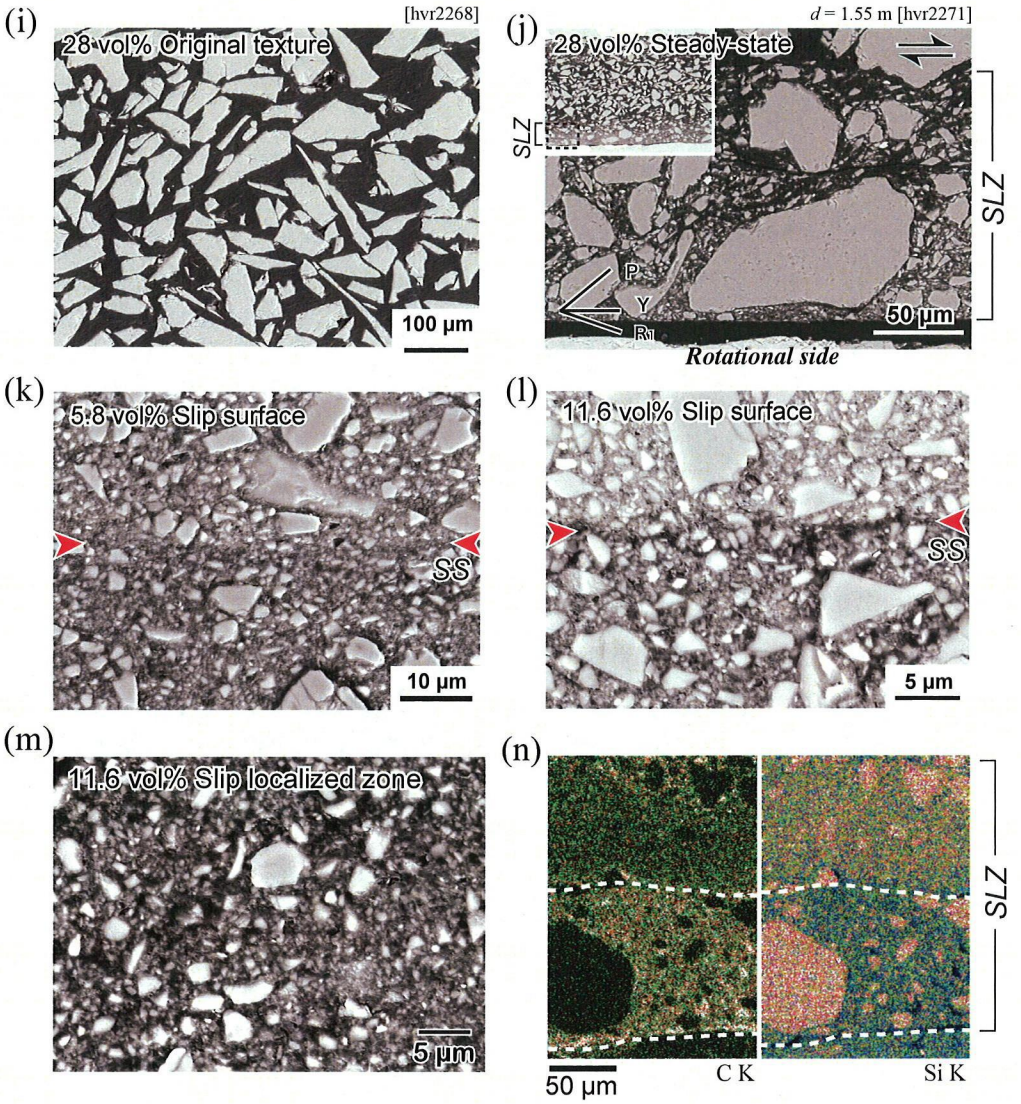

Fig. 4.4. (continued).

formed by connectivity of graphite within the slip-localized zones, and matrix shows almost random in fabric (Figure 4.4m).

On the 28 vol% graphite mixture, the comminution of quartz grains are less visible in the slip-localized zone (Figure 4.4j) as compared to the 5.8 and 11.6 vol%. This slip-localized zone is characterized by the development of composite planar fabric with Y, R_1 shear and P foliation. The P foliation is composed by the arrangement of major axis of quartz grains and the connectivity of graphite flakes, and forms "graphite-matrix supported" texture in the slip-localized zone. Such composite planar

fabric has not recognized from 5.8 and 11.6 vol% mixture gouges.

4-4-2. Microstructural evolution during slip weakening

To investigate the relationship between textural development and slip weakening of graphite-quartz mixture gouge, I conducted microstructural observation of the fault zone of 11.6 vol% mixture gouge at early, late and steady-state stages of the slip weakening (Figure 4.5). The initial texture of the fault zone is homogeneous, grain-supported texture (Figure 4.4g). The grain size reduction of quartz starts at displacement of 0.62 m (the early stage of slip weakening), forming an incipient slip-localized zone at the one or both sides of the boundary between rock cylinder and gouge zone (Figure 4.5a). The visible slip-localized zone that composed of further crushed quartz grains is developed at the displacement of 1.73 m (the middle to late stage of slip weakening) (Figure 4.5b). At this stage, discontinuous slip surface which is disconnected by coarse fragments of quartz appears within the center of the slip localized zone. This slip surface connects and forms a single continuous slip surface at the steady-state stage (Figure 4.5c). The slip-localized zone away from the slip surface is characterized by "grain-matrix intermingling" texture; the fine quartz grains seem to surround the graphite (Figure 4.4m). Such a texture is typically observed in the slip-localized zone prior to the steady-state stage. In contrast, the continuous slip surface consists of the connected graphite-matrix (Figure 4.4l) is only recognized from steady-state stage.

4-5. Interpretation and discussion

4-5-1. Correlation between microstructure and strength reduction

The steady-state friction decreases with increasing graphite fraction irrespective of slip rate (Figure 4.2 and 4.3). This trend can be expressed by sigmoid fitting curves with the following empirical equation (Figure 4.6):

$$\mu_{ss} = \mu_{100} + (\mu_0 - \mu_{100})/(1+(x/C_w)^S) \qquad (9)$$

where μ_{100} is steady-state friction of pure graphite, μ_0 is steady-state friction of pure quartz, x is a graphite fraction, C_w is a critical weakening fraction and S is a slope parameter. Thus, the frictional strength of graphite-quartz mixture gouge drop with

graphite content according to the power-law relations. The sigmoid fitting equations in Figure 4.6 indicate that 9.8 to 12.4 vol% of graphite addition reduces friction coefficient of $(\mu_0 - \mu_{100})/2$. Furthermore, more than 20 vol% of graphite addition makes the friction strength of mixture gouge nearly equivalent to that of the pure graphite at all slip rates.

Based on the textural observation, there is striking difference between 5.8, 11.6 and 28 vol% mixture gouges. On the 5.8 vol% of mixture gouge at the steady-state stage, the slip localized zone is composed of randomly oriented quartz-graphite mixture without visible foliation except for slip surface. Additionally, there is no interconnection of graphite-matrix along the surface (Figure 4.4d and k). On the other hand, the texture of 11.6 vol% mixture is characterized by textures of random fabric in slip-localized zone and interconnected graphite-matrix along the slip surface. In contrast to 5.8 and 11.6 vol%, the slip localized zone of 28 vol% mixture shows development of composite planar fabric and connection of graphite layers parallel to the Y and P surface within the zone. Consequently, the slip-localized zone forms diffused graphite-matrix flow structure. The textural transition from localized slip without connected graphite to localized slip with interconnected graphite lubrication, and to graphite-matrix flow within the slip-localized zone, with increases of graphite fraction may leads to sufficient weakening.

4-5-2. Slip-weakening mechanisms at 0.15 mm/s

Friction-displacement trajectories of graphite-quartz mixture gouges clearly indicate slip-weakening behavior within the displacement of first few meters (Figure 4.2a), whereas the pure quartz and graphite gouge does not represent such behavior. According to the microstructural observation on snapshots of 11.6 vol% mixture gouge, textural development with increasing displacement was recognized (Figure 4.5a to c). Original fault zone texture is constructed by framework of quartz grains and this is why initial peak friction shows high value (μ_p of 0.6-0.7) equal to the pure quartz gouge. Early stage of slip weakening corresponds to the initiation of incipient slip localized zone and breakage of strength framework of quartz along the rock-gouge boundary. At the later stage of slip weakening, discrete slip-localized zone and the beginning of slip surface are created with progressive comminution, and displacement become more localized along the surface (Figure 4.5b). However, this slip surface is not thoroughgoing but intermitted by the surviving coarse quartz fragments within the

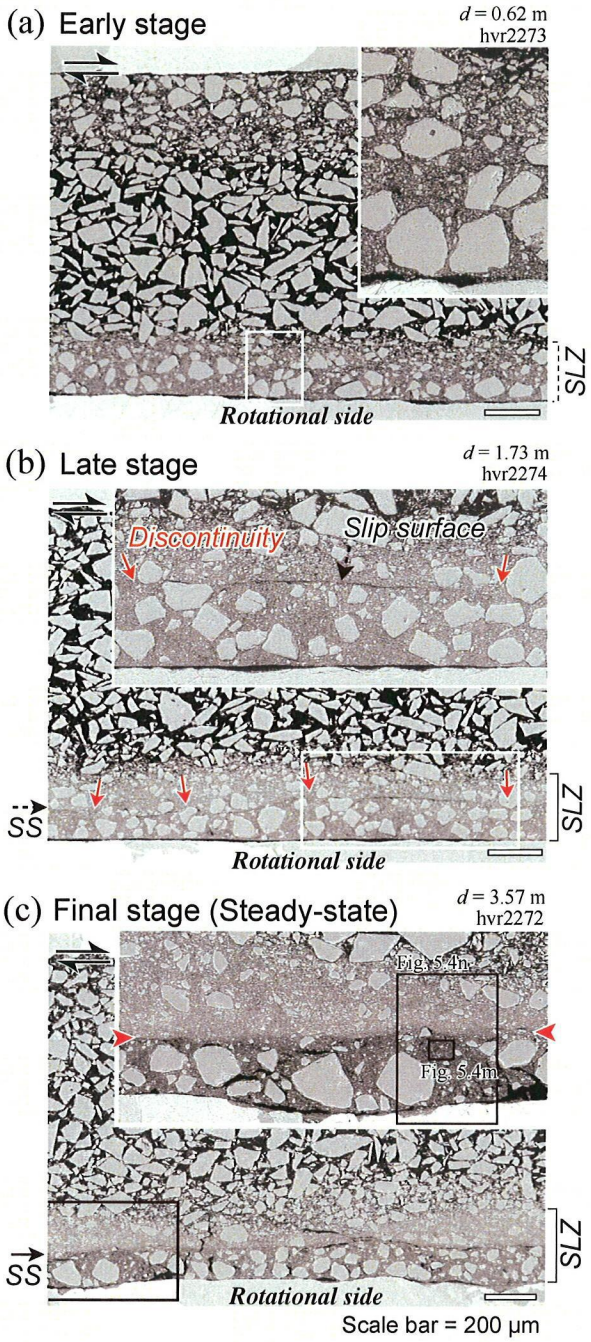

Fig. 4.5. SEM backscattered electron images of three different stages during the slip weakening sheared at V = 150 μm/s and σn = 2.0 MPa. (a) A snapshot of early stage of the slip weakening (hvr2273). The inset shows close-up view of the incipient slip-localized zone (boxed area). (b) The snapshot of middle to late stage of the slip weakening (hvr2274). The inset shows close-up view of the slip-localized zone and discontinuous slip surface (boxed area). Red allows show discontinued sections. (c) The texture of final stage of the slip weakening (hvr 2272). The inset shows close-up view of the slip-localized zone and throughgoing slip surface (boxed area). SLZ, slip-localized zone; SS, slip surface.

slip-localized zone. Therefore, quartz framework is not completely broke up at this stage, and friction coefficient shows still high as compared to the steady state. Finally, slip surface which is composed of interconnected matrix of graphite penetrates within the slip-localized zone thoroughly (Figure 4.4h and Figure 4.5c) and friction is completely released from strength framework of quartz. The textural development, that is, breakage of quartz framework due to the appearance of extremely comminuted slip-localized zone and penetration of throughgoing slip surface (± interconnected graphite-matrix) are essential mechanisms for slip weakening of < 28 vol% mixture gouges.

No visible slip-weakening behaviors are found from the experiments at intermediate slip rate (Figure 2b). These specimens slide sufficiently at lower slip rates, leading to the formation of the slip localization zone. Hence, the preexistence of these structures possibly eliminates the slip weakening behaviors.

4-5-3. Graphite as a weakening agent for faults

Effect of weak phyllosilicate minerals on gouge friction was examined based on the bimineralic friction experiments (e.g. Logan and Rauenzahn, 1987, Brown et al., 2003, Crawford et al., 2008, Moore and Lockner, 2010). Frictional experiments on montmorillonite (smectite) , illite and kaolinite with quartz powder shows almost linear dependency of friction on clay content, but 15–25 % of clay addition is not sufficient to reduce the fault strength (see Figure 4.6; Montmorillonite; Logan and Rauenzahn, 1987, Takahashi et al., 2007, Tembe et al., 2010; Illite; Brown et al., 2003, Tembe et al., 2010; Kaolinite; Crawford et al., 2008). Additionally, Moore and Lockner (2010) conducted talc-quartz bimineralic experiments and revealed its linear trend of decreasing from 0 to 15 % of talc and following higher rates of weakening from 15 % to 40–50 % (Figure 4.6). However, our experiments of graphite-quartz bimineralic gouge abruptly loses the strength around 10 vol%, and 20–30 vol% of addition may leads to the friction of graphite irrespective of slip-rate. This power-law dependency of frictional strength on graphite content distinctly differs from almost linear dependency of another phyllosilicate minerals, and is suggests that its effectiveness for weakening agents on faults.

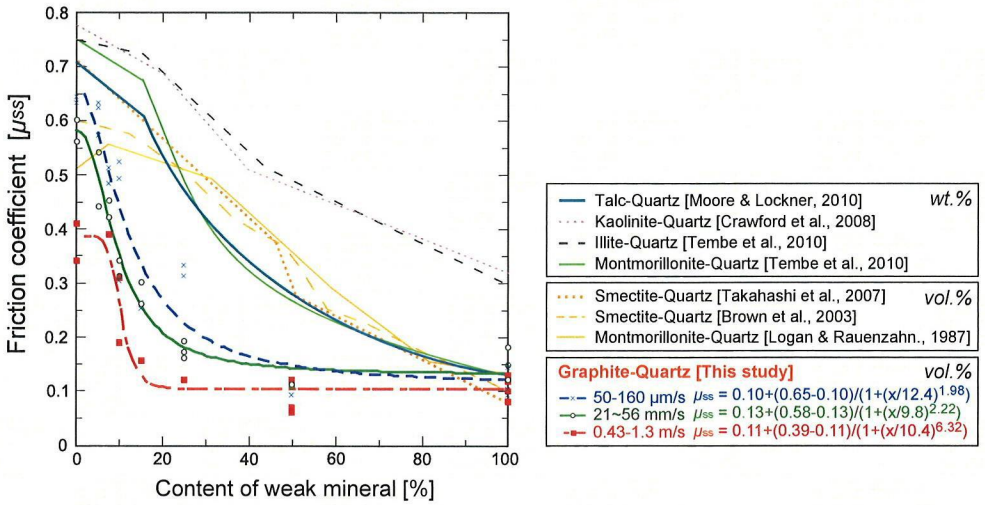

Fig. 4.6. Steady-state friction coefficient plotted against graphite content at three regimes of slip rate (thicker lines and symbols). Thick solid and dashed lines are sigmoid (power-law) fitting curves with each equation. For comparison, previous results on representative weakening agents are also illustrated.

Significance of gouge fabric for fault weakening is pointed out from Logan and Rauenzahn (1987); progressive shearing makes intensive comminution on stronger fragments until grain size is sufficiently reduced so that through-going shear (Y shear) and foliation of weak mineral can develop within the gouge. van Diggelen et al. (2009) and Elsworth et al. (2009) also suggest that the formation of an interconnected weak-mineral networks (e.g. talc) by increasing shear strain (γ > 15–25) is needed for effective fault weakening. On the 28 vol.% graphite gouge, the interconnected layers of graphite parallel to the Y and P surfaces are developed in the slip-localized zone (Figure 4.4j). On the other hand, the throughgoing slip surface characterized by the interconnected graphite matrix is formed in the slip-localized zone of 11.6 vol% mixture gouge at the steady state (Figure 4.4h). Our mechanical data and microscopic observation demonstrates that both characteristic steady-state textures are responsible for the weakening of graphite gouge, same as other weak phyllosilicate gouges.

Possible explanation for intensive weakening by graphite may be attributed to peculiar physical properties of graphite; extremely low friction coefficient and electrostatic separation energy (Moore and Lockner, 2004) than other weak phyllosilicate. Additionally, large shear strain (γ > 750) enabled by rotary-shear

apparatus must be taken into consideration.

4-5-4. Implication for natural faults

Our experimental work revealed that the graphite content and textural evolution of mixture gouge are keys for explaining weakening of graphite-rich fault zone. In many cases, graphite-rich fault zones are mainly consists of quartzo-feldspathic crushed fragments, ~10 wt% (12 vol%) of graphite; that is enough amount for significant weakening, and ± clay minerals in bulk content (Zulauf et al., 1990, Manatschal, 1999, Oohashi et al., 2011). Graphite-rich fault gouges are typically found from fault cores of the Ushikubi fault or the Tanakura tectonic line, besides development of composite planar fabric and slip-localized zone (principal slip zone) are also recognized and resemble to those in experimentally deformed gouge zone (compare Figure 2.1b and Figure 4.4j). Such weakening by graphite content increment and textural evolution can be possible in natural fault zones as a consequence of greater displacement. Although shallow faults often contains some extent of clay minerals, the effectiveness of graphite for fault weakening surely exceeds that of clay minerals because the weakening effect of 10 % content of graphite is equivalent to that of 30–60 % of montmorillonite and more than 65 % of illite and kaolinite (see Figure 4.6). The weakness of graphite may cause creeping fault motion (e.g. the Atotsugawa fault system; GSI, 1997) and possibly explain statically weak faults (Holdsworth, 2004; Collettini et al., 2009) in graphite-rich, metamorphic belts, buried sedimentary basins and accretionary prisms. Although it is still hard to extrapolate directly frictional property of graphite revealed in this study to the deeper seismogenic zone, the graphite lubrication possibly operates at the depths owing to its chemical and thermal stability.

4-6. Conclusions

The main conclusions of our experimental study are as follows.

1. I investigated frictional properties of graphite-quartz bimineralic gouge at various slip rates with more than a meter of slip displacement. The experiments clearly indicated that the friction coefficient of the bimineralic gouge decreases exponentially with

graphite content irrespective of slip-rate; it starts to reduce at the graphite fraction of 5 vol% and reached to the almost same level of pure graphite gouge at the fraction of 28 vol%. The non-linear, exponential trend that is different from linear trend of clay minerals (Figure 4.6) demonstrates the potential importance of graphite for the weakening agent of faults even if its amount is small.

2. The weakening by slight amount of graphite (< 12 vol%) is associated with grain size reduction, formation of slip surface and partial/throughgoing connection of graphite matrix along the surface. On the other hand, > 28 vol% of mixture shows interconnection of graphite parallels to the Y and P surfaces developed within the slip localized zone. Thus, the abrupt strength reduction around 10 to 15 vol% is attributed to the textural transition of localized slip to diffused graphite-matrix flow.

3. Comparison on graphite content and textural features with our experimental results and natural graphite-bearing faults revealed that the weakening by graphite can be possible in natural fault zones as a consequence of greater displacement. Although shallow faults often contains some extent of clay minerals, effectiveness of graphite for fault weakening surely exceeds that of clay minerals because the weakening effect of 10 % content of graphite is equivalent to that of 30–60 % of montmorillonite and more than 65 % of illite and kaolinite. This weakening may be more effective at depths where smectite could not exist anymore. The weakness of graphite even at low slip-rates may promote creeping fault motion or afterslip and one of the candidates for long-term fault weakening.

5. Mineralogical alteration with seismic fault motion under various atmospheres; Oxic, anoxic and reduction environment

5-1. Introduction

In last several years, experimental studies suggested that mineralogical transformation took place in a few tens of seconds during coseismic fault slip (e.g. Han et al., 2007a Han et al., 2007b; Brantut et al., 2008). Coincident with these experimental studies, reports from fault-drilling projects revealed mineral transformation along the principal slip zone (e.g. Mishima et al., 2006; Ikehara et al., 2007) which might had receive seismic slip. O'Hara et al. (2006) confirmed devolatilization and coalification (increment of vitrinite reflectance) of coal gouge by rapid frictional heating. The outcrop shown in Figure 2.2 is the Tanakura Western Marginal fault (the Inazawa outcrop; Awaji et al., 2010) with strike-slip displacement of more than a kilometer. The fault core mainly consists of foliated cataclasite and foliated fault-gouge zones (G1, G2, and G3 in Figure 2.2b). The matrix of these blackish gouge zones contains about 10 wt% of carbonaceous materials with particles <2 μm in size (arrows in Figure 2.2d). Although the degree of graphitization varies among the three gouge layers, the greatest degree of crystallinity of carbonaceous materials is in the principal slip zone G1′ between the G2 and foliated fault gouge zone (Figure 2.2b and d). Tanakura carbonaceous gouge zones are incohesive fault rocks that moved at anoxic shallow depths, so that pressure and temperature conditions during the formation of this gouge zones are far below those estimated previously from the natural occurrence of graphite in metamorphic rocks (e.g. 300–500 °C and 400–500 MPa by Diessel, 1978; Buseck and Huang, 1985) and by laboratory experiments (e.g. 600–900 °C and 600 MPa by Oberlin, 1984; Nover and Stoll, 2001; Wilks et al., 1993; Bustin et al., 1995). Hence, I speculate that the graphite forms in response to frictional heat during coseismic slip.

However, the graphitization processes along the fault zone are not understood yet. Thus, the first problem I address in this chapter is whether or not graphite can form in fault zones. I used commercial products of amorphous carbon and graphite as natural analogues to avoid complexities arising from natural carbonaceous materials with

different degrees of crystallinity (e.g. Itaya, 1981).

5-2. Experimental procedures

I used three starting materials for simulated fault gouge: (1) synthetic amorphous carbon powder (angular shape and grain size <45 μm, Strem Chemicals, Inc., product number 93-0601) , (2) highly crystallized natural graphite (platy shape and grain size <45 μm, Wako Pure Chemical Industries, Ltd., product number 072-03845) and (3) natural carbonaceous fault gouge. Additionally, the rock-to-rock experiments using Carrara marble were performed under specific atmospheric condition.

Friction experiments were performed using a rotary-shear, high-velocity friction apparatus (HVR) at Kochi/JAMSTEC (Shimamoto and Tsutsumi, 1994; Hirose and Shimamoto, 2005) and a rotary-shear, low to high-velocity friction apparatus (HDR) at Hiroshima University (Shimamoto and Hirose, 2006, Figure 5.1a). The experiments were conducted at normal stresses (σ_n) of 0.5 to 2.8 MPa, equivalent slip rates (V_e) of 50 μm/s to 1.3 m/s, and displacements of 0.09 to 118 m. Because the slip rate increases from the center to the periphery of the cylindrical specimens, I used the equivalent slip rate, V_e, defined such that $\tau V_e S$ gives the rate of total frictional work on a fault with area S, assuming a constant shear stress τ over the fault surface (Shimamoto and Tsutsumi, 1994). Hereafter, for convenience, I refer to "equivalent slip rate" as simply "slip rate" or "velocity".

Simulated fault gouge was placed between two cylinders of dolerite host rock with 25.0 mm diameters whose end surfaces were ground with SiC 80# powder (see Figure 5.1b). A Teflon sleeve of 24.9 mm in inner diameter was attached around the simulated fault zone to prevent gouge leakage. To correct for the effect of friction between the Teflon sleeve and the cylinders, I measured the shear traction caused by the sleeve in experiments without gouge, and then subtracted that traction from the measured raw data (see details in Appendix A). Thus, the effect of the Teflon sleeve is removed from the frictional data reported in this paper.

All starting materials and host rock cylinders were dried in an oven at 80 °C for at least 48 hours before experiments. The experiments used 0.3 g of amorphous carbon or 0.5 g of highly crystallized graphite to provide a consistent gouge thickness at

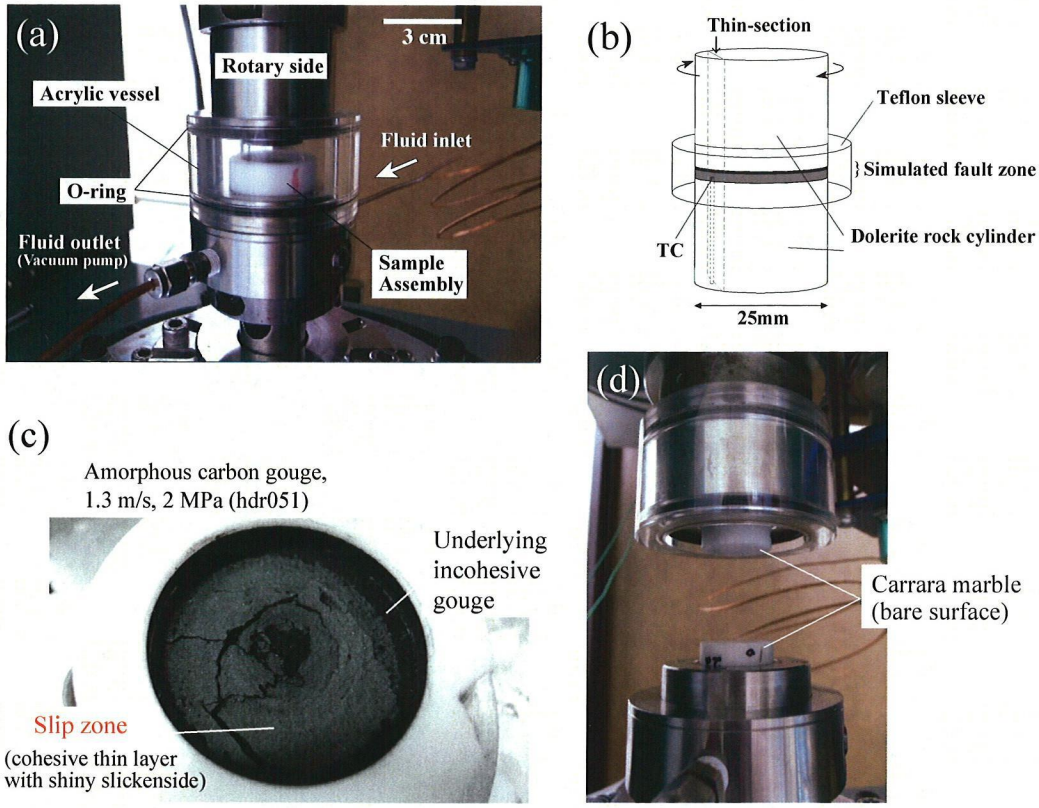

Fig. 5.1. (a) Photograph of the acrylic vessel and specimen holder configuration of the HDR apparatus for experiments in a N_2 atmosphere. (b) Specimen configuration used for the gouge experiments . Thin sections were made along the illustrated longitudinal section after the experiments. A thermocouple (TC) was placed 0.3 mm below the sliding surface in two experiments (hdr194, 195). (c) Slip surface of amorphous carbon gouge sheared at a slip rate of 1.3 m/s and normal stress of 2.0 MPa in a N_2 atmosphere (hdr051). The gouge from the cohesive thin layer was sampled for XRD analysis and TEM observation. (d) Photograph of the specimen configuration for rock-to-rock experiment on Carrara marble in H_2 atmosphere.

about 1 mm for all runs.

Experiments by the HDR apparatus were conducted under one of three atmospheric conditions: (1) in air at room temperature and humidity to simulate conditions near the ground, (2) in dry nitrogen (N_2) gas to simulate anoxic environments such as deep crustal depths and (3) in hydrogen (H_2) gas to simulate reduction environments. All experiments by the HVR apparatus were done in air. To achieve the anoxic / reduction environment, I placed a small acrylic vessel around the sample holder of the HDR apparatus (Figure 5.1a), evacuated it with a vacuum pump, and then charged it with N_2/H_2 gas, repeating this procedure three times before the experiment. I confirmed that relative humidity in the vessel was less than 2%, the detection limit of

the sensor. Rubber O-rings were placed at the top and bottom of the acrylic vessel (Figure 5.1a) to prevent gas leakage. The measured torque supported by the O-rings was <0.05 N/m, corresponding to shear stress of ~0.01 MPa. In some experiments (hdr194, 195; Table 1), a K-type (chromel-alumel type) thermocouple was placed 0.3 mm below the sliding surface to measure the temperature of the simulated fault zone.

In some experiments using the HVR apparatus, I examined the chemical transformation of carbon to CO_2 gas during the experiment by setting a solid electrolyte-type CO_2 sensor (TGS4161, Figaro Co. Ltd.) with response time of about 2 s. The sensor was placed approximately 50 mm away from the specimen holder (Figure 3.2a). The experimental conditions and results are summarized in Table 1.

5-3. Results

5-3-1. Mechanical behaviors of experiments for atmospheric and N_2 purged conditions

I found no significant difference in the mechanical behavior of amorphous carbon gouge sheared under atmospheric and N_2 purged, anoxic environments at high slip rates (Figure 5.2b). In amorphous carbon gouge deformed at a slip rate of 1.3 m/s and normal stress of 2.0 MPa in air, the emission of CO_2 gas was detected (2894 ppm maximum) at 2.4 s after the onset of experiment, and its concentration increased continuously with displacement (Figure 5.2c). I also detected emission of CO_2 from graphite gouge (in trial hvr1555, not shown in Figure 5.2), although the CO_2 concentration was over two orders of magnitude less (approximately 40 ppm at the maximum). This result suggests that although carbonaceous material emits CO_2 gas during seismic fault motion, the CO_2 concentration depends strongly on the crystallinity of the material.

5-3-2. Fault zone microstructures and mineralogical analysis for gouge experiments

All high-velocity experiments on amorphous carbon and graphite resulted in the development of shiny slickenside surfaces between the rotational-side of dolerite host rock and the gouge zone. Less shiny slickenside surfaces were also recognized for specimens deformed at low slip rates. Microscope and SEM (scanning electron microscope) observations on a thin section (see Figure 5.1b for orientation) reveal a slip

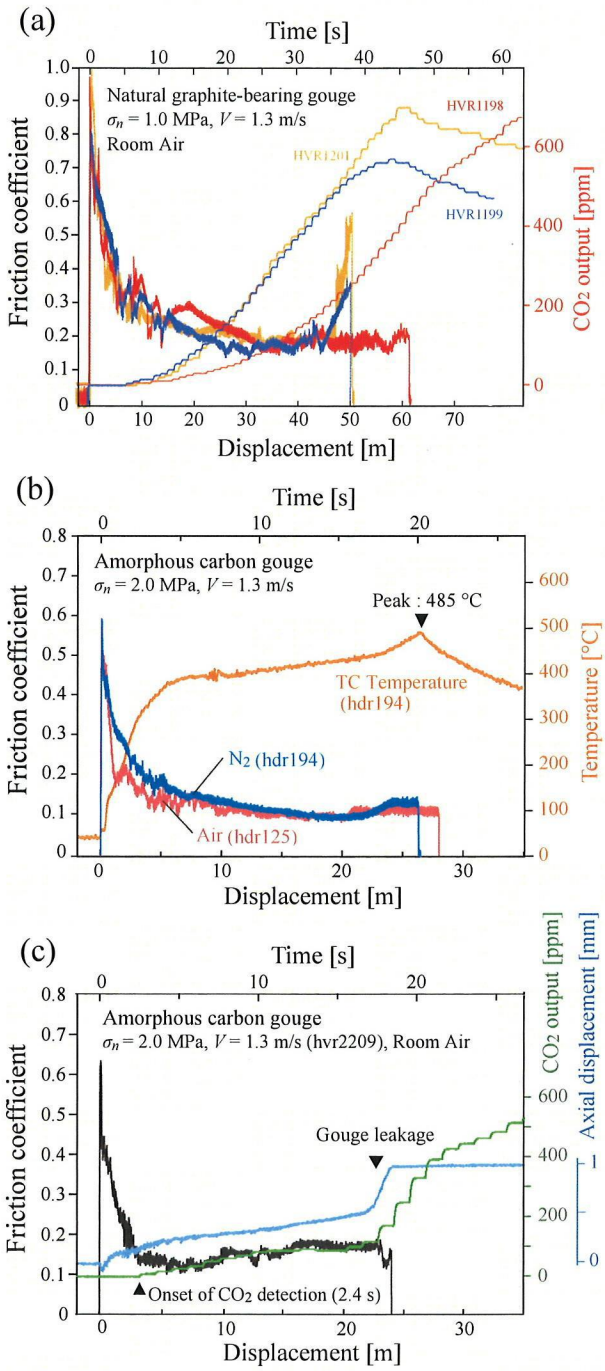

Fig. 5.2. (a) Mechanical behaviors of natural graphite-bearing fault gouges of the Ushikubi fault under oxic (room air) environments at a slip rate of 1.3 m/s and normal stress of 1.0 MPa. Outputs from CO_2 sensor also plotted against time. (b) Mechanical behavior of amorphous carbon gouge under oxic (air) and anoxic (N_2) environments at a slip rate of 1.3 m/s and normal stress of 2.0 MPa (hdr125 and hdr194, respectively). Temperature near sliding surface measured by thermocouple is also shown by orange line (run hdr194). (c) Representative mechanical data at same conditions as those in (b), plus axial shortening of gouge zone thickness and CO_2 concentration in the specimen chamber.

zone of about 65 μm in width of amorphous carbon deformed at a slip rate v of 1.3 m/s and at a normal stress σ_n of 1.0 MPa (Figure 5.4a; reflected light image). The slip zone is more compacted and appears bright colored. Almost no grain size reduction and fabric development are recognized in the weakly deformed zone. Observation of graphite gouge deformed at v = 0.04 m/s and σ_n = 1.0 MPa in a thin section with a similar orientation reveal a well-compacted slip zone of about 50 μm in width (Figure 5.4b; reflected light image). In the weakly deformed zone, grain size is unchanged, but weak foliation forms.

Slickenside surfaces in amorphous carbon (Figure 5.4c; sheared at v = 1.3 m/s and σ_n = 1.0 MPa) and graphite (Figure 5.4d; sheared at v = 1.3 m/s and σ_n = 1.0

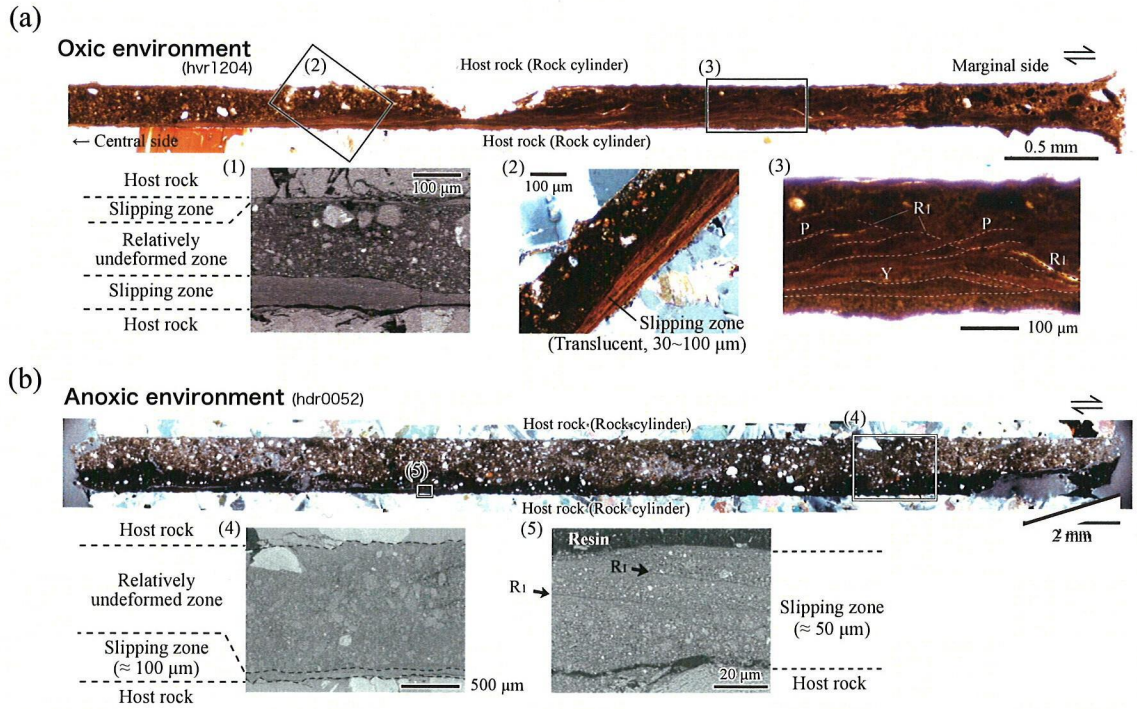

Fig.5.3. Photographs of the thin sections under optical microscope (cross-polarized light) and SEM images of recovered samples from HV friction experiment. (a) Sample recovered from experiment under oxic environment (hvr1204). Half side of the thin section is shown in the diagram. (1) SEM image (backscattered electron image: BEI) obtained from opposite marginal side of identical thin section. (2) Carbonaceous material that is an opaque material is not recognized from slipping zone. (3) Preferred orientation of clay mineral and composite planar fabric are developing along the strain localization zone (slipping zone). (b) Sample recovered from experiment under anoxic environment (hdr0052). (4) SEM image (BEI) obtained from boxed area. Slipping zone of 50-100 μm in thickness is also recognized between hostrock and gouge zone. (5) Detailed SEM image (BEI) of slipping zone. Finely comminuted fragments (less than few micron) and ridel shear (R1) are recognized within the zone. The presence of resin is an artifact due to the thin section preparation.

MPa)are smooth surfaces with fine grooves formed parallel to the slip direction. Fine carbon particles of micrometres to submicrometre sizes constitute the slickenside surface of amorphous carbon (Figure 5.4c) and those grains are finer than the grains in weakly deformed zone immediately underneath the surface (Figure 5.4c). Most experiments on amorphous carbon were conducted in air and some carbon along the slip surface must have disappeared by oxidation transforming to CO_2 (Figure 5.2c). On the other hand, larger grains of several tens of micrometres in size can be recognized on the slickenside surface of graphite (inset of Figure 5.4d) and texture suggests that platy graphite grains are aligned nearly parallel to the surface. Graphite has a well-known sheet structure (e.g., Inagaki and Kang, 2006), so that graphite grains seem to have rotated without much grain crushing to form foliation.

To examine the mineralogical changes during high-velocity experiments in a N_2 atmosphere, XRD (X-ray powder diffraction) analysis was performed on material from both the slip zone and the weakly deformed zone. XRD analyses were performed on a Rigaku MultiFlex-2kW apparatus with the following measurement conditions: Cu-Kα radiation, X-ray generator at 40 kV, 40 mA, scanning step 0.02, scanning speed 2/min, divergence slit 1°, scattering slit 1° and receiving slit 0.15 mm. A sample from the slip zone of amorphous carbon deformed in N_2 purged atmosphere at a slip rate of 1.3 m/s displays a diffraction peak at 3.3 Å corresponding to the spacing distance on the graphite (002) plane (upper curve in Figure 5.5a), whereas no diffraction peaks are seen in samples of the starting amorphous carbon (the bottom curve in the same Figure). A sample from weakly deformed zone of the same specimen shows a small diffraction peak at about the same place (second curve from the top in Figure 5.5). It is well known that the spacing distance of the (002) crystal surface in carbonaceous material, d_{002}, becomes small with increasing crystallinity (e.g., Landis, 1971; Inagaki and Kang, 2006). The d_{002} values of the slip zone materials were always smaller than those of the weakly deformed zone (see Table 1), approaching the ideal (002) spacing of graphite (3.335 Å) with increasing displacement, and peak intensity also tended to increase with displacement (Figure 5.5b). In contrast, no diffraction peak was found in the experiments in air even in the slip zone (hdr125 in Figure 5.5a), graphitization did not take place after rapid slip in oxic conditions. Additionally, the clear diffraction peak of the graphite was hardly detected from the slip zone samples deformed at low to intermediate slip rates to displacement of 20–36.5 m (hdr066, hvr2264 in Figure 5.5a).

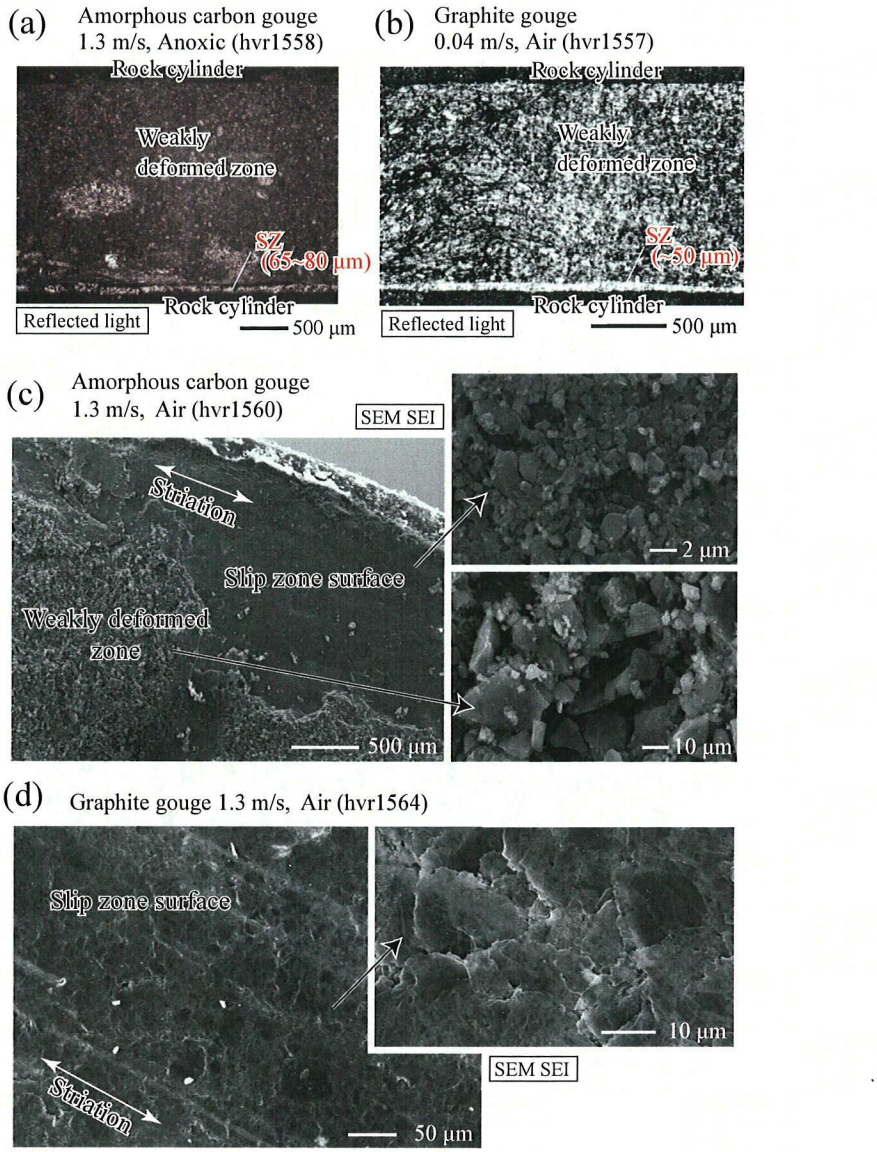

Fig. 5.4. Reflected light micrographs of thin section of amorphous carbon (a) and graphite gouges (b). (a) amorphous carbon gouge sheared at a slip rate of 1.3 m/s and normal stress of 1.0 MPa under anoxic condition, showing a slip zone (SZ) 65~80 μm thick between the rock cylinder and gouge zone that corresponds to the cohesive thin layer. (b) graphite gouge sheared at a slip rate of 0.04 m/s and normal stress of 1.0 MPa, showing a slip zone ~50 μm thick between the rock cylinder and gouge zone. (c) SEM secondary electron images of slip surface and weakly deformed zone of amorphous carbon gouge sheared at a slip rate of 1.3 m/s and normal stress of 1.0 MPa. Upper and lower insets show magnification of slip zone and weakly deformed zone, respectively. Grain size reduction (down to a few micrometres to sub-micrometre in diameter) and increase of roundness are observed from slip surface. (d) SEM secondary electron images of slip surface of graphite gouge sheared at a slip rate of 1.3 m/s and normal stress of 1.0 MPa. The inset shows magnification of slip zone. Preferably oriented graphite particles making very smooth slickenside.

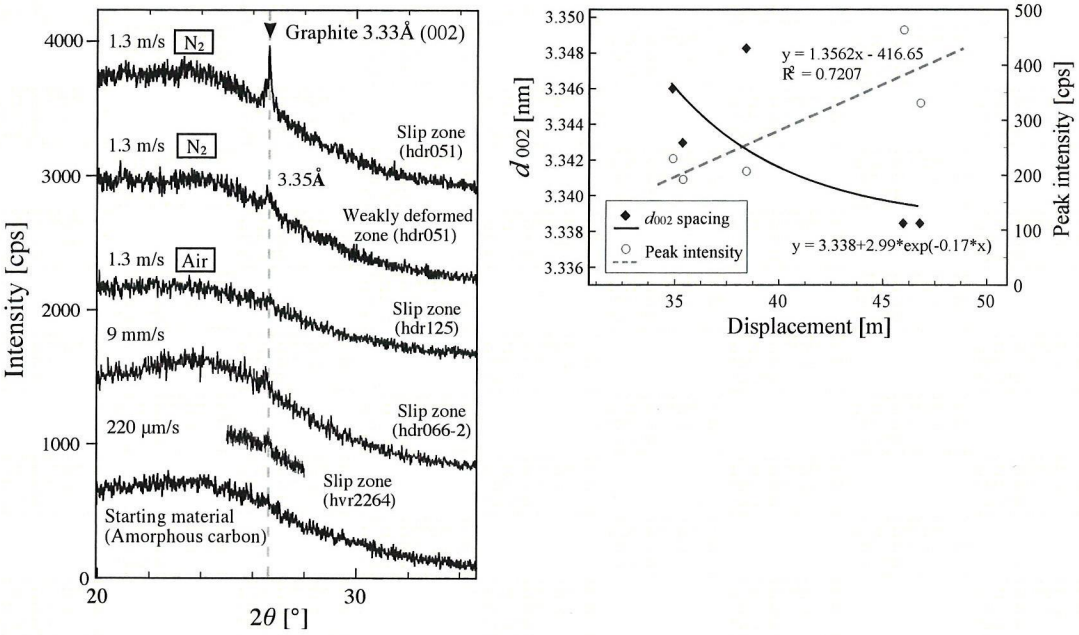

Fig. 5.5. (a) Representative X-ray diffraction patterns of amorphous carbon gouge before and after experiments at slip rates of 220 μm/s, 9 mm/s and 1.3 m/s in air and N2 atmospheres. Graphite (002) diffraction (3.33 Å) is only recognized on recovered material sheared at a slip rate of 1.3 m/s in the N2 atmosphere. For recovered sample of hvr2264, measurement was done only from 25 to 28 ° of theta angle. Patterns are offset for visibility. (b) Evolution of peak position and peak intensity of graphite (002) diffraction in slip zone material with increasing displacement. All experiments are conducted at slip rate of 1.3 m/s. The d002 spacing (solid line) decreases exponentially toward the 3.338 Å closely ideal d002 spacing of graphite (3.335 Å).

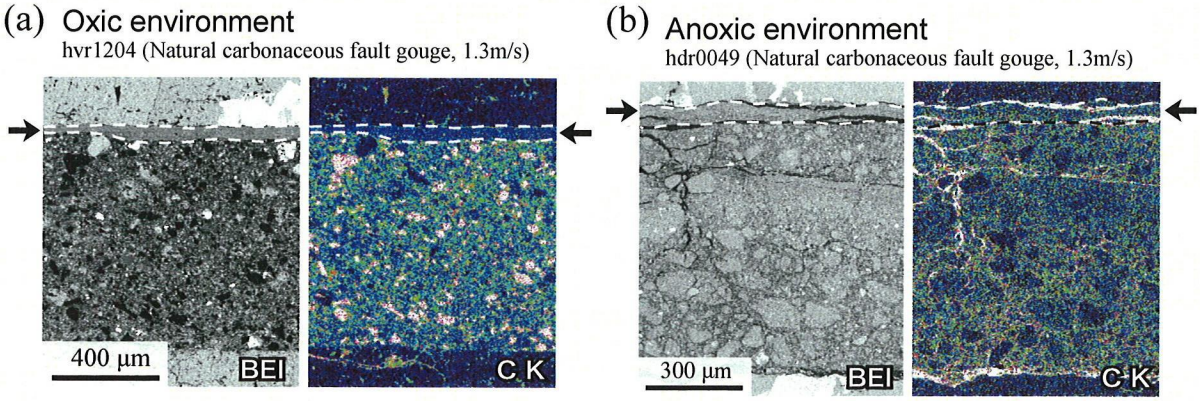

Fig.5.6. SEM backscattered electron image (left side) and EDS elements mapping (right side) of experimentally deformed natural carbonaceous fault gouge. Black arrow shows the position of slipping zone. (A) Sample recovered from experiment under oxic environment (hvr1204). There is almost no detection of carbon (C K) from slipping zone. Spotty carbon detection within the relatively undeformed zone corresponds to the resin due to the fell away of the crushed fragments during the thin section preparation. (B) Sample recovered from experiment under anoxic environment (hdr0049). No significant difference is recognized on carbon amount along the slipping zone.

I performed TEM (transmission electron microscope) observation for the amorphous carbon gouge prior and after the high-velocity friction experiment. A JEOL JEM-2010 high-resolution TEM equipped with an energy dispersive spectrometer under an accelerating voltage of 200 kV is used for observation For preparation of TEM specimens, gouge powder was suspended in ethanol, then dropped onto a copper microgrid with elastic substrate without carbon coating. Under the TEM, the starting material showed typical amorphous textures throughout the specimen (maze pattern, Figure 5.7a). In contrast, the same materials in the slip zone underwent high-velocity friction experiment displayed particles with characteristic lattice fringes (Figure 5.7b) that resemble those of graphite formed by heat treatment of coke at 1100–1300 °C (Inagaki and Kang, 2006). Thus, both XRD and TEM analyses clearly indicate that graphitization of amorphous carbon occurred only at high slip rates in the N_2 environment.

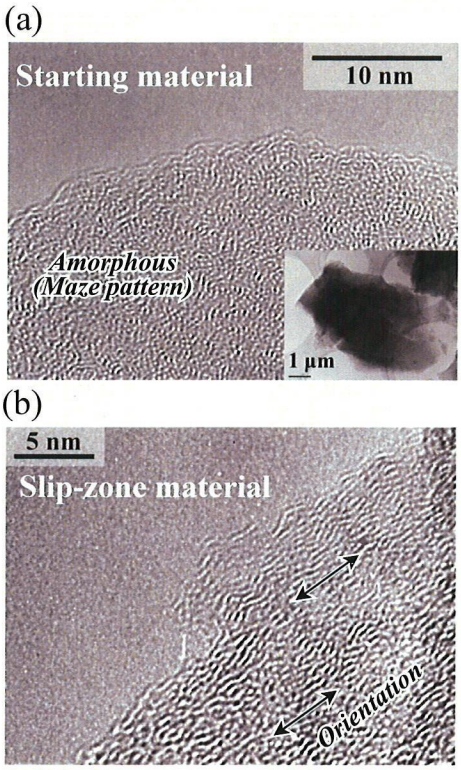

Fig. 5.7. TEM images of amorphous carbon starting material (a) and slip zone material recovered from an experiment at a slip rate of 1.3 m/s in the N_2 atmosphere; hdr051 (b).

5-3-3. Results of HV experiment on Carrara marble sheared at reducing atmosphere

Rock to rock experiments of the Carrara marble were conducted at σ_n of 2.0 MPa and V of 1.3 m/s under the H_2 purged atmosphere. Representative frictional behavior in Figure 5.10 shows initial high peak friction coefficient μ_p of 0.59 and subsequent exponential decreasing with displacement toward a steady-state friction coefficient μ_{ss} of 0.12 ± 0.02. These behaviors are quite comparable to those of experiments under room-air (oxic environment) and Ar (dry argon gas)-flux (anoxic environment) atmosphere (Han et al., 2010). However, I can observe patches of blackish material on the slip surface deformed under the H_2 atmosphere (Figure 5.11), whereas the slip surface deformed under the air/Ar atmosphere maintains original white

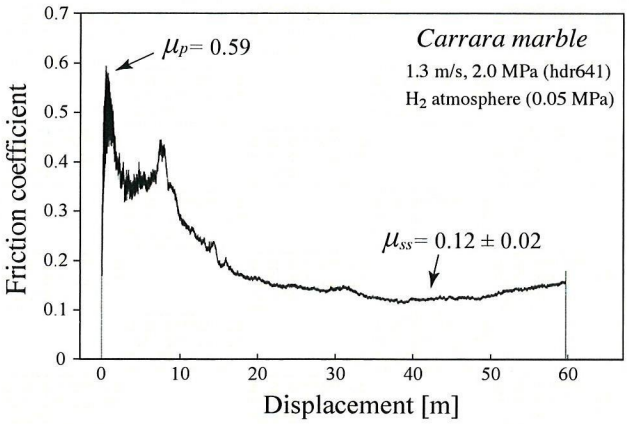

Fig. 5.10. Representative frictional behavior of rock-to-rock experiment on Carrara marble at a slip rate of 1.3 m/s and normal stresses of 2.0 MPa. Experiment was done under H_2 purged atmosphere (reducing environment) with pressure vessel.

Fig. 5.11. Slip surface of sheared Carrara marble. Experiment are conducted at V=1.3 m/s and normal stress of 3 MPa under H_2 purged atmosphere. Blackish materials stick on the originally white-colored surface.

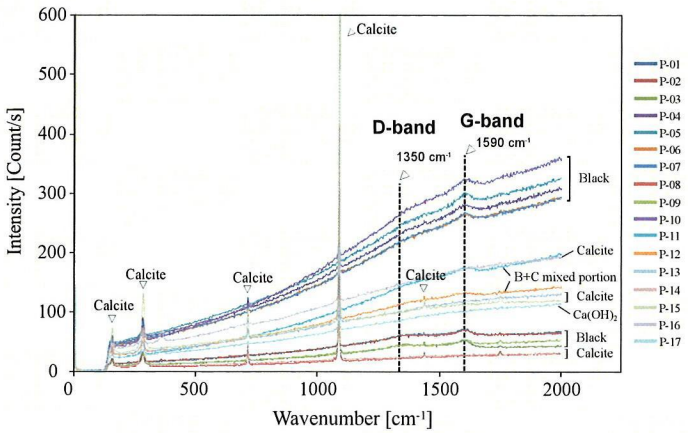

Fig. 5.12. Raman spectra for sliding surface of Carrara marble deformed under reducing atmosphere showing wave numbers characteristic of calcite and graphite. Graphite is identified both by peak at a wavenumber of 1350 cm^{-1} and 1590 cm^{-1}, from blackish portion on the surface.

color (Han et al., 2010). To determine the origin of black color, I conducted laser Raman spectroscopic analysis for the slip surface. Results are shown in Figure 5.12. Measurements were conducted for three different areas; (1) surfaces of decomposed material, (2) patches of blackish material beneath the decomposed material and (3) Original calcite surface beneath the decomposed material and blackish material. As a result, fundamental peaks of the calcite at a wavenumber of 1085, 280, 711 and 155 cm^{-1} were detected from (1) and (3). On the other hand, not only calcite peaks but also additional two broad peaks, 1350 and 1590 cm^{-1} in wavenumber were detected from the

patches of blackish material. These two peaks are known to originate from carbonaceous materials (or graphite).

5-4. Interpretation and discussion

5-4-1. Thermal oxidation of carbonaceous minerals

In our experiments in air, emission of CO_2 gas was detected immediately after the onset of sliding. One possible source of CO_2 is carbonates in the gouge, and CO_2 degassing has been reported in similar experiments on calcite, siderite, and dolomite (Han et al, 2007a, b; De Paola et al., 2011). However, I used pure amorphous carbon and graphite powders as starting materials, and the host-rock dolerite did not show any patterns typical of carbonates in XRD measurements. It is well known that amorphous carbon and graphite starts to react with oxygen (thermal oxidation reaction) at about 300–400 °C and 450–500 °C, respectively, in an oxic environment (Boylan, 1996; Xiaowei et al., 2004):

$$C + O_2 \rightarrow CO_2 \quad (10)$$

Thermocouples placed 0.03 mm from the sliding surface showed that the temperature reached 300 °C within 2–3 s after the onset of sliding (Figure 5.2b), which is high enough to trigger thermal oxidation. The time of the first emission of CO_2 is nearly consistent with the time at which 300 °C was reached (Figure 5.2a and b), strongly supporting thermal oxidation.

Our experiments demonstrated that frictional heating by rapid coseismic sliding induces immediate oxidization of carbon minerals in fault zones under oxic conditions typical of shallow crustal depths. CO_2 gas emission has been observed along natural faults (e.g., the Atotsugawa fault; Saito et al., 2006) and is considered to result from dissolution of carbonate rocks, volcanic gas, and organic soil compounds. Our results suggest that thermal oxidation of carbonaceous minerals is another possible source of CO_2 gas along natural faults, especially in carbon-rich sedimentary rocks (e.g., inland or forearc basins and accretionary prisms) if oxic environments are present in fault zones.

5-4-2. Graphitization of amorphous carbon and geological evidence of seismic fault motion

In our experiments under an N_2 environment, amorphous carbon did not oxidize into CO_2 but underwent partial graphitization (Figures 5.5a and 5.7b). Graphitization occurs for (1) static heating at 1000–2200 °C (Oberlin, 1984), (2) heating at 500 °C under 0.6 GPa pressure for more than 1 month (Nover and Stoll, 2001), (3) simple shear deformation at pressures of 0.8–1.0 GPa, a temperature of 900 °C, and a duration of a few to hundreds of hours (Wilks et al., 1993; Bustin et al., 1995), and (4) temperatures of 300–500 °C at pressures of 0.4–0.5 GPa over geologic time (e.g. Diessel, 1978; Buseck and Huang, 1985). However, none of these conditions were met in our high-velocity experiments with an applied normal stress of <3 MPa, temperatures <500 °C, and duration of less than hundreds of seconds.

One possible cause of graphitization during our high-velocity experiments is flash heating at microscopic asperity contacts of gouge particles (Archard, 1958/1959). Although the original theory of flash heating assumed sliding asperities on two parallel planes, the concept also could be applied to the microscopic contacts between gouge particles being sheared within a narrow slip zone. Flash temperature (T_f) at the asperity contacts is estimated by the equation:

$$T_f = 0.25\beta(\mu\pi P_m/\rho C_p)(aV/2\kappa) \quad (11)$$

where the dimensionless Peclet number, $L = aV/2\kappa$, is between 0.1 and 0.5, β is an empirical constant of 0.95, μ is friction coefficient, P_m is yield strength, a is asperity contact radius, V is slip rate, κ is thermal diffusivity, ρ is density, and C_p is heat capacity. The material properties of amorphous carbon used for the estimates are: ρ = 2000 kg/m^3, C_p = 710 J/kgK, $\kappa = 6.5 \times 10^{-6}$ m^2/s, and P_m = 2 GPa (estimated by converting the Shore hardness of 100–120 (Inagaki and Kang, 2006) to the indentation hardness). In the case of a = 2 μm based on the SEM observation, μ = 0.17 and V = 1.3 m/s, the estimated flash temperature is 50.5 °C. Thus, the maximum temperature expected at the asperity contacts at the steady-state, which is the summation of background temperature (i.e. temperature measured by thermocouples in Figure 7a) and flash temperature, is estimated to be ~600 °C. Although flash temperature rise is not so large due to the low yield strength of amorphous carbon in our experiments, flash temperature rise may affect the graphitization. In addition, stress concentration at asperity contacts of gouge

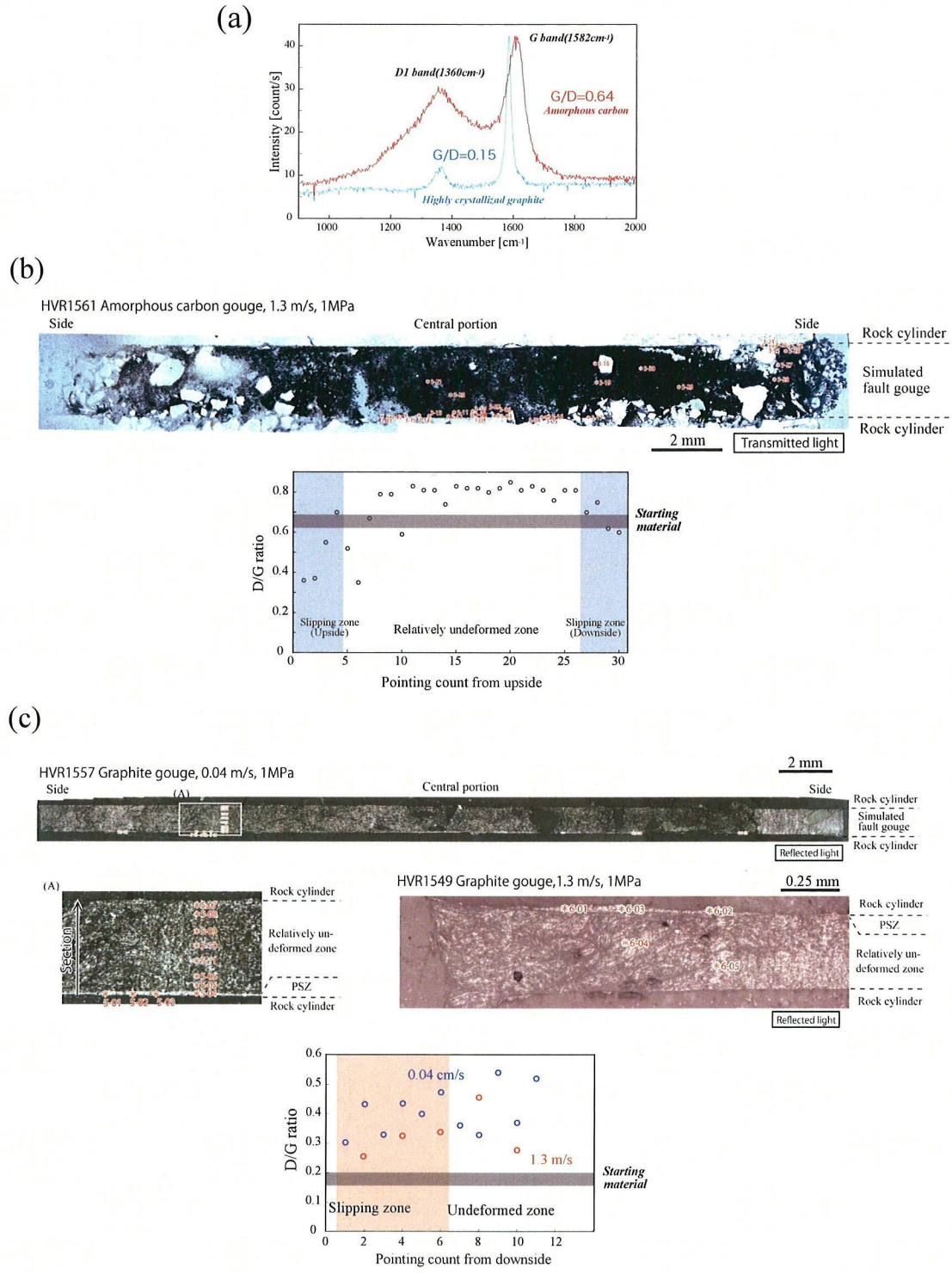

Fig. 5.8. (a) Examples of Raman spectrum from synthetic amorphous carbon powder (in red line) and highly crystallized graphite powder (in blue line) used for the experiments in Chapters 3 and 4. Laser Raman spectroscopic analysis on sheared gouge of (a) amorphous carbon and (b) graphite gouge for evaluation of crystallinity on carbonaceous materials. A crystallinity factor; D/G ratio, across the gouge zones are illustrated in diagrams.

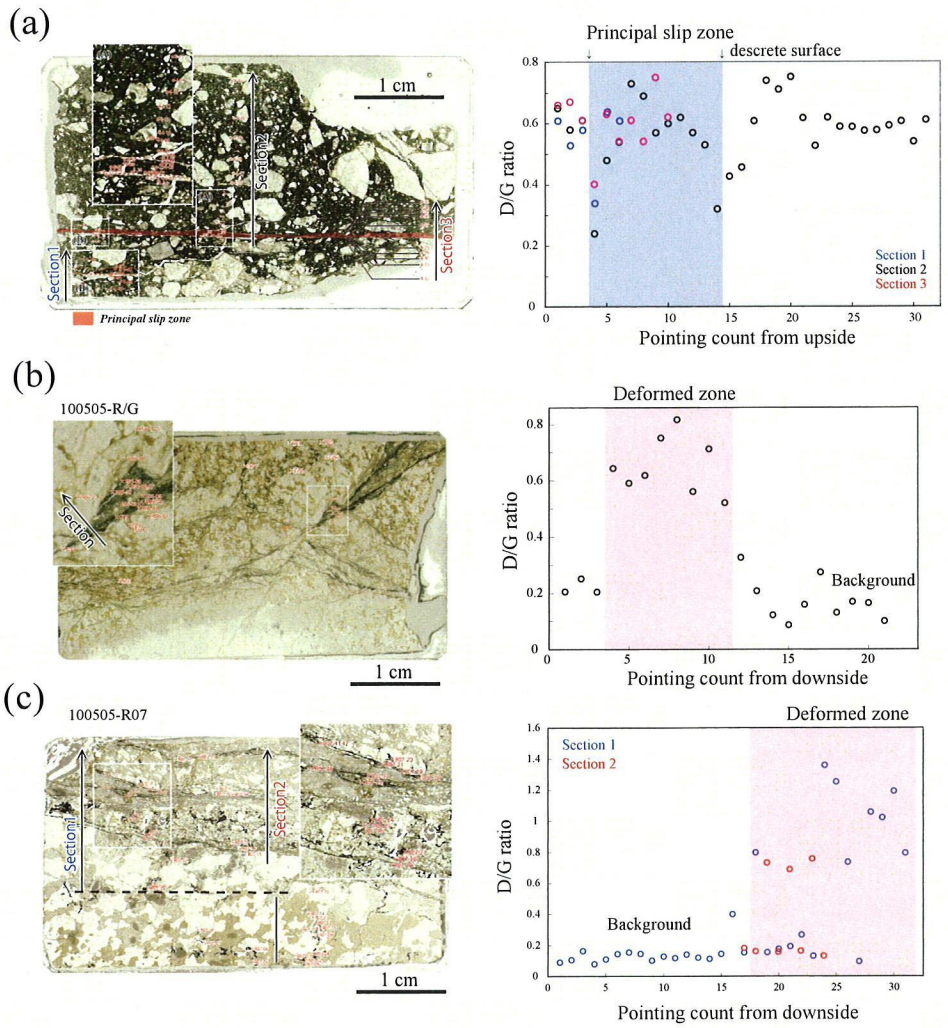

Fig. 5.9. Laser Raman spectroscopic analysis on natural carbonaceous fault rocks. (a) The principal slip zone penetrates within the pelitic rock of the Mino accretionary complex. (b) Carbonaceous shear band from the A4 fault strand of the Ushikubi fault.

particles also yields short-lived high stresses (a few GPa) that may contribute to graphitization.

Another possible cause of graphitization is shear strain (Wilks et al., 1993; Bustin et al., 1995), which in our case was more than 10,000. Although it is not clear which effect might predominate, both thermal and mechanical forces at asperity contacts must contribute to graphitization during high-velocity experiments under anoxic conditions. This explanation is consistent with the graphitization observed only within the slip zones sheared at high slip rates (Figure 5.5a) and with the partial graphitization observed only at possible rims of amorphous carbon grains under the TEM (Figure 5.7b). In the case of oxic conditions, thermal oxidation takes place prior to the graphitization and the amorphous carbon transforms into CO_2 gas. This behavior is why the graphitization of the amorphous carbon could not be found in the sample deformed under oxic conditions.

The transformation of carbonaceous minerals by thermal oxidation (in oxic conditions) and graphitization (in anoxic conditions) may leave geological records, as carbonaceous material is chemically stable and not prone to dissolution. For example, by observing thin continuous graphite-rich layers within a fault zone composed of low crystallinity carbon, one could infer that the graphite formed during seismogenic fault motion. If carbonaceous minerals are missing in a slip zone within a fault zone containing carbonaceous minerals, the zone was likely subjected to seismogenic fault motion under oxic conditions near the ground surface. Based on such evidence, I identified G1′ in Figure 2.2 in the Tanakura fault as the principal slip zone during past seismogenic fault motion at depths. Identification of slip zones which accommodated fault motion is not always easy, but such changes in carbonaceous minerals may lead to a way of identifying coseismic slip zones in natural fault systems.

5-4-3. Implications for presence of graphite and amorphous carbon on fault mechanics

Graphite is well known for its use as a solid lubricant, and in our experiments the friction coefficient of graphite powder was very low over a wide range of slip rates whereas that of amorphous carbon became low only at slip rates greater than a few centimeters per second, similar to other rock-forming minerals (Wibberley et al., 2008). These results have important implications for earthquake geology and fault mechanics. In general, carbonaceous materials are ubiquitous in pelitic rocks in sedimentary basins,

metamorphic belts or accretionary complexes. Fault zones in such tectonic regions are often enriched with carbonaceous minerals (Zulauf et al., 1990; Manatschal, 1999; Awaji, 2006; Oohashi and Kobayashi, 2008). Once rapid faulting occurs within such a fault zone at anoxic depths, the fault could become dramatically weak or slippery at all slip rates due to the generation of graphite by coseismic faulting. This weakening is effective at depths where potentially stable minerals, such as smectite (Saffer and Marone, 2003), could not exist anymore. If graphite is widespread, with the development of continuous and/or interconnected layers of graphite within the fault zones, a long-term weak fault zone (Holdsworth, 2004; Collettini et al., 2009) may be created, because graphite is weak at the wide range of slip velocities (Figure 3.8). How effective this lubrication becomes, depends on the graphite content and slip zone structures.

High-velocity friction experiments have demonstrated dramatic weakening of faults without frictional melting at slip rates greater than the order of 10 mm/s (e.g., Di Toro et al., 2004; Han et al., 2007a; Hirose & Bystricky, 2007; Mizoguchi et al., 2009). Surprisingly, the overall behavior of amorphous carbon is quite similar to those behaviors; i.e., fairly high friction at low to intermediate slip rates, but dramatic weakening at high slip rates. Amorphous materials have received attention since they forms during frictional sliding (Yund et al., 1990) and silica gel, a form of amorphous materials, is proposed to cause such weakening (Goldsby and Tullis, 2002; Di Toro et al., 2004). Previous experiments are inconclusive in this regard since amorphous materials form during frictional slip and may not be controlling the entire behavior. I did use amorphous carbon as the starting material, and given that the host-rock dolerite is stronger, I believe that the amorphous carbon is likely to control the overall behavior. Friction experiments using a variety of amorphous materials from rocks are needed to resolve this important issue.

5-4-4. Formation of graphite with seismic faulting under the reducing atmosphere

A slip surface of Carrara marble after the HV friction experiment under H_2 atmosphere displays completely different in color from that sheared under air and Ar atmospheres. According to the laser Raman spectroscopic analysis, not only calcite peaks but also two broad peaks originate from graphite were detected from the patches of blackish material. The Carrara marble used for the experiment is very pure and

composed of 99% calcite (there is very small amount of silicate). Thus, it is unlikely that graphite appeared from carbonaceous material originally presents in the rock. The appearance of solid carbon is attributable to the atmospheric difference, since no visible color change was observed prior and after the HV friction experiment under the air and Ar atmospheres (Han et al., 2011 and unpublished data), furthermore, another experimental conditions are the same with those of experiments. One possible explanation is formation of graphite via gas phase reaction of eq (1). Salotti et al. (1971) conducted reaction experiment of calcite at the temperature of 500°C, gas pressure of 13.8 MPa and duration of 6 hours under C-O-H atmosphere, and demonstrated formation of well-crystallized graphite on the surface of calcite. Although two of these conditions were not met in my high-velocity experiments with gas pressure of 0.1 MPa and duration of less than hundreds of seconds, temperature must have exceeded 500 °C since calcite decomposed into CaO and CO_2 (decomposition temperature of calcite: >720 °C). The reaction of eq (1) is temperature dependent so this is why this reaction accomplished at these experimental conditions. This result suggests that if rapid faulting occurs within the calcareous rocks (e.g., marble, limestone and rock rich in carbonate vein) under the reducing environment (H_2 or CH_4 atmosphere), graphite forms in response to frictional heating. These experiments and analyses are not enough to understand entire forming processes of graphite, this may be accountable for another formation/concentration mechanism of graphite along the fault zones. High-velocity fiction experiments under various atmospheric conditions are needed to resolve depth diversity of reaction influenced by redox environment.

5-5. Conclusions

The main conclusions of our experimental study are:

1. Our experimental results from all of three gouges at room air atmosphere shows that carbonaceous minerals may oxidize, and emission of CO_2 will take place with seismic slip velocities. This coseismic gas production may trigger a pore pressure rise even under dry condition. In consequence, reduction of normal stress and shear resistance may happen. One possibility to account CO_2 gas detected by fault gases observation on

the Atotsugawa fault system is this thermal oxidation reaction of carbon.

2. Graphitization (crystallization) of amorphous carbon was recognized in the slip zone, which underwent frictional heating due to rapid sliding. XRD analyses and TEM observations suggest that thermally and mechanically driven mineral transformation at asperity contacts contributes to graphitization during high-velocity experiments under anoxic conditions. Therefore, graphitization of amorphous carbon may be a possible indicator of paleoseismic faulting, as carbonaceous minerals are chemically stable on a geologic timescale at anoxic depths.

3. Once rapid faulting occurs within the carbon-rich, anoxic fault zones that typically occur in accretionary complexes, fault might become slippery by the generation of graphite. The presence of graphite could contribute to slow deformation, such as slow slip events observed along subduction zones, as graphite shows low friction over the wide range of slip rates. Thus, mineralogical transformation of carbonaceous minerals by rapid faulting may play an important role in fault behavior at seismogenic depths.

4. Rock to rock, high-velocity friction experiments of Carrara marble were conducted under the H_2 purged atmosphere. According to the laser Raman spectroscopic analysis, carbonaceous material was recognized from blackish deposits on the slip surface. One possible explanation is formation of graphite via gas phase reaction of following equation $CO_2 + 2H_2 \rightarrow 2C + 2H_2O$. The reaction may be enhanced by production of CO_2 gas and elevated temperature due to the rapid sliding. The experimental result proposes another possible mechanism to produce/concentrate carbonaceous materials along the calcareous fault zone.

6. DISCUSSIONS AND IMPLICATIONS FOR FAULT CREEP OBSERVED ALONG THE ATOTSUGAWA FAULT SYSTEM

In this Chapter, I will discuss the origin of fault creep and microearthquakes observed along the Atotsugawa fault system from integrated aspects of natural fault occurrences, experimental results and geophysical datum reported from the Atotsugawa fault system.

6-1. Comparison of experimental and natural faults, aspects from mineral composition, microstructure, and frictional strength

Our experimental work revealed that the graphite content and textural evolution of mixture gouge are keys for explaining weakening of graphite-rich fault zone (discussed in Chapter 4). In many natural cases, graphite-rich fault zones are mainly consists of quartzo-feldspathic crushed fragments, ~10 wt% (12 vol%) of graphite; that is enough amount for significant weakening, and ± clay minerals in bulk content (Zulauf et al., 1990, Manatschal, 1999, Oohashi et al., 2011). Graphite-rich fault gouges are typically found from fault cores of the Atotsugawa fault system including the Ushikubi fault, or the Tanakura tectonic line, besides development of composite planar fabric and slip-localized zone (principal slip zone) are also recognized and resemble to those in experimentally deformed gouge zone (compare Figure 2.1b and Figure 4.4j). Therefore, such weakening by graphite can be possible in actual fault zones as a consequence of greater displacement. Although shallow faults often contains some extent of clay minerals, the effectiveness of graphite for fault weakening surely exceeds that of clay minerals because the weakening effect of 10 % content of graphite is equivalent to that of 30–60 % of montmorillonite and more than 65 % of illite and kaolinite (see Figure 4.6). The weakness of graphite possibly explains statically weak faults (Holdsworth, 2004; Collettini et al., 2009) in graphite-rich, metamorphic belts, buried sedimentary basins and accretionary prisms. Although it is still hard to

extrapolate frictional property of graphite revealed in this study directly to the deeper seismogenic zone, the graphite lubrication possibly operates at the depths owing to its chemical and thermal stability.

6-2. Evolution process of "graphitic fault zone"; a model case of the Atotsugawa fault system

In this thesis, field studies along the Atotsugawa fault system have shown the two types of mechanisms for carbon enrichment; (1) precipitation of graphite precipitation from C-O-H fluid and (2) concentration of host rock carbon (high crystallinity graphite in case of Hida gneiss) due to the pressure solution process. Additionally, experimental works revealed that the (3) graphitization of amorphous carbon due to the rapid sliding under the anoxic environment and (4) carbon (or low crystallinity graphite) deposition onto the sliding surface of marble due to the seismic faulting under the reducing environment. Graphite concentration via process (1) can be occur even if the protolith consists of carbon-free rocks (e.g. granitic rock) and this process is adaptable for the graphite-enrichment at the western part of the Ushikubi fault. The faults within the graphitic gneiss of Hida metamorphic rocks are greatly affected by process (2). On the other hand, the faults within the pelitic rock of non-metamorphic Tetori group are expected to suffered process (3). The direct evidence of process (4) has not recognized yet from the Atotsugawa fault system, however, there is a good possibility that it will occur within the crystalline limestone which frequently adjacent to the Ushikubi and Atotsugawa faults. These are the enrichment processes along the Atotsugawa fault system revealed in this thesis. Simultaneous and/or concurrent textural development due to the shearing might reduce the fault strength significantly even in small amounts of graphite (< 10 %).

6-3. The "weak" Atotsugawa fault system observed by seismological and geodetic study; micro-earthquakes and creeping fault motion

The Atotsugawa fault system is located in the Niigata-Kobe Tectonic Zone (NKTZ); a high strain rate belt which is identified using global positioning system (GPS) observation (Sagiya et al., 2000), in central Japan. The Atotsugawa fault system has several specific features on seismological and geodetical observations, as follows:

(1) Micro-earthquakes are distributed along the fault (Ito et al. 1998, 2007, see Figure 6.1),

(2) Possible fault creep of 2 mm/y in the middle part of the Atotsugawa fault from electronic distance metre (EDM) measurements (Tada, 1998; GSI, 2002) and 2-3 mm/y in the western part of the Atotsugawa and Ushikubi fault from GPS measurements (Ooi et al., 2003; Ohzono et al., 2011)

(3) Along fault heterogeneity of micro-earthquakes corresponds with inferred creep distribution.

(4) A large earthquake faulting; the Hietsu earthquake, A.D.1858 (estimated magnitude 7).

The most remarkable feature of the Atotsugawa fault system is creep-like fault motion concurrent with large earthquake fault (recurrence interval; 2300–2700 years). The surface creep was firstly detected from the observation during the term of 1981-1996 at the central area of the Atotsugawa fault (2 mm/y; GSI, 1997) by the EDM observations. Same observation has carried out simultaneously at the western part of the Atotsugawa fault, but no surface creep has been observed there. The creep-like fault motion of the slip rate of 3 mm/y was also observed from the eastern part of the Ushikubi fault by the dense GPS observation during the term of 1997-2001(Ooi et al., 2003), whereas no creeping motion was observed across the central part of the Atotsugawa fault. Recent compilation of GPS observations during the term of 1998–2006 (Ohzono et al., 2011) suggest that the approximately 2 mm/y velocity gap is exists across the western part of the Atotsugawa fault as well as the Ushikubi fault. Reports of both creep and stationary fault motion from the same observatory are interpreted for a time-dependent phenomenon of fault creep (episodic creep) since the measurements covering different time periods.

6-4. Evidence of graphitic fault zone along the Atotsugawa fault system, and interpretation for graphite-induced weakening

Along the Atotsugawa fault zone, resistivity structures were investigated by using the magnetotelluric (MT) method (Goto et al., 2005; Oshiman et al., 2005; Yoshimura et al., 2009). Notable feature of graphite, in addition to the frictional weakness, is its extremely low electrical resistivity ranging from 9 to 40 μΩm. Electrical resistivity of crustal rocks may vary over several orders of magnitude (0.1–100,000 Ωm), depending on a wide range of petrological and physical parameters (e.g., water content, volatiles, enhanced temperatures). However, the rock contains few % of graphite (e.g., graphitic gneiss or schist) shows significantly low electrical resistivity (a few Ωm) compared to other, carbon-free rocks. Therefore, graphite is regarded as possible candidates to explain high conductivity at crustal depths (e.g., Frost et al., 1989) in addition to highly saline water (brines), partial melts and serpentinites (if containing magnetite and hematite).

Goto et al. (2005) found the low resistivity bodies at shallow depths (< 3 km) of both of the Atotsugawa and Ushikubi faults, from across-fault sections at the eastern and western part of the Atotsugawa fault system (Figure 6.1a). At the deeper depths, in contrast, the faults are located at the boundary between high resistivity body and low one. Resistivity structure along the Atotsugawa fault displays two distinct features, that is, low resistivity in eastern part whereas high resistivity in central–western part and high microseismicity at low resistivity area (Figure 6.1b). Generally, possible candidates to explain high conductivity at crustal depths are regarded as highly saline water (brines). However, seismic tomography does not support existence of fluids along the Atotsugawa fault system (Nakajima et al., 2010, compare Figure 6.1 right side and left side) and there is still controversial to explain the existence of fluids owing to this conflict between resistivity structure and seismic tomography. Additionally, there is no serpentinites from Hida metamorphic belt. One possible interpretation for observed low resistivity is existence of graphite along the fault.

Stress measurement was also carried out to interpret the relationship between fault creep and stress state, from the location adjacent to the Atotsugawa fault. In-situ stress measurement with the hydraulic fracturing method done at 1.1 km northward from the Atotsugawa fault suggested that the almost perpendicular direction of maximum principal stress (N42°W ± 25°; Yamashita et al., 2006; N23°W; Ito et al., 2006). On the other hand, ENE-WSW direction of maximum principal stress which is

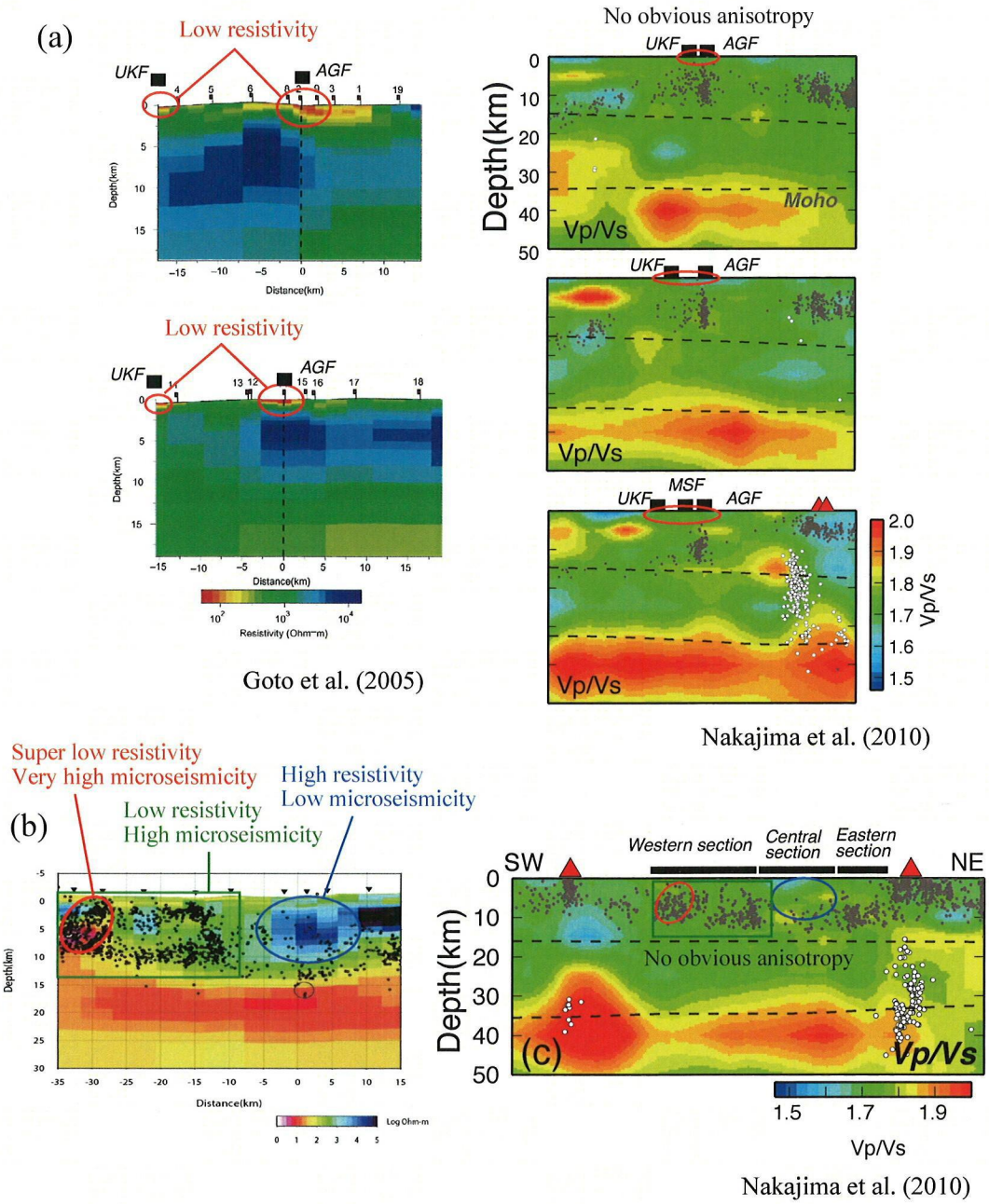

Fig. 6.1. Comparison of resistivity structure by Goto et al. (2005) and seismic tomography by Nakajima et al. (2010). (a) Section across to the Atotsugawa fault system at eastern and western part. (b) Section along to the Atotsugawa fault system.

consistent with regional stress field of Chubu district was also recognized from the measurements by borehole deformation on same observatory (Kuwahara et al., 2006). These results suggest that the direction of maximum principal stress orients not parallel but almost perpendicular or intersect (correspond with regional stress field) to the

Atotsugawa fault. This result is contrary to the theory that explains fault creep by stress orientation, and supports the existence of weak materials along the fault zone. Integrated explanation of all geophysical and geological data suggests the existence of weak graphite along the fault zone.

Table 3
Lateral heterogeneity along the Atotsugawa fault system (modified after Ohzone et al., 2011).

Method/Field	Western region	Central region	Eastern region	Reference
Surface geology	Pelitic gneiss		Non-metamorphic sediments (Tetori group)	Sohma & Akiyama (1983)
Deep geology	Pelitic gneiss	Volcanic gneiss	Granite	
EDM (1981-1996)	No surface freep	1.5 mm yr^{-1} surface creep		Tada (1998), GSI (2002)
GPS (1998-2006)	Possible creep motion of both UKF and AGF	Locked behaviour of AGF Possible creep motion of UKF		Hirahara et al. (2003, 2007), Ohzone et al., 2011
Seismicity	High, almost uniform seismicity	Low seismicity	High seismicity	Ito et al. (1998, 2007)
Seismic tomography (0–10 km)	High *Vp*	Low *Vp*, (Low *Vp/Vs*)		Kato et al. (2006, 2007) Nakajima et al. (2010)
Resistivity (MT) structure	Low resistivity corresponding to high seismicity.	High resistivity correspond-ing to low seismicity.		Yoshimura et al. (2006, 2009), Goto et al. (2005)

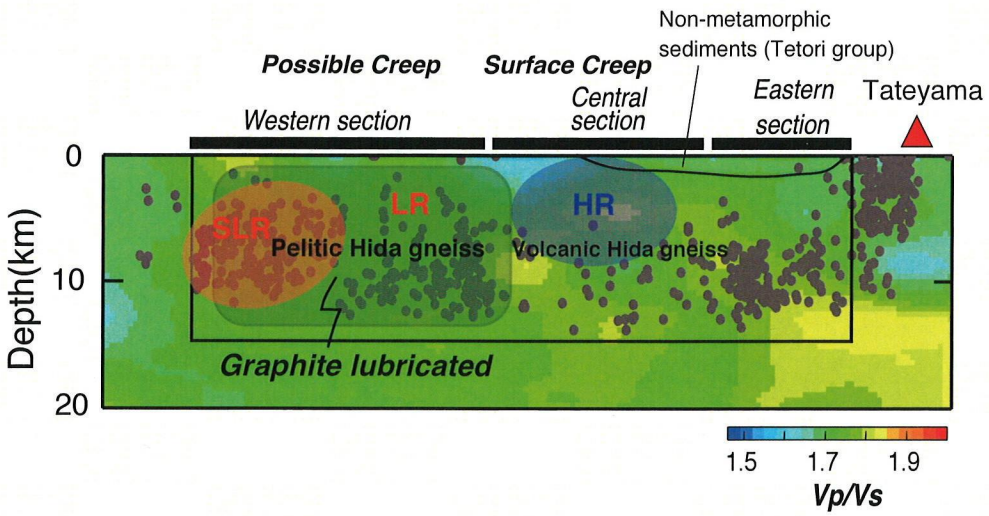

Fig. 6.2. An interpretation of geophysical data and geology along the Atotsugawa fault system (modified after Nakajima et al., 2010). SLR: super low resistivity, LR: low resistivity, HR: high resistivity.

6-5. Conclusion

The integrated field and experimental studies revealed that (a) ubiquitous distribution of graphite along the western part of the Atotsugawa fault system, (b) the significant weakness of graphite at a wide range of slip rates and (c) graphite content of those fault zones enough for reducing friction, suggesting the operation of graphite-induced fault weakening. Geophysical investigation of deep underground seismic-velocity and resistivity structures implies the existence of graphite at the deeper part of the Atotsugawa fault. Taking account of the geophysical data, the mechanical properties of graphite revealed in this study can explain well the creep-like fault motion and the distribution of active microearthquakes observed along the Atotsugawa fault system.

7. CONCLUSIONS

The main conclusions of this thesis are summarized as follows:

(1) The fieldwork along the Atotsugawa fault system and the detailed microstructural analysis of the fault rocks revealed that the two different concentration mechanisms of carbonaceous minerals along the fault zones. One is a pressure solution process: it enhances the mass transfer of water-soluble minerals such as quartz and carbonates and the enrichment of insoluble minerals such as carbon and metals along the fault zones. The other process is the precipitation of graphite from high-temperature carbon-rich fluid: this type of graphite typically appears as injection veins within the cataclasitic fault zones. The two processes lead to ~15 wt% of graphite concentration in the Atotsugawa fault zones, while their hostrock contains only 0~3 wt% of graphite.

(2) The series of experiments on pure amorphous carbon and graphite gouges were conducted under the various slip rates and normal stresses. The experiments revealed the large differences in steady-state friction coefficient μ_{ss} between amorphous carbon (μ_{ss} = 0.54) and graphite (μ_{ss} = 0.1) at low slip rates of less than 0.1 m/s. Faults with amorphous carbon are not weak at low slip rates, but they can become significantly weak to foster fault slip during earthquakes. On the other hand, graphite gouge always displays strikingly low friction coefficient with slight stick-slip motion.

(3) Frictional experiments on graphite-quartz mixture gouges were conducted to determine how large amount of graphite is needed to reduce the frictional strength and how the textural evolution within the fault zone is responsible for the fault weakening. Experimental result clearly indicates that the friction coefficient of the mixture gouge decreases with graphite content following a power-law relation irrespective of slip-rate; it starts to reduce at the graphite fraction of 5 vol% and reaches to the almost same level of pure graphite gouge at the fraction of more than 28 vol%. The non-linear, power-law dependency of friction on graphite content leads more efficient reduction of fault strength as compared with the previously reported linear dependency on weak clay minerals. The results suggest that the potential importance of graphite as an agent for the weakening of mature faults.

(4) The graphite was found from the simulated slip-localized zone of amorphous carbon gouge, which underwent the frictional heating due to rapid sliding. Thus the graphitization can indeed occur during seismogenic fault motion perhaps due to large shear strain, short-lived flash heating and stress concentration at asperity contacts, even at low temperatures and pressures under anoxic environments where the most earthquakes occur. This is another possible process for the graphite enrichment in the fault zones.

(5) The integrated field and experimental studies revealed that (a) ubiquitous distribution of graphite along the western part of the Atotsugawa fault system, (b) the significant weakness of graphite at a wide range of slip rates and (c) enough graphite content of those fault zones for reducing friction. The results indicate the importance of graphite as a weakening agent of faults. Geophysical investigation of deep underground seismic-velocity and resistivity structures implies the existence of graphite at the deeper part of the Atotsugawa fault system. Geophysical data and the mechanical properties of graphite revealed in this study suggest that graphite in fault zones is associated with the creep-like fault motion and the distribution of microearthquakes observed along the Atotsugawa fault system.

APPENDIX :
Evaluation of the effect of the Teflon sleeve on frictional behavior

In this study, I used a Teflon sleeve to surround the simulated fault zone and prevent leakage of gouge material. I evaluated the friction at the contact between the Teflon sleeve and the outer surface of the host rock in experiments without gouge to determine the corrections needed to the mechanical data.

Experiments were performed with an empty space 1 mm wide between the rotary and stationary cylinders at various slip rates and zero normal stress (see Figure.A1). On the runs at slip rates >56 mm/s, typical slip-weakening behavior was observed (Figure A1b and c), with measured shear tractions at initial peak and steady-state of ~0.75 Nm and 0.1–0.4 Nm, respectively. At the lowest slip rate of 0.15 mm/s, the shear traction fluctuated between 0.5 and 0.75 Nm. When the normal stress applied to the gouge was 1 MPa, Teflon friction contributed ~18% and <8% to the measured shear traction at the initial peak and steady-state, respectively. The contribution of Teflon friction decreased at higher applied normal stress. To determine intrinsic frictional behavior, I subtracted the shear traction obtained from the experiments without gouge from the raw traction data from each gouge experiment. Slight fluctuations of the friction coefficient after making the Teflon correction can be attributed to gouge leakage and tilting or movement of the Teflon sleeve, because the sleeve was not fixed during the experiments.

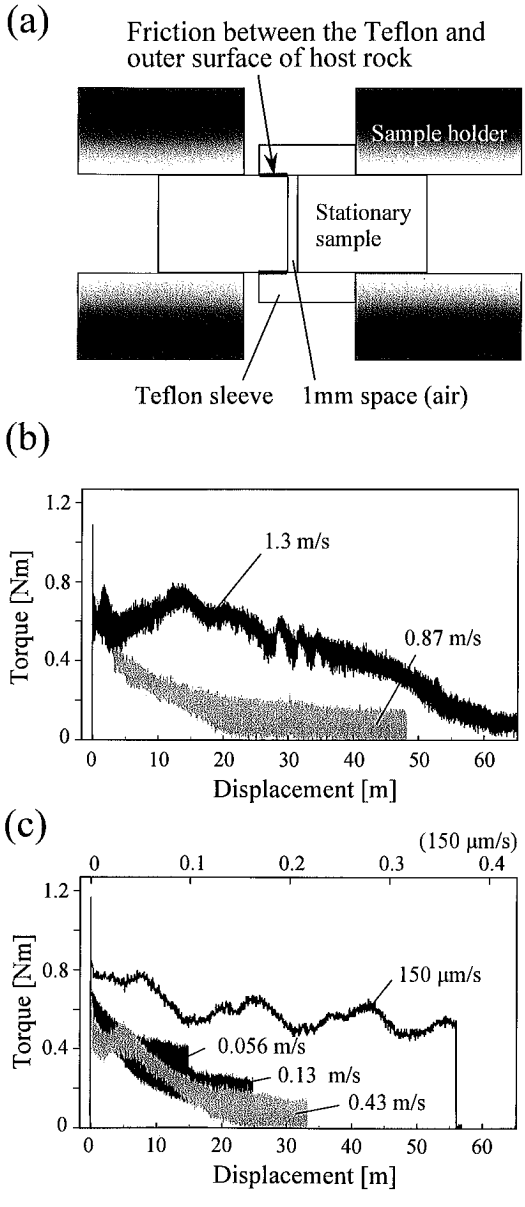

Fig. A1. (a) Schematic specimen configuration for the gougeless experiment to evaluate the effect of Teflon friction. Frictional behavior of Teflon sleeve is shown at high (b) and low to intermediate-velocities (c).

REFERENCES

Archard, J.F., 1958/1959. The temperature of rubbing surfaces, Wear 2, 438-455.

Awaji, D., 2006, Relationship between kinematic history and formation process of fluid channel in brittle shear zone. Ph.D. Thesis. Waseda University, Japan, pp104 (in Japanese, with English abstract).

Awaji, D., Sugimoto, R., Arai, H., Kobayashi, K., Takagi, H., 2010. Miocene dextral movement of Tanakura shear zone: Evidence from the western marginal fault, Hanawa Town, northeast Japan. Island Arc 19, 561-564.

Boylan, J., 1996, Smooth operators: Carbon-graphite materials. Material World 4, 707-708.

Brantut, N., Schubnel, A., Rouzaud, J.-N., Brunet, F., Shimamoto, T., 2008. High velocity frictional properties of a clay-bearing fault gouge and implications for earthquake mechanics. Journal of Geophysical Research 113, B10401, doi:10.1029/2007JB005551.

Brown, K.M., Koef, A., Underwood, M. B., Weinberger J. L., 2003. Compositional and fluid pressure controls on the state of stress on the Nankai subduction thrust: A weak plate boundary, Earth Planet. Sci. Lett., 214, 589-603.

Buseck, P. R., Huang, B.-J., 1985. Conversion of carbonaceous material to graphite during metamorphism. Geochimica et Cosmochimica Acta, 49, 2003-2016.

Bustin, R.M., Ross, J.V., Rouzaud, J.N., 1995. Mechanism of graphite formation from kerogen: experimental evidence. International Journal of Coal Geology 28, 1-36.

Byerlee, J.D., 1978. Friction of rocks. Pure and Applied Geophysics 116, 615-626.

Collettini, C., Niemeijer, A., Viti, C., Marone, C., 2009. Fault zone fabric and fault weakness. Nature 462, 907-910, doi:10.1038/nature08585.

Craw, D., 2002. Geochemistry of late metamorphic hydrothermal alteration and graphitisation of host rock, Macraes gold mine, Otago Schist, New Zealand. Chemical Geology 191, 257-275.

Crawford, B. R., Faulkner D. R., Rutter E. H., 2008. Strength, porosity, and permeability development during hydrostatic and shear loading of synthetic quartz-clay fault gouge, J. Geophys. Res., 113, B03207, doi:10.1029/2006JB004634.

Crespo, E., Luque, F.J., Rodas, M., Wada, H., Gervilla, F., 2006. Graphite–sulfide deposits in Ronda and Beni Bousera peridotites (Spain and Morocco) and the origin of carbon in mantle-derived rocks. Gondwana Research 9, 279 –290.

De Paola, N., Hirose, T., Mitchell, T.M., Di Toro, G., Viti, C., Shimamoto, T., 2011. Fault lubrication and earthquake propagation in thermally unstable rocks. Geology 39, 35-38, doi: 10.1130/G31398.1.

Diessel, C. F. K., Brothers, N. R., Black, P. M., 1978. Coalification and Graphitization in high-pressure schists in New Caledonia. Contributions to Mineralogy and Petrology 68, 63-78.

Di Toro, G., Goldsby, D.L., Tullis, T.E., 2004. Friction falls toward zero in quartz rock as slip velocity approaches seismic rates. Nature 427, 436-439, doi:10.1038/nature02249.

Dunne, W.M., Hancock, P.L., 1994. Paleostress analysis of small-scale brittle structures. Continental Deformation, Hancock, P.L. (ed.), Pergamon, Oxford, 101-120.

Elsworth, D., Marone, C., Niemeijer, A., 2009. Fabric induced weakness of tectonic faults. Eos Trans. AGU, 90(52), Fall Meet. Suppl., Abstract T53B-1574.

Frost, B.R., Fyfe, W.S., Tazaki, K., Chan, T., 1989. Grain-boundary graphite in rocks and implications for high electrical conductivity in the lower crust, Nature, 340, 134-136.

Geographical Survey Institute, Japan, 1997. Crustal deformation in the Chubu and the Hokuriku regions, Japan. Rep. Coord. Comm. Earthquake Predicy 57, 520–524 (in Japanese).

Goldsby, D.L., Tullis, T.E., 2002. Low frictional strength of quartz rocks at subseismic slip rates. Geophysical Research Letters 29 (17), 1844, doi:10.1029/2002GL015240.

Goto, T.,Wada,Y., Oshiman,N., Sumitomo,N., 2005. Resistivity structure of a seismic gap along the Atotsugawa Fault, Japan, Phys. Earth planet. Inter., 148, 55–72, doi:10.1016/j.pepi.2004.08.007.

Han, R., Shimamoto, T., Hirose, T., Ree, J., Ando, J., 2007a. Ultralow friction of carbonate faults caused by thermal decomposition. Science 316, 878-881.

Han, R., Shimamoto, T., Ando, J., Ree, J., 2007b. Seismic slip record in carbonate-bearing fault zones: An insight from high-velocity friction experiments on siderite gouge. Geology 35, 1131-1134.

Hirahara, K., Ooi, Y., Ando, M., Ohkura, T.,, 2003. Dense GPS array observations across the Atotsugawa fault, central Japan, Geophys. Res. Lett., 30, 8012, doi:10.1029/2002GL015035.

Hirahara, K., Ohozno, M., Sagiya, T., Hoso, Y., Wada, Y., Ando, M., 2007. Dense GPS array observations across the Atotsugawa fault system in Central Japan, in Geodynamics of Atotsugawa Fault System, pp. 25–44, ed. Ando, M., TERRAPUB, Tokyo.

Hirose, T., Bystricky, M., 2007. Extreme dynamic weakening of faults during dehydration by coseismic shear heating. Geophysical Research Letters 34, L14311, doi:10.1029/2007GL030049.

Hirose, T., Shimamoto, T., 2005. Growth of molten zone as a mechanism of slip weakening of simulated faults in gabbro during frictional melting. Journal of Geophysical Research 110, B05202, doi:10.1029/2004JB003207.

Holdsworth, R. E., 2004. Weak faults--Rotten cores. Science 303, 181-182, DOI: 10.1126/science.1092491.

Inagaki, M., Kang, F., 2006. Carbon materials science and engineering: from fundamentals to applications. Tsinghua University Press, pp604.

Itaya, T., 1981. Carbonaceous material in pelitic schists of the Sanbagawa metamorphic belt in central Shikoku, Japan. Lithos, 14, 215-224.

Ito, K., Wada, H., Wada, K., 1998. Give chase to fault movements by seismic activity, Earth Mon., 20, 137–141 (in Japanese).

Ito, K., Wada, H., Ohmi, S., Hirano, N., Ueno, T., 2007. Seismic activity from routine and temporary observations of earthquakes in the northwest Chubu district, central Honshu, Japan, in Geodynamics of Atotsugawa Fault System, pp. 45–63, ed. Ando, M., TERRAPUB, Tokyo.

Ito, T., Omura, K., Kato, H., Tanaka, H., Sekine, K., 2006 Stress measurements by the Baby Borehole Hydro-fracturing method, BABHY, in the vicinity of the Atotsugawa fault. Abstract of 2006 Japan Earth and Planetary Science Joint Meeting, S117-012, Makuhari, Japan.

Kato, A., Kurashimo, E., Hirata, N., Iwasaki, T., Iidaka, T., 2006. Imaging crustal structure around the western segment of the Atotsugawa fault system, central Japan, Geophys. Res. Lett., 33, L09307, doi:10.1029/2006GL025841.

Kato, A., Iidaka, T., Kurashimo, E., Nakagawa, S., Hirata, N., Iwasaki, T., 2007. Delineation of probable asperities on the Atotsugawa fault, central Japan, using a dense temporary seismic network, Geophys. Res. Lett., 34, L09318, doi:10.1029/2007GL029604.

Katz, M. B., 1987. Graphite deposits of Sri Lanka: a consequence of granulite facies metamorphism. Mineralium Deposita 22, 18-25.

Kita, I., Matsuo, S., Wakita, H., 1982. H_2 Generation by Reaction Between H_2O and Crushed Rock. J. Geophys. Res. 87,10789-10795. An Experimental Study on H2 Degassing From the Active Fault Zone

Kuwahara, Y., Omura, K., Kiguchi, T., Yamashita, F., 2006. A new method for stress orientation measurements by using borehole deformation -Application to the Atotsugawa fault. Abstract of 2006 Japan Earth and Planetary Science Joint Meeting, S117-011, Makuhari, Japan.

Landis, C. A., 1971. Graphitization of dispersed carbonaceous material in metamorphic rocks. Contributions to Mineralogy and Petrology 30, 34-45.

Logan, J. M., Rauenzahn, A., 1987. Frictional dependence of gouge mixtures of quartz and montmorillonite on velocity, composition and fabric. Tectonophysics, 144, 87-108.

Miyashita, Y., Yoshioka, T., Kuwabara, T., Kariya, Y., Matsuura, K., Yoshimura, M., and Takase, N., 2003. Paleoseismological study of the southwestern part of the Ushikubi fault on Toyama/Gifu prefectural border (1) Geomorphological and geological survey. Annual Report on Active Fault and Paleoearthquake Researches, Geological Survey of Japan/AIST, No.3, 47-62.

Mizoguchi, K., Hirose, T., Shimamoto, T., Fukuyama, E., 2007. Reconstruction of seismic faulting by high-velocity friction experiments: An example of the 1995 Kobe earthquake. Geophysical Research Letters 34, L01308, doi:10.1029/2006GL027931.

Mizoguchi, K., Hirose, T., Shimamoto, T., Fukuyama, E., 2009. High-velocity frictional behavior and microstructure evolution of fault gouge obtained from Nojima fault, southwest Japan, Tectonophysics, doi:10.1016/j.tecto.2009.02.033.Manatschal, G., 1999. Fluid and reaction assisted low angle normal faulting: evidence from rift related brittle fault rocks in the Alps (Err Nappe, eastern Switzerland). Journal of Structural Geology 21, 777-793.

Moore, D.E., Lockner, D.A., Summers, R., Shengli, Ma, Byerlee, J.D., 1996. Strength of chrysotile-serpentinite gouge under hydrothermal conditions: Can it explain a weak San Andreas fault?. Geology 24, 1041-1044.

Moore, D.E., Lockner, D.A., 2004. Crystallographic controls on the frictional behavior of dry and water-saturated sheet structure minerals. J. Geophys. Res. 109, B03401, doi:10.1029/2003JB002582.

Moore, D.E., Lockner, D.A., 2007. Comparative deformation behavior of minerals in serpentinized ultramafic rock: Application to the slab-mantle interface in subduction zones. Int. Geol. Rev. 49, 401–415.

Moore, D.E., Rymer, M.J., 2007. Talc, serpentinite, and the creeping section of the San Andreas fault. Nature 448, 795-797.

Moore, D.E., Lockner, D.A., 2010. Frictional Strengths of Talc-Serpentine and Talc-Quartz Mixtures J. Geophys. Res., doi:10.1029/2010JB007881, in press.

Nakajima, J., Kato, A., Iwasaki, T., Ohmi, S., Okada, T., Takeda, T., The Japanese University Group of the Joint Seismic Observations at NKTZ, 2010. Deep crustal structure around the Atotsugawa fault system, central Japan: A weak zone below the seismogenic zone and its role in earthquake generation Earth Planets Space 62, 555-566.

Nover, G., Stoll, J., 2001. Graphitisation of carbon - a p,T-laboratory experiment. Protocol on the 19th Colloquium "Electromagnetic Depth Research", Hördt, A., Stoll, J. (Eds.), German geophysical society.

Oberlin A., 1984. Carbonization and graphitization. Carbon 22, 521-541.

O'Hara, K., Mizoguchi, K., Shimamoto, T., Hower, J.C., 2006. Experimental frictional heating of coal gouge at seismic slip rates: evidence for devolatilization and thermal pressurization of gouge fluids. Tectonophysics 424, 109-118.

Ohzone, M., Sagiya, T., Hirahara, K., Hashimoto, M., Takeuchi, A., Hoso, Y., Wada, Y., Onoue, K., Ohya, F., Doke, R., 2011. Strain accumulation process around the Atotsugawa fault system in the Niigata-Kobe Tectonic Zone, central Japan. Geophys. J. Int. doi: 10.1111/j.1365-246X.2010.04876.x.

Oohashi, K., 2008MS. Evolution and Mineralization processes of Fault-related rocks at the Atotsugawa and Ushikubi fault system, Northern Hida highland. M.S. Thesis. Niigata University, Japan, pp178 (in Japanese, with English abstract).

Oohashi, K., Kobayashi, K., 2008. Fault geometry and paleo-movement of the central part of the Ushikubi fault, northern central Japan. Jour. Geol. Soc. Japan 114, 16-30 (in Japanese, with English abstract).

Oohashi, K., Kobayashi, K., Mashima, H., 2008. A method for making thin sections and polished slubs of non-cohesive fault rocks containing swelling clay minerals. Jour. Geol. Soc. Japan 114, 426-431 (in Japanese, with English abstract).

Oohashi, K., Hirose, T., Shimamoto, T., 2011. Shear-induced graphitization of carbonaceous materials during seismic fault motion: experiments and possible implications for fault mechanics. Journal of Structural Geology, doi:10.1016/j.jsg.2011.01.007, in press.

Ooi, Y., 2003MS. Analysis of crustal deformation around the Atotsugawa fault system obtained with dense GPS array observations. Master Thesis, Graduate School of Environmental Studies, Nagoya University.

Oshiman et al., 2005. Preliminary report on deep resistivity structure deduced from wide-band MT measurements around the Niigata-Kobe strained belt (the Atotsugawa fault) in Japan. Annuals of Disas. Prev. Res. Inst., Kyoto univ., 48, 125-132.

Pasteris, J.D., Chou, I.-M., 1998. Fluid-deposited graphitic inclusions in quartz: Comparison between KTB (German Continental Deep-Drilling) core samples and artificially reequilibrated natural inclusions. Geochimica et Cosmochimica Acta 62, 109-122.

Reches, Z., Lockner, D.A., 2010. Fault weakening and earthquake instability by powder lubrication. Nature 467, 452-455.

Rumble, D., Hoerign, T.C., 1986. Carbon isotope geochemistry of graphite vein deposit from New Hampshire, U.S.A.. Geochimica et Cosmochimica Acta 50, 1239-1247.

Saffer, D. M., C. Marone, 2003. Comparison of smectite- and illite-rich gouge frictional properties: Implications for the updip limit of the seismogenic zone along subduction megathrusts, Earth Planet. Sci. Lett., 215, 219-235.

Sagiya,T., Miyazaki, S., Tada,T., 2000. Continuous GPS array and present day crustal deformation of Japan, Pure appl. Geophys. 157, 2303-2322.

Saito, T., Tanaka, H., Shimada, K., Nakamura, M., 2006. New technology of separating and continuous monitoring of groundwater and desolved gases in 200 m drilled-hole in Atotugawa Fault. Japan Geoscience Union Meeting, Abstract

S119-006.

Savage, R. H., 1948. Graphite Lubrication. Journal of Applied Physics 19, doi:10.1063/1.1697867.

Shikano, K., Harayama, S., Yamamoto, H., Takeuchi, M., Uto, K., Komazawa, M., Hiroshima, T., Sudo, S., 1999. Geological map of Japan 1/200,000 KANAZAWA. Geological survey of Japan.

Shimamoto, T., Tsutsumi, A., 1994. A new rotary-shear high-velocity friction testing machine: Its basic design and scope of research (in Japanese with English abstract), Structural Geology, 39, 65-78.

Shimamoto, T. and T. Hirose, Reproducing low to high-velocity fault motion in fluid-rich environments: An experimental challenge and preliminary results, European Geosciences Union, General Assembly, Vienna, Austria, EGU06-A-09077, 2-7 April, 2006.

Sohma, T., Akiyama, S., 1983. Geological structure and lithofacies in the central part of the Hida metamorphic belt. Jour. Geol. Soc. Japan 90, 609-628 (in Japanese, with English abstract).

Tada, T., 1998. Crustal movement around the Atotsugawa fault, Earth Mon., 20, 142-148 (in Japanese).

Takahashi, M., Mizoguchi K., Kitamura K., Masuda K., 2007. Effects of clay content on the frictional strength and fluid transport property of faults, J. Geophys. Res., 112, B08206, doi:10.1029/2006JB004678.

Tembe, S., Lockner, D. A., Wong, T.-F., 2010. Effect of clay content and mineralogy on frictional sliding behavior of simulated gouges: Binary and ternary mixtures of quartz, illite, and montmorillonite. J. Geophys. Res., 115, B03416, doi:10.1029/2009JB006383.

The Research Group of Active Faults in Japan, 1991, Active Faults in Japan: sheep maps and inventories. University of Tokyo Press, 439pp.

Togo, T., Shimamoto, T., Ma, S., Wen, X., He, H., 2011. Internal structure of Longmenshan fault zone at Hongkou outcrop, Sichuan, China, that caused the 2008 Wenchuan earthquake. Earthquake Geology, *under review.*

van Diggelen, De Bresser, J. H., Spiers, C., 2009, The effect of phyllosilicates and matrix on fault strength-implications for the San Andreas fault zone. Eos Trans. AGU, 90(52), Fall Meet. Suppl., Abstract T53C-1601.

Wibberley, C.A.J., Yielding, G., Di Toro, G., 2008. Recent advances in the understanding of fault zone internal structure: a review. Wibberley, C. A. J., Kurz, W., Imber, J., Holdsworth, R. E., Collettini, C. (Eds.), The Internal Structure of Fault Zones: Implications for Mechanical and Fluid-Flow Properties 299, 5-33, DOI: 10.1144/SP299.2

Wilks, K.R., Mastalerz, M., Ross, J.V., Bustin, R.M., 1993. The effect of experimental deformation on the graphitisation of Pennsylvania anthracite. International Journal of Coal Geology 24, 347-369.

Winter, H., Aelhardt, S., Jerak, A., Kuchenhoff, H., 2002. Characterization of cataclastic shear-zones of the KTB deep drill hole by regression analysis of drill cuttings data. Geophys. J. Int. 150, 1-9.

Xiaowei, L., Robin, J.-C., Suyuan, Y., 2004. Effect of temperature on graphite oxidation behavior. Nuclear Engineering and Design 227, 273-280.

Yamada, N., Nozawa, T., Harayama, S., Takizawa, F., Kato, H., Hiroshima, T., Komazawa, M., 1989. Geological map of Japan 1/200,000 TAKAYAMA. Geological survey of Japan.

Yamashita, F., Omura, K., Yamada, R., Matsuda, T., Fukuyama, E., Mizoguchi, K., 2006. Stress measurement with the hydraulic fracturing method performed in the Atotsu tunnel of the Kamioka mine. Abstract of 2006 Japan Earth and Planetary Science Joint Meeting, S117-010, Makuhari, Japan.

Yoshimura, R. et al., 2006. Electrical resistivity structure along the Atotsugawa fault -Preliminary Report-, Abstract of 2006 Japan Earth and Planetary Science Joint Meeting, S118-P001, Makuhari, Japan.

Yoshimura, R. et al., 2009. Magnetotelluric transect across the Niigata-Kobe Tectonic Zone, central Japan: a clear correlation between strain accumulation and resistivity structure. Geophys. Res. Lett., 36, L20311, doi:10.1029/2009GL040016.

Yund, R.A., Blanpied, M.L., Tullis, T. E., Weeks, J. D., 1990. Amorphous material in high strain experimental fault gouges. Journal of Geophysical Research 95, 15589-15602.

Zulauf, G., Kleinschmidt, G., Oncken, G., 1990. Brittle deformation and graphitic cataclasites in the pilot research well KTB-VB (Oberpfalz, FRG). Geological Society, London, Special Publications 54, 97-103.